Flow Visualization and Simulation of Miscible Displacement with Gravity Domination

A thesis Submitted for

Doctor of Philosophy in

Petroleum Engineering

By

Zeeshan Mohiuddin

Supervisors:

Dr Manouchehr Haghighi

Dr Yvonne Stokes

Dr Themis Carageorgos

Australian School of Petroleum

Faculty of Engineering, Computer and Mathematical Sciences

The University of Adelaide, Australia

September 2013

TABLE OF CONTENTS

List of Figures

List of Tables

Abstract

Gravity assisted miscible gas injection into oil reservoirs is an efficient method of Enhanced Oil Recovery (EOR). Carbon dioxide injection into aquifers for sequestration purposes is another application of miscible displacement under gravity control. This dissertation reports pore-scale experimental and simulation studies to determine the role of different parameters on the frontal stability of the miscible displacement process under gravity domination.

Experimental studies were based on visualization of first contact miscible flooding under gravity domination. Visualization was conducted using the glass micromodel technique. Facilities were designed and fabricated to perform the experiments. Two micromodels with different patterns of loose packing and close packing were prepared through the sandblasting technique. The porous patterns for these micromodels were generated using the MATLAB program. The injection of the lighter and less viscous iso-octane was carried out in comparatively heavier and high viscous butanol. The injections were carried out at different dipping angles ($0 \leq \theta \leq 90$) and injection velocities (representing near wellbore and reservoir flow rates). The images were captured and processed to analyse the frontal movement and to estimate the concentration of injecting fluid in the flow domain. The experimental results presented in this thesis demonstrate the dependencies of various characteristics such as dip angle and porous medium heterogeneity on the process at pore scale.

The simulation studies were performed using the Finite Element Analysis technique. The simulation model was initially validated by matching results with flow visualization experimental studies using glass micromodels. The Navier–Stokes, continuity and convection-diffusion equations were used in the simulation instead of Darcy's law. Wide ranges of parameters applicable for Enhanced Oil Recovery and CO_2 sequestration were used in the sensitivity study. Dip angles (θ) between 0° and 180° (for up-dip and down-dip situations), different domain velocities, density differences of 50 to 900 kg/m^3 between the injecting and displaced fluids and viscosity ratios from 1 to 100 (to include light and heavy oils) were investigated. Snapshots were captured in each simulation case for visual comparison of the frontal advancement. In addition, breakthrough saturation was plotted against cos (θ) to quantify the competition

between viscous and gravity forces in the gravity-dominated miscible displacement process.

The pore-scale study suggests that the stability of a miscible process can be influenced by several factors. When gravity acts in favour of displacement and there is a moderate to large density difference, angular tilt is the most important parameter influencing displacement. When the density difference is small, then the mobility ratio and flow velocity also play a role. When gravity opposes displacement and buoyancy forces are dominating, results show little sensitivity to the actual tilt angle. Better displacement is seen for lower density difference and for higher flow velocity; yet, again, the mobility ratio only impacts on displacement when the density difference is quite small.

The sensitivity simulation studies were performed based on: (a) mobility ratio, density difference and angle of tilt; (b) domain velocities; and (c) local and global heterogeneity. The sensitivity study for $0 \leq \theta \leq 90$ suggests a region that is sensitive to angular dip. The region $90 < \theta \leq 180$, however, is more sensitive to the density difference between injection and inplace fluids. For $0 \leq \theta \leq 180$ mobility ratio might be significant if the density difference between injection and inplace fluid is small. Sensitivity based on domain velocity suggests that large reduction in domain velocities might lose the inertial effects and might cause overriding, especially for the high-dipping angle cases. Sensitivity based on heterogeneity suggests that decreasing grain spacing promotes the fluid mixing. Therefore, in less permeable zones, the overriding of lighter fluid can be reduced even in high-dipping angle cases.

Statement of Originality

This work contains no material which has been accepted for the award of any other degree or diploma in any university or other tertiary institution and, to the best of my knowledge and belief, contains no material previously published or written by another person, except where due reference has been made in the text.

I give consent to this copy of my thesis, when deposited in the University Library, being made available for loan and photocopying, subject to the provisions of the Copyright Act 1968.

I also give permission for the digital version of my thesis to be made available on the web, via the University's digital research repository, the Library catalogue, and also through web search engines, unless permission has been granted by the University to restrict access for a period of time.

Signature :_____

Zeeshan Mohiuddin

Australian School of Petroleum

The University of Adelaide, Australia.

Acknowledgements

I would like to especially thank Dr Manouchehr Haghighi and Dr Yvonne Stokes for their continuous guidance and support. Moreover, I would like to acknowledge Dr Themis Carageorgos and Dr Danny Gibbins for their assistance during the experimental and image processing work. I would also like to thank my family who supported me during the tough times in my PhD studies.

List of Publications

Zeeshan Mohiuddin, Manouchehr Haghighi and Yvonne Stokes (2013). 'Pore level visualisation and simulation of CO_2 miscible injection with gravity domination', Energy Procedia, **37:** 6885–6900.

Zeeshan Mohiuddin, Manouchehr Haghighi and Yvonne Stokes. 'Pore level visualisation and simulation of CO_2 miscible injection with gravity domination', paper presented at the 11th International Conference on Greenhouse Gas Control Technologies, Kyoto International Conference Centre, Japan, 18–22 November 2012.

Zeeshan Mohiuddin, Manouchehr Haghighi, Yvonne Stokes, Themis Carageorgos and Danny Gibbins. 'Pore scale visualization and simulation of miscible displacement process under gravity domination', paper IPTC 15310 presented at the International Petroleum Technology Conference Bangkok, Thailand, 15–17 November 2011.

Zeeshan Mohiuddin and Manouchehr Haghighi. 'Visualization of CO_2 displacement process under gravity domination", paper SPE 144101 presented at the SPE Enhanced Oil Recovery Conference, Kuala Lumpur, Malaysia, 19–21 July 2011.

Abbreviations, Prefixes and Symbols

Breakthrough Saturation (S_b)

Carbon Capture and Storage (CCS)

Cyclic Gas Injection (CGI)

Density Difference ($\Delta\rho$)

Diffusion Coefficient (D_o)

Enhanced Oil Recovery (EOR)

First Contact Miscibility (FCM)

Gas Assisted Gravity Drainage (GAGD)

Hue Saturation and Value (HSV)

Original Oil in Place (OOIP)

Minimum Miscibility Pressure (MMP)

Mobility Ratio (M)

Multiple Contact Miscibility (MCM)

Red Green Blue (RGB)

Water Alternating Gas (WAG)

CHAPTER 1 INTRODUCTION

1.1 Miscibility

Miscibility is defined as a physical condition between two or more fluids that permits mixing in all proportions without the existence of an interface. Under this condition, molecules of fluids are free to move around each other as no interface and capillary forces exist and fluids behave as a single fluid. The solvent (or the inplace fluid with large volume) molecules overcome the intermolecular Van der Waals' forces in the solute (or the injected fluid), and find their way between and around the solute molecules. The solvent molecules also manage to distribute themselves uniformly to form a homogeneous mixture.

Miscibility can be explained by an example of a gas that is injected into a liquid at normal conditions situated in the porous mass. Only a small percentage of the gas will be dissolved in the liquid at normal conditions and both the gas and liquid exist with an interface, which separates both fluids. The liquid will swell with the presence of the gas and its viscosity will slightly reduce. This condition is termed as immiscible gas swelling. Figure 1-1 shows the schematic of an immiscible gas swelling of oil in the porous media. A common example of two partially miscible fluids is water and carbon dioxide (CO_2) at atmospheric pressure and temperature condition.

NOTE:
This figure/table/image has been removed
to comply with copyright regulations.
It is included in the print copy of the thesis
held by the University of Adelaide Library.

Figure 1-1: Schematic of Immiscible Gas Swelling of Oil in Porous Media (BP-Amoco 1999)

The immiscible condition can be changed to a miscible condition when the pressure and/or the temperature of the system are increased to a certain value so there is no clear demarcation between the liquid and gas. The two fluids behave as a single fluid and one cannot distinguish between the two fluids. Figure 1-2 is a schematic of a miscible displacement process which shows that when a miscible gas is introduced in the porous medium at high pressure and/or temperature condition, it develops a single phase with existing oil.

Gases are usually miscible in each other due to large intermolecular spaces and weak dispersive forces between the molecules. However, a liquid-liquid or a liquid-gas system may or may not be miscible depending on different factors such as composition, condition and polarity (Rao 2006).

NOTE:
This figure/table/image has been removed
to comply with copyright regulations.
It is included in the print copy of the thesis
held by the University of Adelaide Library.

Figure 1-2: Schematic of Miscible Gas Displacement in the Porous Media (BP-Amoco 1999)

Two fluids are termed as First Contact Miscible (FCM) when they are brought in contact with each other at certain pressure and temperature conditions and readily form a single phase mixture. FCM is the simplest method to achieve miscibility. Besides FCM, there is a case where injected fluid initially does not achieve miscibility with the inplace fluid. However, as the process continues, modification in the composition of the injected or inplace fluid occurs, which develops miscibility between the fluids. Since this type of miscibility develops gradually due to the mass transfer between the two fluids, it is termed as dynamic miscibility or more commonly as Multiple Contact Miscibility (MCM). The condition when two fluids are unable to mix in any proportion to form a single phase is termed immiscible.

1.2 The Importance of Miscibility in Petroleum Engineering

Miscibility has various applications in different science and engineering disciplines. In petroleum engineering the most important role of miscibility is in Enhanced Oil Recovery (EOR) and geological CO_2 sequestration. EOR processes are those which aim to recover trapped or discontinuous oil from the reservoirs. This oil is trapped in the porous media after primary recovery and/or after waterflooding. The trapping of oil is due to the capillary forces which facilitate the oil to reach almost zero relative permeability. Due to this zero relative permeability oil becomes immobile, and any further injection of immiscible fluid merely flows around the trapped oil.

Among many different EOR processes, miscible EOR is the process in which a fluid (mostly a gas) is introduced in the porous media which develops first or multiple contact miscibility with the oil and ideally behaves as a single fluid with no interface.

Thus the trapped oil ideally forms a single phase mixture with the injected fluid and becomes mobile to produce some additional percentage of oil. This method of EOR was successfully applied to several fields across the world after primary and/or secondary recovery (Smith Duane 1988).

The miscible EOR processes offer great advantages over the other methods of EOR as theoretically no surface tension and capillary effects are present that account for oil entrapment (Sahimi, Reza Rasaei et al. 2006). The molecules of fluids are therefore free to move and displace each other within the porous medium. If the viscosity of the injected fluid is less than that of the inplace fluid, then the effective viscosity of the mixture might also be less than that of the original oil. This reduces the applied pressure gradient that is required to displace the oil and to aid recovery (Booth 2008), and theoretically the recovery of oil might reach 100% (Asgarpour 1994).

In miscible EOR processes it is ideal to select a fluid that could develop FCM with the inplace oil. In this regard, hydrocarbon solvents such as ethane and butane could develop FCM with most of the reservoir oils at high pressure and temperature conditions. However, the solvents that are FCM with oil are usually expensive for continuous injection and are not financially viable for a project (Holm 1986). In contrast, gases such as flue gas, nitrogen, methane and CO_2 are considerable cheap and readily available. However, these gases are MCM with inplace oil instead of FCM at most reservoir conditions. Among these gases, CO_2 is a good candidate as a miscible fluid because large volumes of CO_2 are available from industry and environmental sources. Additionally, CO_2 has good solubility, especially with light oil, which can achieve miscibility if the pressure exceeds the Minimum Miscibility Pressure (MMP)—the pressure required to achieve a miscible state. Since CO_2 is a gas, it could invade tiny pores that are inaccessible to water, which in turn increases displacement efficiency and the recovery factor. Furthermore, its wetting characteristics favour the displacement of oil over water, which helps to develop an oil bank ahead of the injected gas and increase the oil production (Fayers and Zhou 1996).

Upon developing miscibility with oil, CO_2 could decrease the effective viscosity and the interfacial tension. An additional advantage in using CO_2 in miscible displacements is that once the oil recovery process is complete, the CO_2 is left behind in the oil

reservoir. Perkins (2011) reported that at the end of 2009 in the Joffre field, 30% of CO_2 was stored in the reservoir (57.6 bcf was injected and 40.4 bcf was produced) while 11.5% Original Oil in Place (OOIP) of oil was recovered as a result of the CO_2 miscible EOR process. Thus CO_2 miscible EOR could also serve the purpose of carbon capture and storage (CCS). The removal of CO_2 from the atmosphere by enhancing the oil production process has therefore gained attention as a possible means of both reducing global warming and increasing oil production (Booth 2008). Therefore, an additional benefit of CO_2 sequestration above EOR can be obtained. However, conventional miscible EOR processes have aimed to maximise oil production and to minimise CO_2 injection (Perkins 2011) due to some inherited problems of the process which are outlined in the next section.

The carbon dioxide sequestration process is the process when CO_2 is stored subsurface. Among different methods of geological CO_2 sequestration, solubility trapping is the process when supercritical CO_2 is dissolved in the deep saline formation water. Carboxylic acid is formed along with bicarbonate and carbonate ions. The formation of this solution is heavier than water and thus CO_2 loses buoyancy, which decreases the chance of leakage (Greenman 2009). Solubility trapping is considered to be covered under solubility (or partial miscibility) and not under miscibility (Kuo, Perrin et al. 2010) because full miscibility might not be achieved due to the high MMP of CO_2 in saline water.

1.3 Problems Associated with Miscible Gas EOR

As described above, miscible gas injection has the potential to scrub almost 100% of the oil from a reservoir *if* complete miscibility is achieved. The complete miscibility depends on various chemical and physical characteristics of oil, injected fluid and porous media etc. Besides, one of the principal requirements is the physical contact of injecting and displacing fluid (or oil) under appropriate conditions. This physical contact is a major requirement that decides the success of miscible displacement (Dumore 1964; Coskuner 1993). Unfortunately, this condition is not always fulfilled, even in homogeneous reservoirs. The major contributors in this regard are the viscosity and density of the injected fluid (Raible 1992). Injected fluid is usually less viscous and less dense compared to the inplace oil at reservoir conditions. This restricts its contact

with inplace oil and reduces mass transfer, which in turn promotes instabilities (Kurowski, Misbah et al. 1995).

1.3.1   Problem Due to Less Viscosity of Injected Gas

The less viscosity of the injected gas results in viscous fingering. The less viscous gas has high mobility and thus tends to penetrate into the more viscous oil; the overall effect of this uneven penetration results in poor sweep efficiency. In the FCM process, the injected and inplace fluid become a single phase upon the first contact; however, this cannot stop the viscous fingering of the injected less viscous solute (Homsy 1987). Viscous fingering in the FCM process is due to the variations in concentration of chemical components. The variation in the concentration in the porous media is due to either by molecular diffusion or by dispersion/convection. High mobility of injected gas is used to reduce by processes such as Water Alternating Gas (WAG) and Cyclic Gas Injection (CGI). The primary target of these processes is to reduce gas relative permeability so that early breakthrough will not occur (Stalkup 1983).

1.3.2   Problem Due to Less Density of Injected Gas

The WAG and CGI processes are moderately effective in controlling the mobility of the injected gas because of the less density of the gas and/or high density of water compared with oil (Rao 2006; Mahmoud and Rao 2007). Since the gas is lighter and water is heavier than oil at the reservoir condition, overriding of gas and underriding of water occurs. This reduces the contact of the injected fluid with the oil and leaves a high percentage of oil unswept. Figure 1-3 shows the schematic description of this phenomenon.

NOTE:
This figure/table/image has been removed
to comply with copyright regulations.
It is included in the print copy of the thesis
held by the University of Adelaide Library.

Figure 1-3: Underriding of heavier and overriding of lighter fluid during WAG process (Rao 2006)

Besides WAG and CGI, the overriding phenomenon can be experienced in any gas injection process. The degree of gravity override increases as the difference in density between the reservoir and the injected gas increases. The problem of the overriding of injected gas is often roughly controlled through injection rates. The gas is injected at a higher flow rate to achieve inertial effects. Since the velocity is high, a small time is provided to settle, which may avoid overriding (Blunt, Fayers et al. 1993). However, the higher rates in horizontal flooding may leave plenty of oil because of viscous fingering. The gravity override problem is also minimised when CO_2 is used as an injected gas due to its comparable density with the reservoir oil under reservoir conditions. However, CO_2 has a high tendency to channel though the oil due to its low viscosity, which results in higher residual saturations and poor sweep efficiency by viscous fingering (Wang 1980; Campbell and Orr 1985).

The inherited limitations of the miscible gas injection process restrict physical contact between the inplace oil and the injected gas and result in a reduced recovery efficiency (i.e. product of the displacement efficiency and sweep efficiency) (Raible 1992). Therefore, the full advantages of the miscible displacement process cannot be utilised despite its high potential to recover more oil.

1.3.3 Gravity-Dominated Miscible Displacement

The effect of gravity can be utilised to minimise the inherited problems of miscible flooding and to enjoy the benefits of this process. This can be performed when a less dense gas, compared with inplace oil, is injected in the direction parallel to gravity

instead of perpendicular to gravity. This method couples conventional miscible gas EOR with the concept of gravity drainage, a process of self-propulsion of oil due to gravity in the reservoir rock (Lewis 1944; Hagoort 1980; Chatzis, Kantzas et al. 1988). Therefore, when a less dense fluid is injected parallel to the gravity in a dense fluid, the less dense fluid tends to remain at the top of the dense inplace fluid. This gravity segregation of less dense and dense fluids promotes a stable displacement and increases the sweep efficiency of the displacement. Moreover, the gravity forces dominate the viscous forces and favour the stability of the displacement process (Tiffin and Kremesec-Jr. 1988). This mechanism has long been studied (Dumore 1964) and was modified and renamed as the Gas Assisted Gravity Drainage (GAGD) process (Rao 2006). The schematic of this process is shown in Figure 1-4.

NOTE:
This figure/table/image has been removed
to comply with copyright regulations.
It is included in the print copy of the thesis
held by the University of Adelaide Library.

Figure 1-4: Schematic of Gas Assisted Gravity Drainage Process (Rao 2006)

This method of coupling miscible EOR is quite effective and, as Dumore (1964) reported, it is even possible in the gravity-dominated miscible process to completely avoid gravity override if applied properly. In addition, Tiffin and Kremesec-Jr. (1988) reported that during their core flooding studies, miscibility was developed in a much shorter core length in a gravity-dominated miscible flooding compared with the conventional horizontal miscible flooding. Besides this EOR application, the voidage replacement capability of this process offers the additional application of CO_2 sequestration in subsurface formation as reported by Jadhawar (Jadhawar and Sarma 2010). To date, this method has been studied (Kasiri and Bashiri 2009; Jadhawar and

Sarma 2010) and used successfully in various fields across the world (Palmer, Nute et al. 1984; Moore 1986; Johnston 1988; Bangia, Yau et al. 1993).

Although this technique is very significant, various sensitive parameters are responsible to make it more efficient. Moreover, no reservoir is perfectly vertical so a gas can be injected in a perfectly vertical direction. Pore-scale knowledge in this regard is important because the instability initiates at pore level. This pore-scale knowledge could be utilised to determine the areal and vertical sweep efficiencies.

Therefore, performing a pore-scale study of the gravity-dominant miscible process helps to understand the flow mechanisms at pore scale. The critical and non-critical parameters can be identified through this study, which could be considered useful information during a core-scale or a full-field level study. Many studies (Dumore 1964; Stalkup 1983) were conducted in the past that considered a perfect scenario using Darcy's law and proposed a rate of injection to avoid instability during gravity-dominated miscible displacement. This optimum rate was set low enough so that the less dense fluid remained segregated from the oil (Stalkup 1983). However, the stability does not merely depend on the rate of injection, but on various different parameters. Many different attempts were made to determine the stability of a vertical miscible front with gravity using a continuum approach (Schowalter (1965), Rogerson and Meiburg (1993) Manickam and Homsy (1995)) These studies exclude the pore-level physics due to their approximation of continuum and the use of Darcy's law. To understand the actual mechanism and to acquire better knowledge of the displacement mechanisms, pore-level studies are required.

1.4 Research Gap

Details of the past simulation and experimental studies conducted in the domain of gravity-dominated miscible displacement will be addressed in Chapter 2, which advises that detailed sensitivity studies were not conducted to show the competition of different parameters affecting the performance of the process. These parameters include a complete range of dip angles, injection flow rate (velocity), heterogeneity, fluid density and viscosity contrast.

The previous visualization studies adopted procedures (for example, glass beads and core flooding) such that the actual pore geometry was not known for numerical

simulation, and therefore experiments cannot be repeated using the same scenarios and cannot be modelled using the same geometric features. Some experimental studies also used the Hele-Shaw cell which lacks the pore-scale complexities. Therefore, visual experimental studies were required to be carried out using a method so that porous geometry could be controlled and which could be repeated in the simulation studies.

Similarly, the simulation studies conducted in the past were mostly reliant on either continuum (Darcy's Law) or pore-network modelling (Poiseuille's Law). These laws were based on the average properties of the porous media. No exact simulation has therefore been developed which is based on actual governing laws (Navier–Stokes, continuity and convection-diffusion equation) rather than approximate laws. Since the actual geometry was not used in the past simulation studies, various different mechanisms (such as the diffusion/dispersion effect) have not been accounted for.

1.5 Research Aims and Objectives

The present research primarily aims to fill the identified research gaps and to conduct a pore-level experimental and simulation study on the gravity-dominated miscible displacement process. The study aims to find critical parameters which can affect the miscible displacement process. The identification of these critical parameters would help to classify the factors and/or the parameters which could influence the process on the pore scale. Better visualization and simulation techniques aim to identify the interplay of these parameters on the gravity-dominated miscible displacement process.

The present work does not pretend to analyse a real reservoir problem. However, the findings of this research could be upscaled to core scale and the information could be utilised to determine the potential of the gravity-dominated miscible process via numerical simulation or through core-flood experiments.

1.6 Scope of Work

The scope of the present research study is divided into two parts, experimental and simulation:

1.6.1 Experimental

1. Designing porous media patterns and developing the patterns on a piece of glass with the best possible technique.

2. Designing and manufacturing a flow visualization set-up to hold a glass micromodel and to perform experiments at the required angle.

3. Designing and constructing the piping and instrumentation set-up to conduct experiments at the required conditions.

4. Conducting visualization experiments at various angles and operating conditions.

5. Capturing and processing images during each experiment at fixed-time intervals.

6. Analysing the results of the different experiments.

1.6.2 Simulation

1. Transferring the same porous media pattern used initially for experimental studies to finite element analysis software so that simulation can be performed on an exact porous domain.

2. Assigning the physics and the equations into the model. Partial differential equations and boundary conditions needed to be assigned properly. Meshing was required to be performed in the flow domain.

3. Comparing the simulation and experimental results.

4. Comparing the simulation results with past studies found in literature for gap identification.

5. Detailed sensitivity analysis based on a wide range of physical and chemical parameters affecting the process. This helped to identify the regions of stable and unstable displacement.

CHAPTER 2   LITERATURE REVIEW

This chapter reviews the published literature in the domain of pore-scale experimental (visualization) and simulation studies on the gravity-dominated miscible displacement in porous media.

2.1 Pore-Scale Visualization

Flow visualization experiments are considered to be a useful tool in a variety of porous media fluid-flow investigations. The concept of flow visualization was initiated by Haines (1925) through a study of drainage-imbibition in porous media using uniform and regular metallic (phosphor bronze) balls packing. This study pioneered the concept of moving interfaces, which is considered to be the foundation of several oil-recovery mechanisms. Afterwards, the interest in fluid-flow visualization grew, and many researchers and engineers reported a large amount of literature on the use of different flow visualization experiments so to understand the behaviour of fluid flow through porous media.

Several methods and techniques were introduced that used flow visualization to study complex mechanisms and each had its own advantages and limitations. Therefore, background knowledge of different methods and their capabilities was explored to select the appropriate method for the present research study.

Hele-Shaw Cells

Meyer and Searcy (1956) first visualized the rate of water-cone rise in a Hele-Shaw cell. This cell consisted of two parallel glass plates separated by a cellulose acetate sheet. This cell was not a porous media; however, the flow in between the glass plates were mathematically represented as the flow in porous media because the governing equation of the Hele-Shaw cell was found to be similar to Darcy's law (Homsy 1987).

Capillary Tube

Gardescu (1930) used fine capillary tube with two periodic enlargements to investigate the behaviour of gas bubbles in oil flow through capillaries. Later, Rose and Witherspoon (1956) presented a concept of two parallel pores connected to each other with capillary tubes in order to obtain the relative permeability relationships, and to explain the trapping of the non-wetting phase. This method was relatively simple to

explain the behaviour of multiphase flow in porous media; however, it was lacking in terms of explaining the tortuosities.

Powder or Beads Pack

Engelberts and Klinkenberg (1951) performed visualization experiments using unconsolidated grains (sand and pyrite) of approximately equal sizes to study the oil displacement by water in pores and demonstrated the viscous fingering effect in the porous media. This method considered the tortuosities effects as the fluid flow occurred in the granular media. Hill (1952) extended this concept and performed visualization experiments using a column packed with granular bone charcoal to study the displacement of sugar liquors by water. His study set the foundation of the concept of interface stability during a displacement process in terms of the viscosities and densities of the fluids. Later, Meurs (1957) performed experiments to visualize the displacement of oil by water using powdered glass packed in a transparent cell. Glass was used due to its similar wettability conditions compared with the reservoir rock (sandstone). In addition, Heller (1959) modified the concept of Rahman (1949) and used grains of Christiansen composite as porous media. The Christiansen composite had the same refractive index with that of the inplace fluid and when the inplace fluid fully invaded the model, the overall combination of grains and inplace fluid became transparent. However, when another fluid with a different refractive index was injected, the zone of invasion did become visible. Afterwards, the beads pack visualization received much attention and, to date, several studies (Yoon, Germaine et al. 2006; AlHamdan, Cinar et al. 2011; Pathak 2011; Krummel, Datta et al. 2013) have reported using glass beads pack to visualize different mechanisms.

While this method does offer good features of 3-D visualization, a few limitations are inherited. The pore spaces cannot be controlled even if the uniform-sized sieved grains are used. The pore space is therefore considered as an unknown parameter and only estimated values can be used for reporting purposes. Moreover, repeatability of experiments is often not possible as for each set of experiments the grains might rearrange their position/location, which makes it practically impossible to perform the experiment under the same conditions. Furthermore, because of the uncertainty of grains/pore location and geometry, beads pack visualization does not permit the

replication of the exact geometry and grains arrangement during modelling. In addition, the pore shapes cannot be varied as the beads have to be uniform.

Glass Micromodel

In this visualization approach a desired porous pattern is etched onto the piece of glass, and this etched glass is then fused with another piece of plain glass under high temperature. Once the two glass plates are fused, the fluid can flow through the inlet port and be produced at the outlet port. This method is of prime importance as the geometry of the grains and pores can be controlled. In addition, glass is a transparent medium that allows effective visualization. Also, glass possesses similar wettability conditions to that of a sandstone reservoir. This visualization approach was therefore found to be very useful.

This method of visualization was first introduced by Mattax and Kyte (1961) when they etched a desired pattern of grains and pore geometry onto a piece of glass to study the waterflooding in the porous media. The micromodel in that study was prepared by coating wax onto the glass plate. The pattern was designed by drawing lines on the wax manually using a fine stylus. The waxed coated glass was then exposed to hydrofluoric acid to perform etching. Davis and Jones (1968) improved this technique by replacing the wax coating with a photosensitive resist, a resin which becomes both insoluble in many solvents upon ultraviolet (UV) light exposure and acid resistant. Therefore, any black and white coloured pattern can be etched through this technique as it allows a complicated pattern to be etched onto the glass surface.

The interest in this particular technique has continuously grown over time, especially in the petroleum industry, because of its advantages over other visualization techniques. Several different mechanisms were studied that included, but are not limited to: miscible enhanced oil recovery (Campbell and Orr 1985); drainage in fractured systems (Haghighi, Xu et al. 1994); interfacial tension (Mackay, Henderson et al. 1998); solution gas drive (Bora, Maini et al. 2000); water alternating gas (Sohrabi, Tehrani et al. 2004); immiscible enhanced oil recovery (Shariatpanahi, Dastyari et al. 2005); heavy oil depressurisation (Shahabinejad, Danesh et al. 2005); gravity drainage (Mollaei, Haghighi et al. 2006); gas hydrates (Mohammadi, Ji et al. 2006); capillary pressure (Ghazanfari, Rashtchian et al. 2007); Polymer flooding (Meybodi, Kharrat et al. 2008);

Microbial enhanced oil recovery (Crescente, Rekdal et al. 2008); steam-assisted gravity drainage (Mohammadzadeh and Chatzis 2009); gas flooding (Mohiuddin and Haghighi 2011); and wettability (Afrapoli, Alipour et al. 2012). Continuous development was carried out in the domain of micromodel pattern design (Sayegh and Fisher 2009; Mohiuddin, Stokes et al. 2012) and preparation (Mohiuddin and Haghighi 2011; Karadimitriou, Joekar-Niasar et al. 2012) and many authors reviewed the detailed history of micromodel development phases.

As discussed above, this method offers great advantages over other methods as the geometry of grains, pores or fracture geometries can be adjusted and fixed for all sets of experiments (Campbell and Orr 1985). Therefore, the repeatability for each set of experiments is possible. Since the geometry of the porous pattern is known, the experiments can be simulated using the same geometric features. It is noted, however, that the glass micromodel porous network is usually defined as a 2-D homogeneous system and therefore does not represent the complexity of a real reservoir.

Other Visualization Techniques

Currently, many different visualization technologies exist such as X-ray, CT scan (Alajmi, Grader et al. 2008), microfused X-ray CT scan (Setiawan, Nomura et al. 2012) and MRI imaging (Graue, Kvamme et al. 2008). However in all of these processes, the grains pattern cannot be reproduced during modelling and simulation due to unknown porous geometry.

As discussed in the above paragraphs, literature suggests various different approaches to fluid-flow visualization. Each method offers some good feature, and therefore a method should be selected which suit the particular objective of a study. The present study aimed to conduct the visualization and simulation of miscible displacement in the porous media. Therefore, a method was required to hold the capabilities so that the exact grain pattern remained conserved in each set of visualization experiments and could be reproduced during the simulation study. Glass micromodel method was found to be appropriate in this regard and thus it was selected for the present research work.

2.1.1 Pore-Scale Visualization for Miscible Displacement

This section discusses past advancements and attempts in the domain of miscible displacement visualization. The traditional miscible displacement considers the

injection of miscible fluid in the horizontal direction. The injection fluid is usually less dense than the inplace fluid, which causes the fluid to rise, and, in turn, the overriding problem.

Although the importance of gravity domination in fluid flow through pores has been recognised since long (Wyckoff, Botset et al. 1932), the gravity segregation effects in horizontal flooding in a miscible environment was first studied by Craig Jr et al. (1957) using sand and glass beads pack. The liquids (water and a water glycol mixture) of various viscosity ratios were injected to signify the problem of gravity override in horizontal flooding. Sweep efficiencies were plotted for a five-spot pattern with a range of different mobility ratios. Crane, Kendall et al. (1963) later performed glass beads experiments on two mobility ratios of 6.5 and 27 and showed the effect of gravity on frontal displacements. A mixture of fluids was displaced by a mixture of water, potassium chloride and a tracer. The model was set in a horizontal position; however, the interface was vertically inclined. This interface inclination was set via injecting one fluid from injector and the other fluid from producer, and the mixture was bled through holes drilled 10 cm away from the inlet port. The interface between the fluids was found after observing the tracer. Transition from high to low gravity forces was studied by plotting a dimensionless ratio of viscous to gravitational forces against the pore volume injected required to produce 98% of the inplace fluid for two different mobility ratios. Visual observation regarding front destabilisation was not reported in this study.

Various visualization studies (Pozzi and Blackwell 1963; Campbell and Orr 1985; Withjack and Akervoll 1988; Rao 2006; Sayegh and Fisher 2009) were also reported which signifies the role of gravity override and viscous fingering in conventional horizontal flooding. The role of gravity is therefore considered very important in the miscible displacement process. The following section discusses the studies conducted in the past in the domain of gravity-dominated miscible displacement.

2.1.1.1 Experimental Studies on Miscible Displacement with Gravity Effects

Hill (1952) was the first to systematically report the importance of displacement of fluid under the influence of gravity. This study focused on the gravity-dominated immiscible displacement of sugar liquors by water in a column of granular bone charcoal. Due to the immiscible displacement, a sharp interface between the fluids was assumed. A

critical rate was proposed using Darcy's law through equating pressure of invading and defending fluids at the horizontal interface. Later, Blackwell et al. (1959) performed visualization of miscible displacement in a uniform sand-packed tube. This work was based on the interplay between diffusion, dispersion and convection transport in the porous media. The experiments were performed by injecting a less viscous and less dense fluid vertically downwards with a small 4° tilt, with respect to vertical, at different rates. Small ranges of density difference between 0.1 and 0.28 g/cm^3 were tested. Piston-like displacement was found in low-rate injection cases (0.5 ft/day), while fingers were observed when injecting at a higher rate (50 ft/day).

A few years later, Gardner et al. (1962) performed glass beads experiments and studied the motion of interface in a gravity-segregated system. Heavier fluid was injected in the lighter fluid; however, no direct visualization was carried out to visualize the frontal advancement. To match the results, an analytical equation was derived to study the combined effect of early and late motion of the interface, which assumed that the interface remained horizontal.

Slobod (1964) conducted core-flooding experiments by injecting fluid vertically down into unconsolidated sands to study the effect of gravity segregation in vertical miscible floods. Different sets of mobility ratios (0.4 to 2.7) and density differences (0 to 0.2 g/cc) were tested at large flow rates between 25 to 100 ft/day. The effect of gravity and viscous forces were highlighted based on the mixing zone length between 5 to 95% of the injected fluid pore volumes. Hence the nature of the miscible fluids mixing zone in terms of density difference, viscosity ratio and flow rate was determined. The ratio of injection rate and critical velocity of immiscible fluids defined by Hill (1952) was compared with the change in the mixing-zone length of different cases of gravity and viscosity contrasts. The study was based on fundamental principles, but it missed to allocate diffusion in the porous media. Moreover, the comparison of results with the immiscible critical rate generated some errors along with some experimental errors as reported by Slobod himself (Slobod 1964).

Dumore (1964) presented the idea of stable displacement in the gravity-dominated miscible system. Glass beads visualization experiments were performed in a glass tube. The injection of gasoline was carried out in oil in a vertically downward direction. The

experiments were conducted to justify a theoretical hypothesis on front stability of a gravity-dominated miscible displacement. This hypothesis was an upgraded version of Hill's (1952) work on immiscible displacement with gravity. Dumore (1964) stated that the front stability in a gravity-dominated miscible displacement can be achieved if the pressure in the inplace fluid is higher than that in the injected fluid at their interface. A theoretical expression of injected velocity was proposed utilising Darcy's law, for which a stable front can be obtained in a miscible displacement. A linear change of density and a logarithmic change in viscosity was assumed with respect to change in injected fluid concentration in the transition zone between the injected and inplace (or displaced) fluid. The logarithmic viscosity was determined by matching results with the experimental data. Dumore proposed the following equation for stable injection velocity, u_{st}, above which the injection front become unstable in a vertically downward miscible displacement.

$$u_{st} = \frac{a(\rho_o - \rho_s)}{\mu(ln\mu_o - ln\mu_s)}kg$$

Where,

a = experimentally derived value to achieve a viscosity match with the experiments.

ρ = density.

μ = viscosity.

Subscript o and s represent oil and injected solvent respectively.

Although this study set the basics of stability in gravity-dominated miscible displacement, it simplified many concepts. For example, the pressure between the injected and inplace fluid was set as the only criterion to establish a stable system, and Darcy's law approximation was used. In addition, fluid mixing in porous media was not considered, and viscosity was a function of the produced solvent concentration coefficient obtained after the experimental results were matched.

Nute (1983) and Cardenas et al. (1984) reported lab studies conducted to apply miscible CO_2 injection in a dipping reservoir of Bay St. Elaine field. The experiments were performed on clean silica sand packed in a steel pipe that was situated in a heater at

$73^{\circ}C$ and inclined 36°. The temperature and pressure conditions were selected because of the specific reservoir in consideration. The injection mixture composition of CO_2/methane/n-butane was obtained through the slim-tube experiments, and was required to be injected in the waterflooded conditions. The experiments were conducted to confirm the miscibility between the oil and the injected mixture and to determine linear displacement efficiencies of gravity-dominated miscible front. This study was considered as a lab-screening study for a field application and therefore it did not provide any fundamental pore scale information.

Tiffin and Kremesec (1988) performed core-flooding experiments on miscible gravity-dominated displacement to study the density and compositional behaviour of CO_2. This study aimed to improve the stability criteria of gravity-dominated immiscible (Hill 1952) and miscible processes (Dumore 1964) via measuring mixing-zone length between 10 and 90% of injected fluid concentration. In the experimental study, less viscous and less dense fluid was injected vertically downwards into the core and the density of the produced mixture was measured. Moreover, the mixing-zone length was estimated after the refractive index analysis of the produced fluids. A mixing coefficient was defined as a function of mixing-zone length. However, this mixing coefficient was strictly applicable to equal density and equal viscosity displacements and did not take viscous mixing and gravity override problems into account. The ratio of the injection velocity and critical velocity defined by Hill (1952) was compared with the mixing coefficient to predict the region of molecular diffusion, dispersion (that is, additional diffusion due to tortuosities of porous media) and convection (velocity-dominated flow).

The mixing-zone concept was also studied by Buès and Aachib (1991) through monitoring the change in the mixing zone in gravity-dominated miscible displacement. Experiments were conducted in a vertical column filled with quartz sand and the change in the mixing-zone concentration was monitored through measuring change in electrical conductivities of the mixture inside the flow domain. This study mainly dealt with the mixing effect between two fluids of different density and viscosity based on the calculated values. However, this approach of determining stability with the help of the density of a produced mixture or through analysing mixing-zone composition was

criticised by many authors (Manickam and Homsy 1995) and thus did not received much appreciation.

In all of the studies reported prior to 1993, those conducted in the domain of gravity-dominated miscible displacement were based on calculations; no visual study was conducted to witness the instability of a system when gravity forces come into action in miscible displacement. The first visualization study on the gravity-dominated miscible process was reported in 1993 by Page et al. when they performed experiments of injection of a viscous and heavy fluid in less viscous and light fluid using sintered glass beads to form a consolidated porous media. Experiments were performed using injection vertically upwards, vertically downwards, horizontal and horizontal direction. This was the first time a visualization study was conducted on a gravity-dominated miscible system; however, this study was purely qualitative and no analysis was conducted. The visual result showed that the fingering effect reduced when lighter fluid was injected from the top compared to when injected from the bottom and in a horizontal direction. Although the results were fairly straightforward, the important aspect of this study was visualization of the results.

The Page et al. (1993) study was further extended by Guo and Neale (1996) using the similar technique of sintered glass beads. Distilled water was injected in different aqueous mixtures of glycerol. The injection was carried out in top, bottom and horizontal directions. The use of different aqueous glycerol mixtures produces change in viscosity ($\mu_{inplace}/\mu_{injecting}$) and density ($\rho_{inplace}/\rho_{injecting}$) ratio. The increase of glycol concentration in the aqueous solution was found to be directly proportional to the increase in viscosity and density ratio. However, this methodology produced more change in the viscosity compared to the change in density. The mobility ratio was varied from 1.5 to 147; however, the density ratio was varied from 1.03 to 1.23. Thus viscosity interplay was more highlighted than density change. This was witnessed in the vertical injection case when the recovery of lower density ratio (1.03) was higher than the case of high density ratio (1.23), which might have been due to dominating viscous forces.

In 2007 Mahmoud and Rao performed an experimental study using Ottawa sand packed between two glass plates. Two fluids with near equal densities were selected with the

density difference ($\Delta\rho$) = 0.016 g/cc. The lighter fluid was injected from the top in a vertically downward direction. No information about the fluid viscosities, injection rate and injection pressure etc. was reported. Because of this negligible density difference, the recovery was reported to be 100%; however, it was not reported whether this recovery at the breakthrough or at the end of the process.

In 2008 Jiao and Maxworthy (2008) performed experiments using a Hele-Shaw cell to study the interplay between density and viscosity in a miscible gravity-dominated study. The less viscous and light fluid was injected into a high viscous and heavy fluid at various angles. This study focused on observations related to fingering patterns and geometric features in a gravity-dominated miscible displacement. However it is to be noted that although many authors claimed that the Hele-Shaw cell was mathematically analogous to the real porous media, it in fact lacked an important aspect of considering pore microstructure: that unlike the flow between plates, flow in a porous media involves roughness which causes resistance and extra mixing due to dispersion. This approximation could results in serious errors as reported by different authors (Kong, Haghighi et al. 1992; Wu, Xiao et al. 2011).

Abbas and Rose (2010) reported a study using inert and reactive porous media to study the transport of ionic solutions of different concentrations and densities. This study was mainly targeted at liquid fertilisers in agricultural fields, and considered injection of a dense fluid vertically upwards against the gravity and in horizontal directions. Breakthrough saturations were plotted against the pore volume injection for different pure vertical and horizontal cases. The breakthrough concentration was plotted against the pore volume injection for two different velocities, and the delay in the breakthrough and gentle versus sharp slope of the curves were related to the mixing of the fluids at the interface.

The available literature outlined in the above paragraphs shows that the experiments performed which targeted the stability of gravity-dominated miscible displacement were either based on purely qualitative (Page, Brooks et al. 1993) or quantitative (Jiao and Maxworthy 2008) approaches. Moreover, most of the experiments were conducted using a process where control on the grains and pore structure and size was not possible (for example, core flooding, beads/sand pack). Since exact pore geometry was not used,

the analysis was performed based on average parameters (such as permeability) rather than on pore-scale parameters. In addition, repeatability could not be achieved as the arrangement of the grains and pores changed after every experiment. Besides, due to unknown pore geometry, simulation on an exact scale was not possible which resulted in uncertainty.

Some past studies were conducted on a Hele-Shaw cell which lacks an important aspect of pore microstructure and thus cannot be equivalent to a porous media. Moreover, previous studies considered either a small or no angular dip. Most of the studies focused on perfectly horizontal or perfectly vertical cases. Few studies reported experiments at only single dipping angle and a complete sensitivity study has never been conducted. Thus a gap exists to conduct detailed experimental studies at different dipping angles on the stability of the process. In addition, the effects of changes in pore arrangement (or heterogeneity) have also never been properly addressed in past studies. Therefore, the present research study aims to fill most of these gaps through conducting experiments taking sensitivity of various parameters such as angular dip and pore arrangement into account. Furthermore, the experiments are conducted on a glass micromodel so that the grains geometry can be controlled and reproduced for the simulation study. It is to be noted that due to experimental limitations all the scenarios cannot be tested and so pore scale simulation studies are also performed.

2.2 Pore-Scale Simulation

Experiments are the direct way to obtain information about a process in a real-world context. However, operational challenges often limit the execution of experiments. Lengthy experimental procedures integrated with risk and uncertainties associated with unavoidable human, instrumental and post-processing errors affect the authentication of the results acquired. In light of these factors, precision and accuracy is practically not possible to maintain.

Simulation studies are therefore performed to avoid these experimental limitations. Simulation allows more flexibility to test scenarios which might not be possible to test during an experimental study. However, the reliability of simulation results depends on the authentication of the simulation model. Thus a simulation model must be validated

before any prediction is made. This could be done by simulating the experimental study and comparing the results.

Pore-level simulation is a useful technique to study the physics of the processes at the pore level. This kind of simulation is usually preferred over commercial reservoir simulations to study the pore-scale flow phenomenon because reservoir simulators are based on Darcy's law and Buckley–Leverett equations to predict two-phase flow through the porous medium using relative permeabilities. Darcy's law is applicable for steady flow under conditions such that inertial effects are negligible. In addition, it considers average parameters like permeability, which is not a true representation of pore-scale fluid flow. Due to this limitation, reservoir simulators only account for uniform or compact flow and are unable to describe the interfacial instabilities. Furthermore, the use of large grid-block sizes in these simulators minimises computational time, but results in significant errors in recoveries causing over-mixing of fluids. The information provided by the commercial simulators is significant for the macroscopic level, but their efficiency could be improved by inputting the information obtained after the pore-level simulation study.

The concept of pore-scale fluid-flow simulation originated from Fatt (1956) who established concurrency between a capillary network and the real porous media. An electrical circuit of wire and resistance was compared with the system of pore and throat in a porous medium to obtain the flow properties. The capillary pressure and relative permeability curves of the drainage process in a capillary network were calculated and the results were compared with the results of the performed experimental study. Different capillary network arrangements were tested to match the experimental results. The concept of modelling real porous media as a bundle of capillary tubes was therefore proposed. This concept received tremendous appreciation and development has been carried out since then. Several studies (Lenormand, Zarcone et al. 1983; Mollaei, Haghighi et al. 2007) were then reported on pore-scale simulation to validate the visual experiments and/or to extrapolate the experimental findings.

2.2.1 Pore Network Modelling

Pore network modelling is the modern version of capillary tube modelling to simulate the flow in the porous media as described earlier. Pore network simulators are the fit-to-

purpose simulators and the program has been coded as per the requirement of the process. This technique is very popular and a huge amount of literature has been reported (Rose 1957; Simon and Kelsey 1971; Lenormand, Touboul et al. 1988; Blunt 2001; Mollaei, Haghighi et al. 2006; Stevenson, Ferer et al. 2006; Xu 2008) to study various different mechanisms.

This method considers a network of pore bodies, interconnected with throats or capillaries, to represent the void spaces of a porous rock. The shape of pore and throat may be selected based on the problem under consideration (Simon and Kelsey 1971; Stevenson, Ferer et al. 2006; Mollaei, Haghighi et al. 2007; Xu 2008). Size (or volume) of pore and/or throat may be randomly generated values or based on experimental evidence (Simon and Kelsey 1971; Xu, Kamath et al. 1999). The use of random size pores/throat represents the heterogeneity of the porous rock. The pores and throats are then spatially arranged over the flow domain based on some defined arrangement such as a rectangular diamond or hexagon etc. The location of the pores and throats is then allotted randomly to certain places in the defined arrangement. Desired physics is then assigned to the network model and the results are drawn. The results obtained from the network model are then matched with the available experimental values. Often geometric features (number of pores/throats, size, shape and location of pores/throats, overall network arrangement etc.) of the network model are tuned if the results are not comparable with the experiments. This exercise is repeated until the results are acceptably matched. The purpose of this exercise is to achieve a reasonable geometric arrangement that reflects the unknown geometry of the porous bodies. Once the match is found in an acceptable range, the network model is believed to represent the actual porous network so that sensitivity studies can be made.

Although this simulation technique is quite popular because of its flexibility to model different phenomena, the method of approximating the actual geometrical arrangements of the grains and pores is spatially uncorrelated. It shows a conceptual representation of a porous medium while not taking actual porous geometry into account. The geometry of pores and throats in a network model is usually estimated based on matching the results with few parameters. This produces uncertainties because different kinds of experiments might provide different sizes, shapes and patterns of pores and throats (Simon and Kelsey 1971). Moreover, all the experimental studies are accompanied with

some operational/unavoidable errors and therefore relying on only experimental matching cannot provide a decent network model. The oversimplification of a real porous pattern method might not correctly simulate the pore-scale mechanisms. Furthermore, since a network of pipes is used to model the porous rock, pipe-flow concepts are used to model the flow of fluid in porous media that are based on average principles and therefore cannot be fully characterised under pore-level simulation.

2.2.2 Pore Scale Simulation Studies on Gravity-Dominated Miscible Flow

Simulation studies on miscible flooding under horizontal conditions have been widely conducted. These studies mostly recount the viscous fingering and gravity override effects in a perfect horizontal scenario. The viscous fingering effect and the gravity segregation of miscible fluids during the horizontal flooding through the particle-tracking method using Darcy's law was studied by Tchelepi and Orr (1994). Pore network modelling (Siddiqui and Sahimi 1990) and experiments results matching through finite difference analysis of Darcy's law and the convection–diffusion equation (Christie, Jones et al. 1990) was also carried out for the horizontal miscible flooding.

Simulation studies on miscible flooding under non-horizontal conditions (under gravity) were mostly based on an analytical technique (based on the Hele-Shaw cell theory). The Darcy's law and convection–diffusion equation have been solved simultaneously under different boundary conditions. These studies mostly focused on the unstable interface due to finger growth and thus reported fingers' characteristics. Studies conducted by Rogerson and Meiburg (1993) and Manickam and Homsy (1995) are noticeable in this regard.

Besides the analytical approaches, a pore network modelling study was also conducted by Stevenson et al. (2004). Miscible simulation was studied for the extreme scenarios of 0° and 180° dips with respective to the vertical. Pipe flow Poiseuille's equation was used to calculate the flow rate in the throats that connect the spherical pore bodies. The fluid flow in the network model was the function of pressure difference between the interconnected pore bodies. The diffusive/dispersive mixing of the fluids was not taken into account with this model and a variable, interfacial width, was described as the proxy of dispersivity. In order to validate the network model, Stevenson et al. compared

the simulation results with the experimental work of Freytes et al. (2001) (glass beads) and Tiffin and Kremesec (1988) (core flooding).

For matching results with the Freytes et al. (2001) study, Stevenson et al. (2004) chose the cases where Freytes et al. injected a near equal density ($\Delta\rho \sim 10^{-3}$ kg/m^3) and equal viscosity fluid upward from the bottom of the glass beads packing to measure the dispersivity and found a scenario where destabilisation occurred. However, the Stevenson et al. model did not account for the dispersion mechanism and so a direct comparison was not possible. Therefore, interfacial width of different simulation cases was compared with the defined destabilisation limit proposed by Freytes et al. (2001). However, this showed some deviation as the destabilisation limit observed in the work on log scale by Freytes et al. (2001) was found to be slightly higher than the limit found by Stevenson et al. (2004).

While matching the simulation results with Tiffin and Kremesec's (1988) experimental study, a disagreement was found between the breakthrough saturation values. Out of several experiments, Figure 2-1 shows the best matched results of Stevenson et al. (2004). However, the simulation data was unable to properly fit the experimental results.
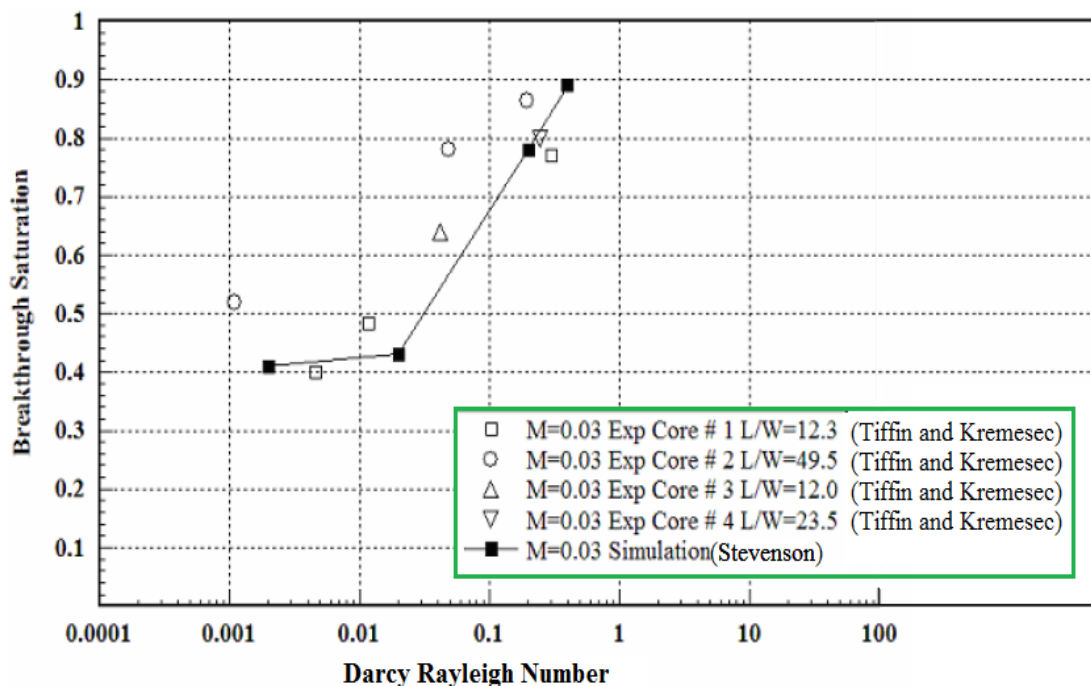
Figure 2-1: Comparison of the Work by Stevenson et al. (2004) and Tiffin and Kremesec (1988)

One of the main reasons for mismatching the simulation results of Stevenson et al. with the work of Freytes et al. (2001) and Tiffin and Kremesec (1988) is because the experimental studies were unable to provide all the necessary information and Stevenson et al. manipulated the data to fit the simulation model. Furthermore, the actual grain arrangement in the experiments (glass beads and core flooding) was unknown and therefore an experimental study was required to be conducted with known parameters to address the simulation model properly. Another reason could have been using pipe-scale physics for the porous medium.

In the sensitivity analysis conducted by Stevenson et al., different dipping angles were not considered and only the extreme scenarios of injection of light fluid from top and bottom were considered. Furthermore, the sensitivity study did not account for any grain arrangements (heterogeneity) that could have affected the process efficiency. Therefore, while the Stevenson et al. study provided basic information, several gaps were required to be filled such as:

a) To conduct a study based on pore-scale physics instead of considering a pipe-flow mechanism.

b) To conduct better experiment and simulation result matching by conducting a simultaneous experiment and simulation study so that a sensitivity study can be performed directly.

c) To utilise the exact geometry of an experimental study to minimise the number of unknowns to reduce uncertainty.

d) To match results in real time so that a better comparison can be made.

e) Sensitivity can be performed based on different dipping angles along with the extreme scenarios.

f) Sensitivity can be performed based on pore arrangement to address local and global heterogeneity.

Regarding the experiments' results comparison, the simulation study conducted by Christie, Jones et al. (1990) can be set as a reference. This study reported the horizontal miscible displacement experiments conducted on the glass beads experiments, and the

images were processed. The simulation study was performed and the finite difference technique was used to solve Darcy's law and the convection– diffusion equations. The images of the simulation and of the experiments were compared to validate the simulation model. However, the comparison of the results could have been improved if the grains geometry of the experiments was known and more detailed physics was used.

Regarding using detailed physics, a pore-level simulation study conducted by Garmeh, Johns et al. (2009) can also be used as a reference. The pore-level simulation was performed through solving the Navier–Stokes equations and the convection–diffusion equation using COMSOL software to examine the origin of scale-dependent dispersion of fluids mixing. However, the geometric pattern of porous media used in that work was not the experimental geometry so experimental results cannot be truly verified.

CHAPTER 3   RESEARCH METHODOLOGY

3.1 Introduction

This chapter describes the procedures adopted in the research study to meet the research objective of determining the effects of different parameters on the gravity-dominated miscible process at pore scale. This objective was attempted to be met through visual experiments and numerical simulation at the pore-scale level.

Based on the literature review in Chapter 2, the glass micromodel method was selected to conduct the pore-scale visual experiments so that grains/pore/throat size and/or geometry could be adjusted. Therefore, it was required to conduct experiments with appropriate fluids and at various dipping angles. A detailed description of activities to meet this objective is described in this chapter.

The pore-scale experiments needed to be simulated using the same porous geometry instead of a geometry based on average properties. In addition, pore-scale physics based on partial differential equations was required to be used instead of Darcy's law or averaged pipe-flow equations. Following the comparison between experimental and simulation results, a sensitivity study was required to be conducted. This study would provide information regarding the parameters and configurations that affect the gravity-dominated miscible displacement process. A brief overview of the methodology adopted in this research is summarised in Figure 3-1.
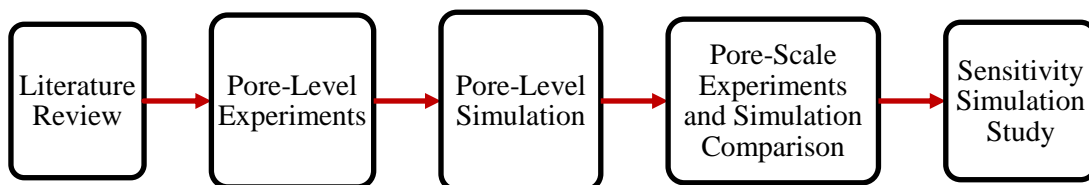
Figure 3-1: Methodology Adopted in the Research Work

3.2 Detailed Methodology

In the following subsections, details of the methodology shown in Figure 3-1 are described.

3.2.1 Literature Review Methodology

The literature review for the present research is divided into the following sections:

1. Literature review for gathering fundamentals of the process and for problem identification.

2. Literature review for experiments (selection of the experimental method).

3. Literature review for experiments (gap identification in previous visual gravity-dominated miscible studies).

4. Literature review for simulation (gap identification in simulation studies).

An initial literature review was conducted to signify the importance of the gravity-dominated miscible process. Based on this information, the scope and objective of the present research was set to conduct pore-level visualization and simulation studies.

After the problem was defined and the objective was fixed, a literature review was conducted to determine the best method for the visualization studies. The methodology adopted in this regard is shown in Figure 3-2, which shows that a literature review was conducted to understand the various different options available for pore-level experiments. The literature suggests that the visualization of a process can help to understand the process as it offers a method of direct analysis. Various visual techniques and their history were then explored. The advantages and disadvantages of these methods were explored in Chapter 2. The literature review recommends the glass micromodel method for visual experimental study due to its advantage of allowing the arrangement of grains of desired size, shape and position that can remain fixed for other experiments. Besides, glass wettability resembles to sandstone reservoir as discussed in section 2.1and glass is also a transparent medium that allows clear visual observations.

Glass Micromodel
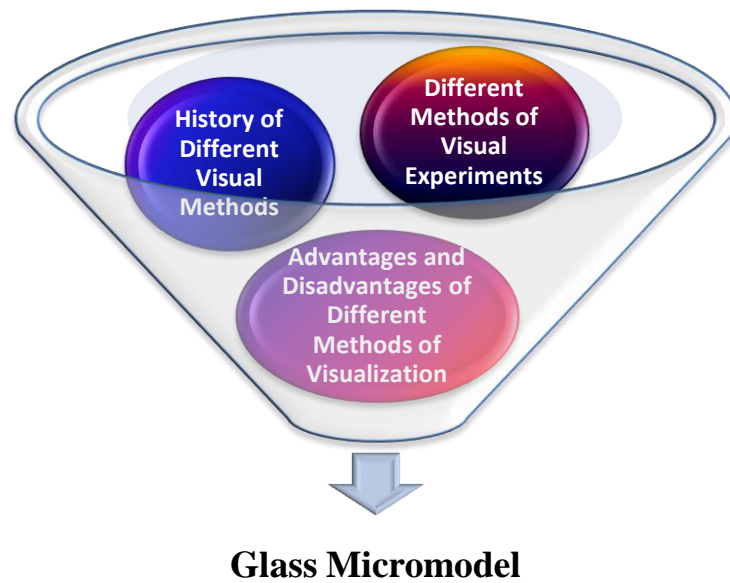
Figure 3-2: Methodology to Determine Appropriate Visualization Method for Experimental Study

Following the selection of the experimental method, the advances of research in the domain of miscible displacement in horizontal and vertical modes of injection were explored. Various studies are mentioned in Chapter 2 in this regard. Several fundamental immiscible experimental studies are also covered in this literature review. This review enables to identify the gap in the previous experimental studies.
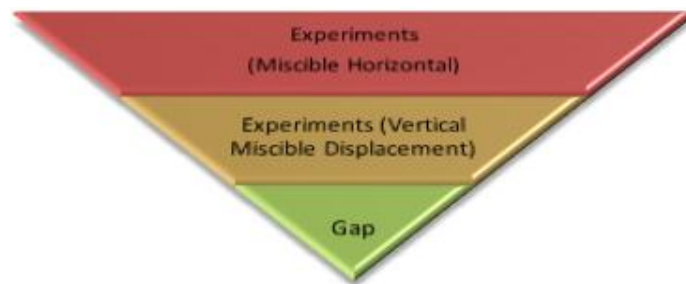
Figure 3-3: Methodology for Gap Identification (Experimental Studies)

The literature review on numerical simulation was also conducted and different methods of simulating pore-level mechanisms were explored. Examining the literature helped to deduce that a method should be adopted which utilise the true geometric features of the porous pattern instead of approximating the grain/pore size and distribution. Literature review also suggested that a more accurate and advanced simulation option should be used that did not rely on averaged pipe-flow equations.

3.2.2 Pore-Level Experiments' Methodology

New lab facilities needed to be developed so experiments for gravity-dominated miscible displacement could be conducted. Therefore, a methodology shown in Figure 3-4 was adopted to construct the required lab facilities.
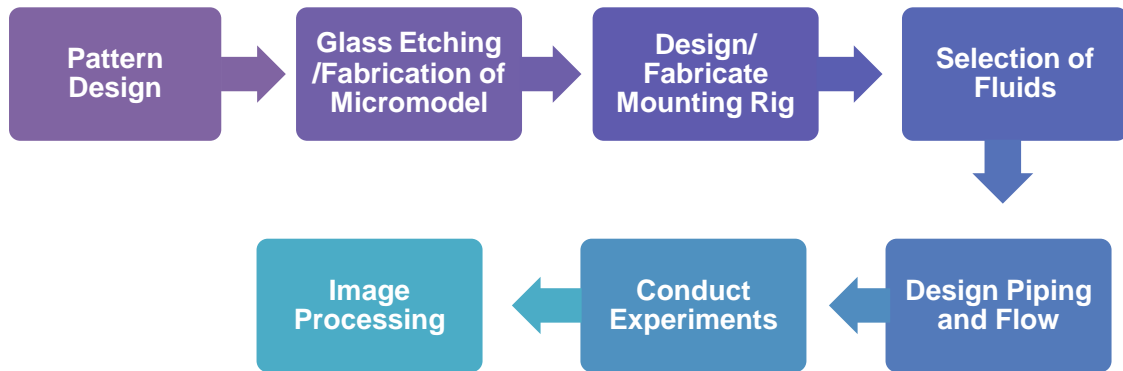
Figure 3-4: Methodology for Experimental Facilities Development

Figure 3-4 shows that the facilities development activities began with the design of a porous pattern so that the grains arrangement could be controlled and the desired geometry could be obtained. Patterns were designed through MATLAB software and the details will be given in section 4.1.1.1. The designed patterns were then etched onto the glass plates and fused with another plain glass plate. After the preparation of the glass micromodel, an experimental rig/fixture was required to hold the micromodel and to allow experiments at different dip angles in x-y planes to be performed. The experimental rig was designed so that the model could be tilted in either x-y and y-z plans. Tilting capabilities of the rig in y-z plane could be utilised for future research studies. Figure 3-5 shows the angular tilting in different planes.
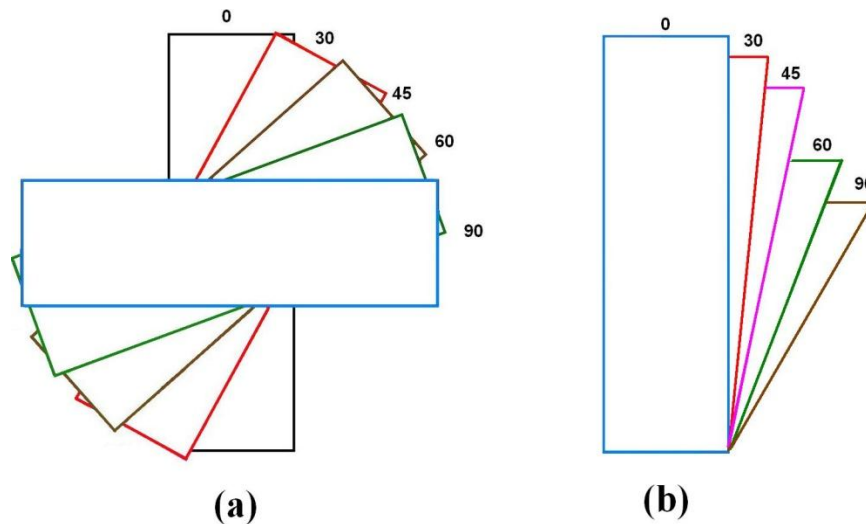
Figure 3-5: Angular Tilting of the Model in (a) x-y plane (b) y-z plane

In addition, the rig was designed in such a way that micromodels of different dimensions could be mounted and rotated at a desired angle and plane. The details of this design can be found in section 4.1.2.

The selection of fluids for the experimental study was also an important aspect of the experimental methodology. Miscible operations in the field are usually referred to as a gas-injection process; however, when it comes to lab visual experiments, it seems difficult to visualize a gas becoming miscible in the liquid. Therefore, most of the visual experimental studies in the past have relied on miscible liquids rather than on studying a gas and liquid system (Mahmoud and Rao 2007). The same approach was adopted in this study. In this regard, the injecting and inplace liquids were selected based on their comparable density differences and mobility ratios. The injected fluid was dyed so that its concentration could be estimated in a colourless inplace fluid.

The design of fluid flow in the experimental set-up was an important aspect to achieve the desired operational parameters. Thus a piping and flow design was designed, and the important instrumentation required—including the pump, piping connections and fittings—was procured and assembled according to the piping plan. The details are given in section 4.1.4 of Chapter 4.

Various flow visualization experiments were conducted at different angles and at desired flow rates. During each experiment, a high-definition movie was taken and images were captured at particular time intervals. These images represented the

distribution of dye in the porous domain; however, the actual concentration could not be estimated manually. Thus a program was developed in MATLAB to process these images and to assign a colour coding to the original image so that the concentration of the injected fluid could be estimated. The image processing will be discussed in section 4.1.6.

3.2.3 Pore-Level Simulation

A methodology was adopted in the present research so that the original features of the porous geometry would remain intact. In addition, pore-scale physics was used to simulate the process efficiently so that sensitivity studies could be performed with more confidence. Furthermore, visual features were utilised for better understanding of the process. The simulation studies were performed using COMSOL, a finite element analysis software, and the methodology adopted in simulation studies was divided into the following three parts:

1. Development of the simulation model.

2. Simulation and experimental results comparison.

3. Sensitivity studies.

3.2.3.1 Development of the Simulation Model

The geometry of experimental patterns, generated by MATLAB, was imported in COMSOL and the pore-scale physics was assigned. This importing was conducted so that the geometric features of the original pattern remained undisturbed and the geometric scale remained unchanged. The initial and boundary conditions for the defined equations were assigned and basic fluid properties such as density and viscosity were provided. Meshing was performed in the flow domain and the numerical adjustments and time stepping were conducted to perform numerical simulations. The details of the numerical model can be found in section 5.2 of Chapter 5.

3.2.3.2 Simulation and Experimental Results Comparison

After the development of the simulation model, the experiments conducted on the micromodel were simulated, and the simulation results were compared with the processed experimental results. Chapter 5 discusses this comparison in detail.

After the experimental and simulation results were compared, a study conducted by Stevenson (2004) was simulated so that a comparison could be made between previous methodology and the methodology adopted in the present study.

3.2.3.3 Sensitivity Studies

The Sensitivity studies were performed so that the effects of different parameters on miscible displacement with gravity domination could be identified. It includes effects of angular dip on fluid properties (density and viscosity contrast), the domain velocity and grains arrangement. For the sensitivity study on the porous arrangement, different sets of porous patterns were constructed to study both local and spatial heterogeneity effects.

CHAPTER 4 Visualization Studies

This chapter is divided into two parts. In the first part, the fabrication of experimental facilities is presented along with the experimental procedure adopted to conduct the experiments. In the second part, the results of the flow visualization experiments are discussed.

4.1 Experimental Facilities Construction

The visualization experiments were required to be conducted on a glass micromodel and therefore their preparation was considered to be of prime importance. Similarly, the construction of the experimental rig was equally important to ensure that the experiments were conducted on the desired conditions. In the sections below details of the glass micromodel preparation, the experimental rig construction and the experimental procedure followed are discussed.

4.1.1 Glass Micromodel Construction

4.1.1.1 Pattern Design

The designing or selection of the grain pattern was the first step of the micromodel construction. The selected grain pattern was intended to be etched onto the glass so that experiments could be performed. The grain pattern could either be a thin section of porous rock or a designed pattern. A thin section of porous rock considers the exact porous geometry and heterogeneities; however, this cannot be replicated during the simulation studies due to complexities of the porous geometry. Attempts were made in the present research to use ScanIP and ScanFE (version 3.1) software packages so that a thin section could be exported to the finite element simulation packages, but due to present technological and computational/memory limitations this approach was found to be unfeasible and was thus not adopted. A simplified approach was therefore adopted and a MATLAB program (Appendix A1) was used to construct a series of circles to act as grains and the spaces between the circles to act as pores. Since the grain/throat arrangements were controlled in the program, the exact grain patterns could be used in the simulation study to explore further mechanisms.

The MATLAB program was written so that the radius (r) of the circles is provided and the distance between any two consecutive circles becomes normally distributed with

provided mean (m) and standard deviation (std) value. In addition, the number of circles in the x and y direction can also be controlled in the program. The full MATLAB program is provided in Appendix A1. The program shows that, the information such as the number of circles in the x (n_x) and y (n_y) directions, coordinate of the first circle's centre (x_1, y_1), the radius of circles is required to be provided. In addition, the mean and standard deviation of the distance between the centres of any two circles is also required to be provided. Based on the defined number of circles in the x and y directions, the number of total connections (n_y-1, n_x) + (n_y, n_x-1) is determined and equal number of random values are generated with a specified mean (m) and standard deviation (std) and are stored in a vector. Once this vector is obtained, the coordinates of other circles' centres are determined by the vertical and horizontal concatenation along the vector. Once the coordinates of circles are determined, the circles are plotted with a given radius (r). Figure A2-7-1 in Appendix A2 shows the schematic arrangements of the circles' arrangement. Using this approach, two grains patterns were designed and named as pattern 1 and pattern 2 in this study. Pattern 1 is a slightly relaxed pattern, whereas the grain arrangement in pattern 2 is rather tight. The values used for constructing these patterns are tabulated in Table 4-1, and the histogram of the distribution of distances between the centres of the circles in the two patterns is shown in Figure A2-7-2 Appendix A2. The schematics of the two patterns are shown in Figure 4-1.
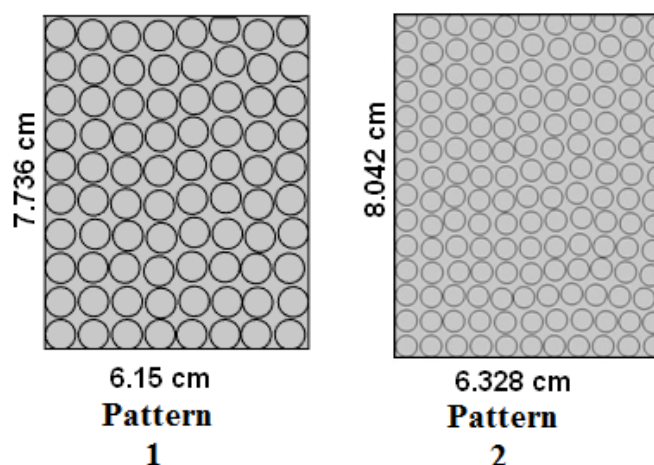
Figure 4-1: Schematics of the Patterns used in the Experimental Study

Table 4-1: Geometric Arrangements of the Two Patterns Designed

Property	Pattern 1	Pattern 2
Grid Size (n_x x n_y)	8 x 10	11 x 14
Radius of Circles (cm)	0.35	0.25
Mean Distance between Centres of Circles (cm)	0.77	0.58
Mean Distance between Circles (cm)	0.77–0.7 = 0.07	0.58–0.5 = 0.08
Standard Deviation (cm)	0.025	0.0266

4.1.1.2 Transferring Image from MATLAB to Paintbrush

The MATLAB-generated image, comprised of grains needed to be adjusted. The inlet/outlet connections were also required to be drawn. This was performed with Microsoft Paintbrush. However, it was observed that if the MATLAB image was exported or open in MS Paintbrush, then the grain geometry and scale became distorted and did not retain the actual features as produced by MATLAB. Therefore, in order to retain the actual geometry and scale, an indirect workflow was adopted, as shown in Figure 4-2.

Figure 4-2: Workflow adopted to import actual geometry from MATLAB to MS Paintbrush

Figure 4-2 shows that in order to retain the actual geometry, scale and shape, the MATLAB generated images were first saved to different Adobe packages such as Illustrator, Acrobat and Photoshop. The image in Photoshop was adjusted as a photonegative image of the actual pattern in which all porous areas were assigned white colour and the grains were assigned black. The image was then saved in .jpg format. When the image was then opened in Microsoft Paintbrush, it was adjusted to exactly the same scale as produced by MATLAB.

Inlet/outlet ports and dead spaces between ports and the grains were drawn in Microsoft Paintbrush. The dead volume ensured uniform distribution of the injected fluid in the

porous domain, and so inlet/outlet ports remained separated from the grains and a constant frontal velocity could be achieved within the porous domain. Figure 4-3 shows the areas assigned for the dead volume in the pattern design.
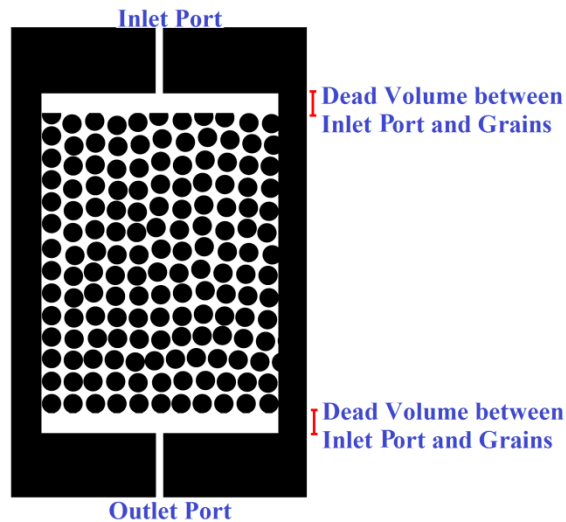
Figure 4-3: Dead Volumes in the Pattern

4.1.1.3   Transferring Pattern to a Photoresist Film

The generated photonegative image was printed on a transparent plastic film. In the present study, AccuArt, the transparent film of IKONICS Imaging (IKONICS-Imaging 2013), was used. The image was printed using an ink jet printer so that the distribution of ink was uniform and no pinch holes remained in the image. This printed image on the transparent film is referred to as 'the artwork' in this thesis.

The artwork was then transferred onto an ultraviolet (UV) light-sensitive photoresist film. In the present study a 4 mm photoresist film, RapidMask (IKONICS-Imaging 2013), was used. This photoresist film has two sides: a shiny side with a layer of photopolymer deposited below and a second side, which is a smooth slip sheet side to cover the photopolymer. Both the shiny and soft sides are protected with a sticky protective film to prevent any damage before application. Figure 4-4 (A) shows the schematic of a photoresist film.

(A)   (B)
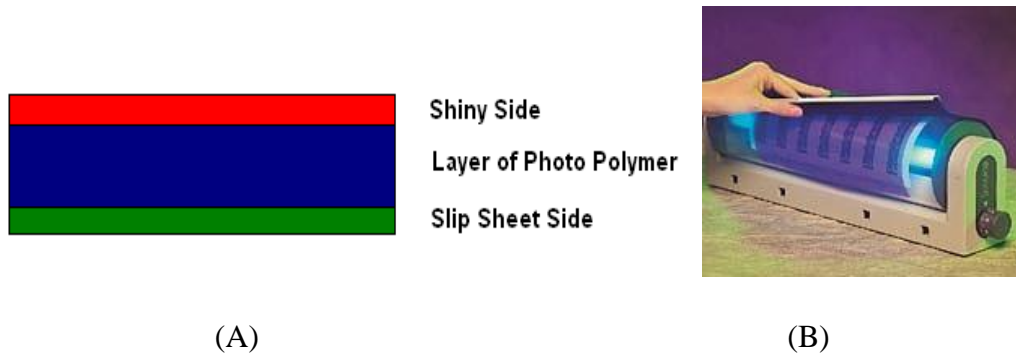
Figure 4-4: (A) Schematic of a Photoresist Film, (B) UV Light Exposure Unit

When the artwork is placed in close contact with the slip sheet side of the photoresist and UV light is exposed, the light passes through the empty areas (or assigned white in the photonegative pattern) and makes those areas brittle. Care was needed so that the contact position remained the same throughout the UV-exposing process. If this contact changed, the UV light may have exposed some unwanted areas and made them brittle too. Therefore, a UV exposure unit of IKONICS Imaging, Letralite, (IKONICS-Imaging 2013) was used. This unit has a cylindrical compression frame that keeps the artwork and photoresist in the same position and allows a uniform exposure of UV light via a 25 watt black fluorescent light bulb. Figure 4-4 (B) shows the UV exposure unit. The artwork and photoresist were orientated so that the UV light would pass though the empty spaces of the artwork first and then strike the photoresist film. Upon the exposure of the UV light on the film through the empty areas of the artwork, the colour of the exposed areas changed from green to blue and became brittle. It was necessary to ensure that enough energy was transmitted to the film via the UV exposure light to make it brittle, but the overexposure of the UV light made some unwanted portions brittle as well. Therefore, the optimised UV light exposure time in the present study was found to be 60 seconds.

4.1.1.4 Application of Photoresist on Glass

After the UV exposure, the photoresist was required to be applied on the glass for pattern etching. The glass was first cleaned with a glass cleaner so that all the fingerprints and dirt marks were removed. The protective film on the slip sheet side of the photoresist film was then removed. A small amount of water was sprinkled by a water sprayer onto the uncovered photoresist and onto the glass. This sprayed water helped to avoid immediate sticking of the film on the glass as it required adjusting the

position of the photoresist. Once the position of the photoresist was finalised, the water was wiped out with a ruler or any straight, sharp object. The pasted photoresist on the glass was allowed to rest for 5-10 minutes.

4.1.1.5 Sandblasting

Once the photoresist was pasted to one side of the glass surface, the glass was ready to be sandblasted and etched. In the past, glass micromodels were usually etched with hydrofluoric acid (Mollaei 2005), making the etching process hazardous. In the present study, the pattern etching was achieved through sandblasting process which is a safe approach to glass etching.

The protective shiny film of the photoresist was removed and the glass was placed in the sandblaster. The pressurised sand collides with the glass, removes the brittle photoresist portions and etches the glass. An optimum pressure is required for uniform etching. If the exposing pressure is too high, it may uncover some of the areas that are not supposed to be etched. However, on the other hand, if the pressure is too low, it may take a long time to etch. The inlet and outlet connections need to be over-etched to create a deep cut so that the needle can pass through them after the fusing job is completed. The optimum parameters identified in this research study are listed in Table 4-2.

Table 4-2: Optimum Parameters to Prepare Glass Micromodel

Parameter	Value
Photoresist film thickness	4 mm thick
Time of UV exposure on the photoresist film	1 min
Sand grain size	Zircon sand 150 micron
Pressure of sandblasting	30–35 psi
Exposure time of sand on the glass plate	4–6 sec/cm

4.1.1.6 Fusing Glass Plates

Once the sandblasting on the glass plate is complete and a pattern etched, the glass needs to be fused with another plain glass plate so that fluid can flow through the pore spaces created by the etched channels and the plain glass plate. This fusing was performed in a programmable Labecs' CEMLL Muffle Furnace (Labec 2013) with fully insulated walls which limit the loss of furnace heat to the surroundings and which allow for the cooling of the specimen within the furnace.

A sensitivity study was conducted which signifies the importance of rate of temperature increment during the whole fusing operation and soaking time at the fusing temperature. This study was important as under-fusing may not bound the two glass plates firmly and over-fusing might block the pores. Out of the different schemes used, the best configuration for fusing the two glass plates is shown in Figure 4-5, which shows the rate of temperature increment and actual temperature with respect to time. The figure shows that the temperature was ramped to a higher rate of 10°C/min until it reached 200°C. Once the temperature reached 200°C, the rate of temperature increment was decreased from a rate of 10°C/min to 2°C/min. This rate remained constant until the temperature reached the fusing temperature of glass plate. In the present study the fusing temperature of glass was approximately 700°C. This temperature could be varied $\pm\ 20^{o}$C depending on the type and nature of the glass. After the temperature was raised to the fusing temperature, the glass plates were rested at this temperature for at least 10–20 minutes. This soaking time was required to ensure good fusion between the two glass plates. After soaking, the furnace was shut off and the glass plates were left inside the furnace for at least 10–15 hours to cool down. Any sudden decrease in temperature causes the glass to break.
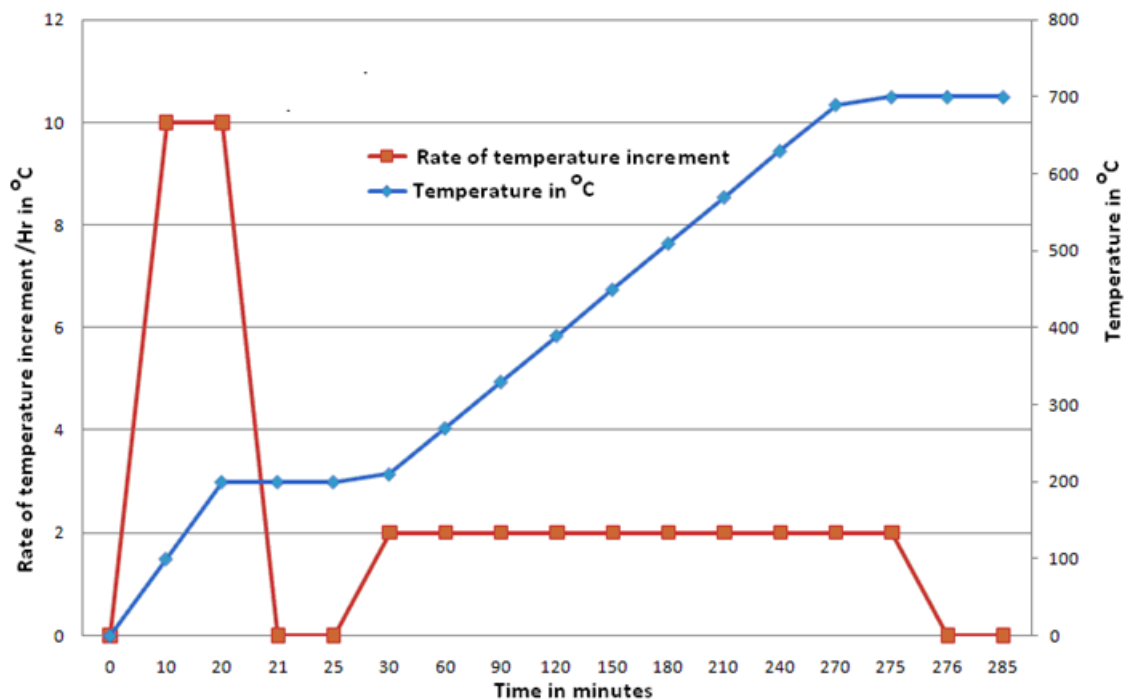
Figure 4-5: The Rate and Temperature Increment for Fusing Glass Plates

4.1.1.7 Mounting Syringe Connections

As mentioned in section 4.1.1.5, the inlet and outlet connections were over-blasted to provide sufficient depth so that needles could be inserted after the fusing operation. Thus two needles were cut according to the length of the inlet/outlet channel and inserted in the ports. Nano470 IC80 visible and UV sensitive load-bearing glass glue was used to glue the needle to the glass so that no fluid would leak out from the model. Nano470 IC 80 is a high-strength glass and metal glue that sets with the application of UV or white light.

4.1.2 Construction of Micromodel Holding Rig

To hold the glass micromodel in any dipping configuration, a special rig was designed and fabricated. This rig could hold glass plates of various widths and lengths and allowed different experiments at flexible degrees of angular positions to be performed.
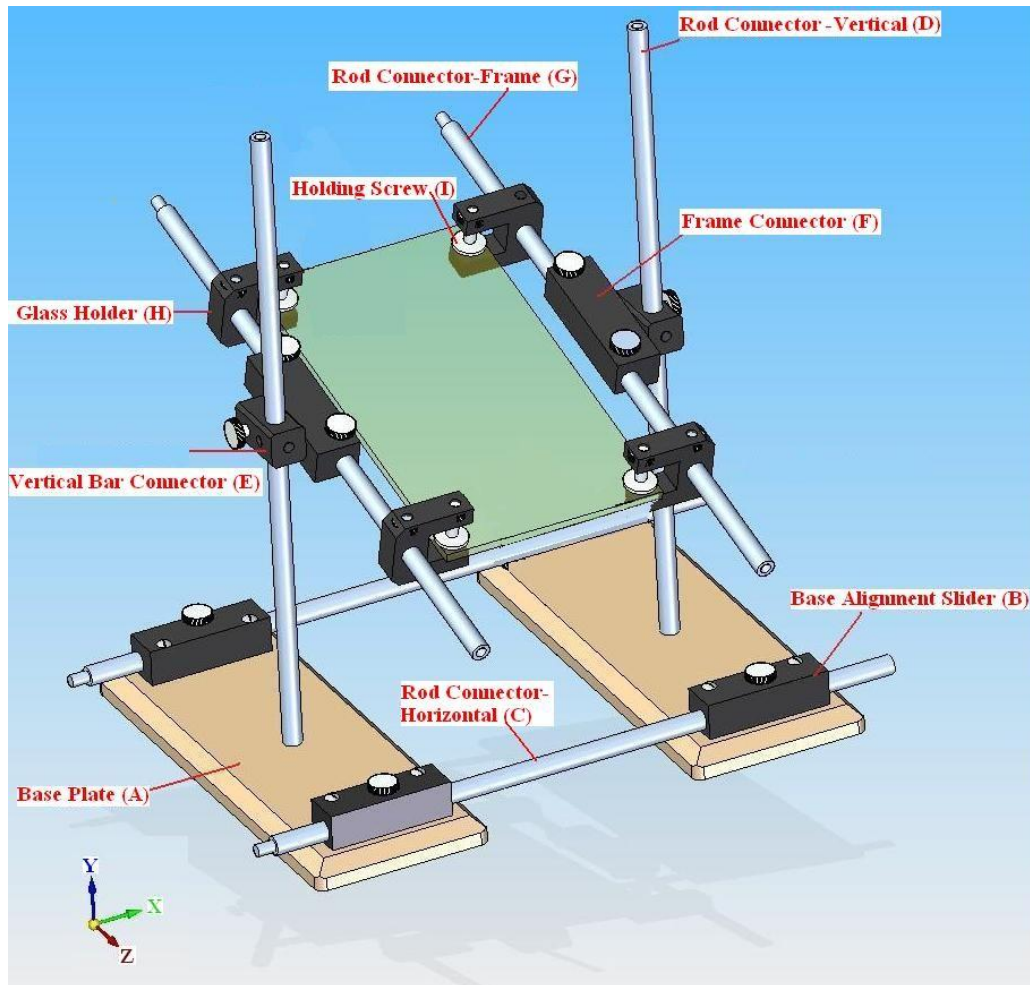
Figure 4-6: Schematic of the Designed Rig

The holding rig was designed to be fabricated by a stainless steel and PVC structure. All the designing of the structure was conducted using SolidWorks software. Figure 4-6 shows the schematic of the designed rig. This Figure shows that the rig was supported by two stainless steel base plates (A). Each of the base plates was provided with two base alignment sliders (B). The base alignment sliders were designed so that a stainless steel rod (C) could pass through them. In addition, a screw was provided on each of the base alignment sliders to fasten the position of the inserted rod.

Two rods (C) were inserted in each of the two base alignment sliders of one of the base plates. Each rod was inserted so that it ran through the corresponding base alignment slider of the other base plate. The provided screw of the base alignment sliders was fastened to adjust the distance between the two base plates. The ends of the inserted rods were threaded which allowed extension of the length so that other rods could be

attached. Thus, the distance between the two base plates was flexible. A hole was drilled in each of the two base plates so that a rod (D) could be connected in a vertical direction. The two ends of this rod were also threaded which allowed further extension of the length. A vertical bar connector (E) was then attached to each of these rods with the help of a screw. Each of the vertical bar connectors (E) was attached to a frame connector (F), also with the help of a screw. This frame connector could be rotated between 0° to 180° and it was designed so that a rod (G) could pass through it. This rod was also threaded at their ends which allowed further extension of the length. A glass holder (H) was designed so that it could be attached to the rod (G) and could hold a glass piece with the help of holding screw (I). This designed assembly allows to hold a glass piece of up to 9 kg with a maximum size of 1000 mm x 250 mm x 25 mm. This assembly allows rotating a glass model in the *y-z* plane as shown in Figure 4-7. A detailed design of this rig is described in Appendix B.

(A)   **(B)**
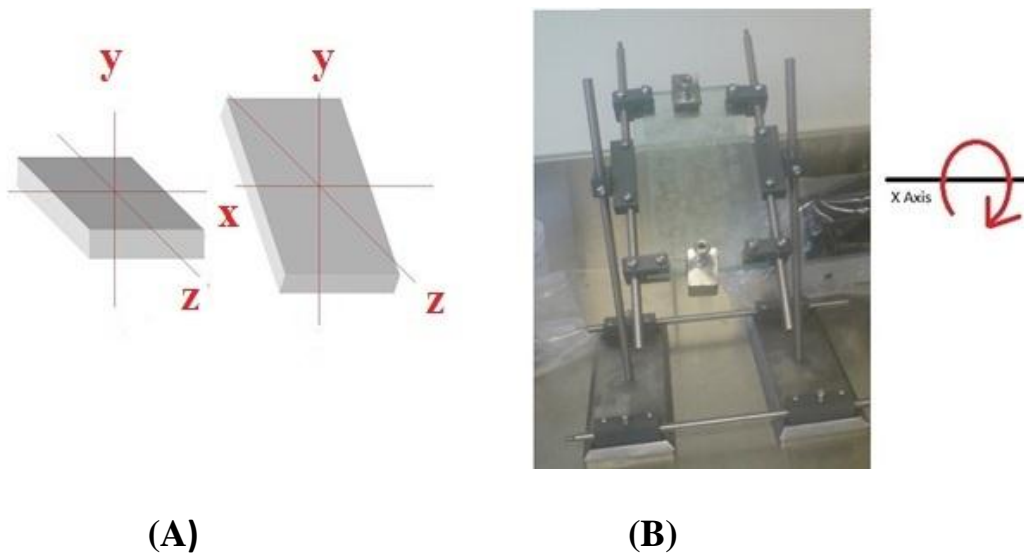
Figure 4-7: Tilting of the Micromodel in *y-z* Plane (A) Axis Representation (B) Fabricated Rig

Two holes were drilled in one of the two base plates (A) and screws were inserted to fix the whole rig assembly on an angle plate. This allows the whole rig to be rotated in the *x-y* plane as shown in Figure 4-8.

(A)   **(B)**
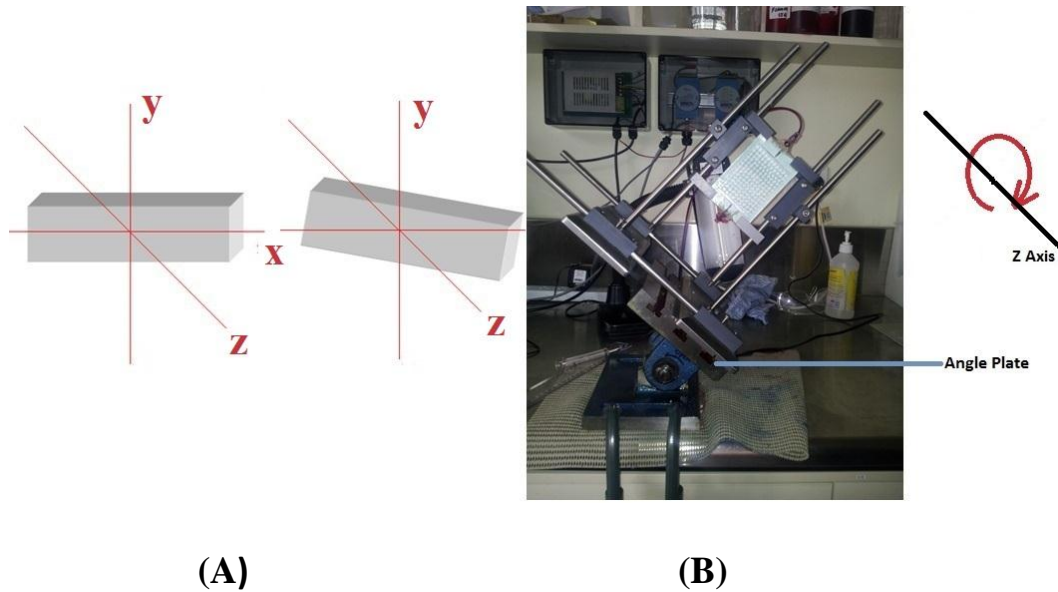
Figure 4-8: Tilting of the Micromodel in *x-y* Plane (A) Axis Representation (B) Fabricated Rig

4.1.3   Fluids used in Experimental Studies

The selection of two miscible liquids for the injecting and inplace fluids was performed so that their density and viscosity ratios were in the realistic range of the applied field processes. Fayers, Hawes et al. (1981) summarises the viscosity and density contrast between a few North Sea reservoirs and CO_2 at reservoir conditions, which is given in Table 4-3. This table shows that in North Sea reservoirs, the density ratios range between 1.3 and 0.7 and the mobility ratios range between 4 and 20.5. Miscible displacement in the field is usually a gas-injection process (for example, CO_2) in the oil formation. The phase diagram of CO_2 gas is shown in Figure 4-9, which shows that CO_2 in high pressure and temperature conditions behaves as supercritical fluid. Carbon dioxide gas at reservoir conditions is a supercritical fluid and its density could be lower or slightly higher than the inplace oil (Blunt, Fayers et al. 1993) depending on various parameters such as oil density, reservoir pressure and temperature. Since CO_2 is in supercritical form, it forms a single phase mixture with the in-situ oil if miscible conditions exist. Besides, gas is a colourless fluid and so the miscible front cannot be observed in a laboratory as shown in our previous study (Mohiuddin and Haghighi 2011). Based on these limitations, several past studies (Mahmoud and Rao 2007) used two liquids to study miscible displacement rather than using a pure gas and liquid.

NOTE:
This figure/table/image has been removed
to comply with copyright regulations.
It is included in the print copy of the thesis
held by the University of Adelaide Library.

Figure 4-9: Phase Diagram of Pure CO_2 (Vermeulen 2011)

Table 4-3: Density and Viscosities Contrast of Different North Sea Light Oil Reservoirs (Fayers, Hawes _et al_. 1981)

Name of Reservoir	Forties	Brent	Ninian	Piper	Thistle
Reservoir Temperature (^{o}C)	90	93	102	80	102
Initial Reservoir Pressure, bar	220	410	450	240	410
Oil Density (ρ_o) , kg/m^3	750	570	790	750	760
CO_2 Density (ρ_{CO2}) , kg/m^3	570	770	780	720	760
Oil Viscosity (μ_o) cP	0.82	0.28	1.35	0.73	1.05
CO_2 Viscosity (μ_{CO2}) cP	0.04	0.07	0.07	0.05	0.07
Density Ratio (ρ_o/ρ_{CO2})	1.316	0.74	1.013	1.04	1
Mobility Ratio (μ_o/μ_{CO2})	20.5	4	19.29	14.6	15

Therefore, in the present study, iso-octane (0.51 cP, 0.69 kg/m³) and butanol (3 cP, 0.81 kg/m³) were selected as the injected and inplace fluid respectively so that their density (1.17) and viscosity ratios (5.88) were in the realistic range of the applied field processes. In addition, the fluids were selected so that the density and viscosity of the injected solvent would be less than that of the inplace solvent.

The iso-octane was dyed red by Sudan Red dye so that its concentration could be estimated in butanol. The dyed iso-octane was then filtered twice by a grade 4 filter

(Whatman filter paper Model 1004-150) so that the undissolved dye particles could be separated.

4.1.4   Piping and Instrumentation

To perform and control the experiments at the desired conditions, appropriate equipments were selected and the necessary piping connections were fabricated. The piping and instrumentation was designed so that a minimum length of pipe and number of instruments were used. This ensured minimum dead volume and leakage. In addition, a small length of piping was useful to control and deliver small flow rates to the micromodel. The schematic diagram of instrumentation arrangement is shown in Figure 4-10.

The inplace and injected fluids are required to be pumped into the glass micromodel. A syringe pump (New Era model NE1000) is used for the injecting fluids into the glass model at a desired injection rate, while the inplace fluid is injected manually. Five ml Luer-Lock male glass Sanitex syringes are used to inject the two fluids. Glass syringes are used because the plastic syringes expand when exposed to alcohol or hydrocarbons, which blocks the movement of the syringe plunger. Although the desired flow rate in the micromodel was very less, 5 ml syringe was used as the dead tubing volume was required to be filled with desired liquid. It is however noted that the inner diameter of the glass syringe was slightly reduces at the upper end of the syringe to have a good seal which could slightly affects the injection flow rates towards the end of experiment.

The Luer ends of the syringes provide a better seal compared to the normal end syringes. Cole–Parmer M/F Luer end tubing (diameter 1.6 mm) is used to connect the syringes to the micromodel. The female end of the tubing is connected to the glass syringes and the male end of the tubing is connected to the female connections (ports 1 and 2) of the three-way stop-cock valve (BD 394600). This valve can switch the flow between the two connected lines. Besides the two female connections, the three-way valve has one male connection (port 3) that can be connected to the needle connection of the glass micromodel. The outlet syringe connection of the micromodel is connected to the Luer end tubing and runs into the waste collector.
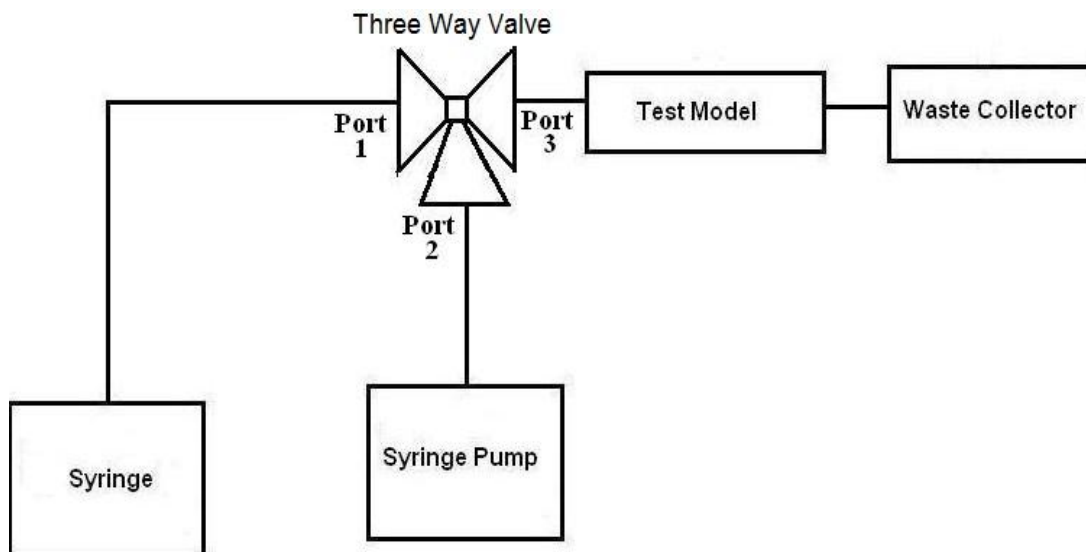
Figure 4-10: Flow Diagram

4.1.5 Experimental Procedure

Butanol, the inplace fluid, is first filled into one of the glass syringes and air bubbles are removed. The syringe is then connected to the female Luer end of the tubing and the male end of this tubing is connected to the port 1 of the three-way valve. The syringe is then pushed slightly so that only a small volume of butanol is purged through port 3 of the three-way valve. After this purging, the port 1 connection of the three-way valve is closed to open port 2.

Dyed iso-octane, the injected fluid, is then taken in another glass syringe and the air bubbles are removed. This syringe is then mounted to a syringe pump and the Luer male connection of the syringe is connected to the female Luer tube connection. The male end of this tube is then connected to port 2 of the three-way valve. This connection is in operation as the port 1 connection is already closed. The syringe pump starts to pump with a high rate until the iso-octane fills the whole tubing and the small volume of butanol is purged out through port 3, which is initially trapped in the three-way valve. These steps are conducted to remove air in the tubing and to fill the fluids in the respective line. Once the iso-octane starts to produce through port 3, the pumping of the iso-octane through the syringe pump is stopped, the port 2 connection is closed and the port 1 connection is in line again. A small volume of butanol is again purged out from port 3 to clear the iso-octane traces. At this stage both the lines are filled with respective fluid. Once this purging is done, the port 3 male connection of the three-way

valve is connected to the glass micromodel through the needle connection. The outlet connection of the micromodel is also connected to the waster collector via the Luer end tubing. A white paper is pasted on the underside of the micromodel and a light lamp is turned on to provide good illumination.

The glass micromodel is then placed in an upside-down position and butanol is forced to inject manually at a higher rate in the micromodel to fill the micromodel without air bubbles forming. Although care was taken, air remained trapped in some small pores. Following the saturation, the micromodel was placed on the experimental rig at the desired orientation. Subsequently, port 1 was closed to open port 2 and the injection fluid started to flow in the model with the adjusted flow rate.

Throughout the entire experimental process, a video film was recorded using a camcorder (Sony HDR XR550). At the end of the experiments the video was processed so that high-quality snapshots could be captured from the movie. The first snapshot was captured when the dyed fluid had just entered into the micromodel. This time was regarded as 'initial time' and the following images were captured with respect to this time. After a few hours, when no visual change was observed, the syringe pump was turned off. The syringe was removed from the syringe pump and the syringe's plunger was pressed manually with a high flow rate to saturate all the pores with the injecting fluid. When all the remaining iso-octane had pumped into the system, a final snapshot was captured. This final snapshot virtually represents the maximum concentration of the injected fluid in the system. This image serves the purpose of a reference image for the image processing and the details are described in the following section. After the completion of the experiment, acetone was pumped into the micromodel to purge both the injected and inplace fluid from the micromodel. High pressure air was blown into the micromodel to vaporise the acetone and to leave the clean micromodel.

4.1.6 Image Processing

The captured snapshots from the recorded video provide a brief qualitative overview of the concentration of the injected fluid in the porous domain. Therefore, to estimate the concentration in the porous domain some standard was required to measure the strength of the dye in the system. In order to assign a proper concentration profile, image

processing was required. Figure 4-11 shows the procedure adopted to process the image.
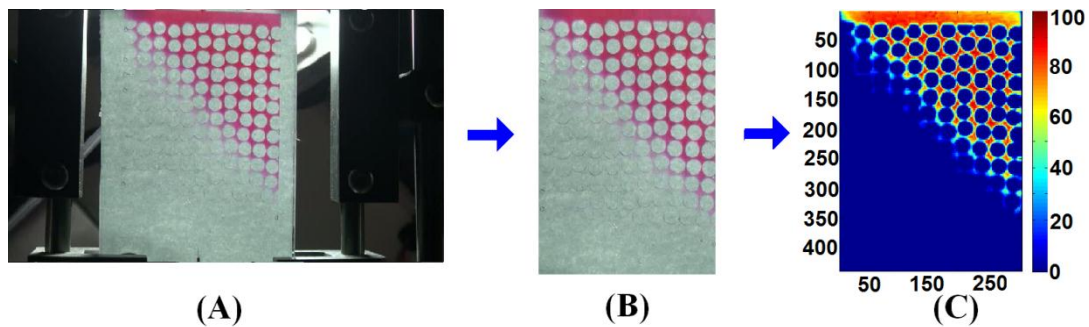
Figure 4-11: Image Processing of the Captured Snapshot

Figure 4-11(A) shows that the captured snapshot that contained some additional surrounding areas around the glass micromodel. As shown in Figure 4-11(B), these areas were required to be removed so that the processed image could only take the areas of interest into account. The same surrounding areas were removed in each snapshot of one experiment so that images of exactly the same dimension were produced. This operation of removing additional areas from the actual captured image was performed in Adobe Photoshop. Since the same image size was required for every single captured image, the final image was considered and its dimension was noted. A canvas size was selected in Adobe Photoshop to match the dimensions and was applied automatically to every single image of the same experiment. This exercise provided uniform-sized images to be captured in a single experiment. It is however to be noted that the image position in a single experiment stayed the same because the camera stand position remained fixed. The difference of image position in a set of experiments might have caused change in obtaining areas of interest. This ultimately resulted in the slight difference of image dimensions between the sets of different experiments.

The obtained images of the experiments—after the cropping shown in Figure 4-11 (B)—were required to be processed so that the saturation of the injected fluid in the micromodel could be evaluated. This processing was performed through MATLAB and the detailed program was written and is given in Appendix C. As shown in the program, the saturation of injected fluid at different time steps in each experiment was determined by comparing every image with a reference image. This reference image needed to contain the maximum saturation so that it showed the maximum value and

virtually behaved as 100% saturated with the red-coloured injected fluid. Therefore, at the end of every experiment, the micromodel was flooded manually with iso-octane until all of the pores were completely filled. An image was captured which served as the reference image. However, this exercise had limitations: absolute filling was not possible (especially in cases of high-tilt such as the 60° and 90° cases), and as small bubbles locked small pores, the invasion of an injected fluid was impossible, which gave an error for maximum saturation. Thus, difference in size of objects causes an error in image processing.

Additionally, the effect of lighting was also very important during image processing. Although care was taken so that the lighting effects remained consistent in every experiment, some small fluctuations in lighting were unavoidable because some experiments were completed in the day and some were completed at night. Due to these constraints, the processed image could provide only a rough estimate and thus the values derived after this exercise should not be treated as universally valid. The purpose of image processing was therefore to provide a rough standard when comparing experimental and simulation results.

The reference image described in the paragraph above was first loaded as a Red Green Blue (RGB) colourmap. The RGB colourmap was then converted into an equivalent Hue Saturation and Value (HSV) colourmap. This conversion was performed because HSV describes colours with more familiar comparisons such as colour type (hue), amount of grey/white (saturation) and brightness or lighting (value). After this conversion, all the saturation values of hue between 0.2 and 0.6 (that is, red colour) of the reference image were stored in a matrix. The maximum value in this saturation matrix was then assigned as the reference value of the highest saturation.

All of the remaining images were then processed and compared with the reference value to estimate the concentration of red dye in the micromodel. A colour mapping was assigned to estimate the concentration profile, as shown in Figure 4-11 (C).

4.2 Miscible Displacement Experiments

The miscible displacement experimental studies were conducted on glass micromodels with two different patterns as described in section 4.1.1.1. The two micromodels enabled the investigation of the fluid flow in different geometry. The experiments were

performed on both micromodel patterns at an angle of 0°, 30°, 45°, 60° and 90° with respect to the vertical. Iso-octane and butanol were used as the injection and inplace fluid respectively. The injection flow rates in two micromodels were required to be selected so that the flow of fluids in the porous domain would follow the similar domain velocity as in real oil reservoirs. The average velocity of fluids in the reservoirs is usually less than 1 ft/day or 3.5 x 10^{-6} m/s and dispersion mechanism dominates the in-fluid mixing (Stalkup 1983). However, the velocity near the wellbore is generally higher than 1 ft/day and convection is the dominating mechanism of fluid mixing (Stalkup 1983). Therefore, the injection rates were required to be chosen so that they represented the flow in both near wellbore and in the reservoir. In the present research study, the first micromodel was tested only in the reservoir flow domain and the second micromodel was tested both near wellbore and in the reservoir flow domain.

The calculations given in the following sections were performed on both micromodels to find the injection rate that corresponded to the domain velocity of respective wellbore and reservoir flow. The micromodel patterns calculations are divided into two categories depending on the area under consideration:

    a) Based on full domain.

    b) Based on the domain in which the grains are located.

Figure 4-12 shows the schematic descriptions of the two categories. In Figure 4-12 the full domain of the micromodels is represented by the area enclosed under the blue-and-black regions; however, the grains domain of the micromodel is represented by the area enclosed under the blue colour only.
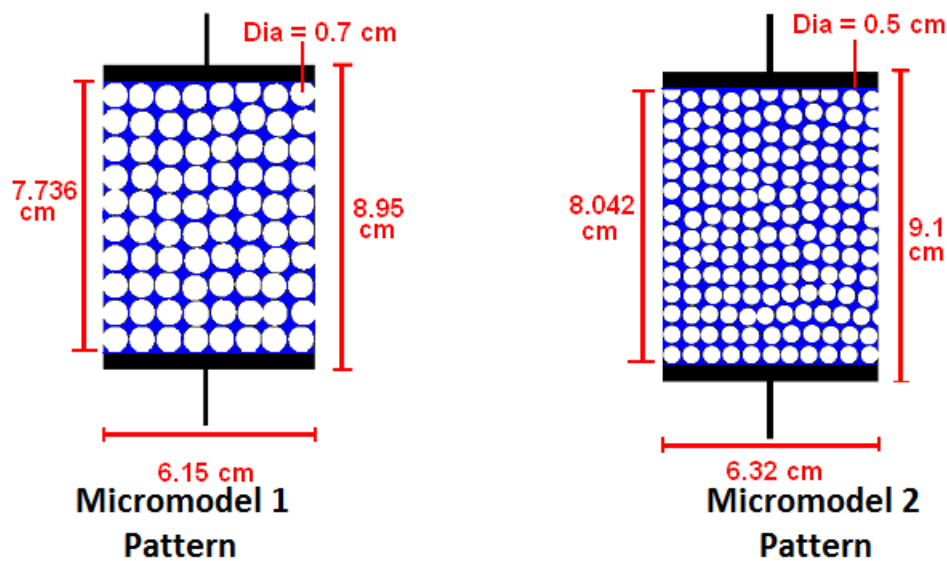
Figure 4-12: Schematic of the Patterns used in the Experimental Study

4.2.1 Calculations in the Full Domain

4.2.1.1 Total Pore Volume

The pore volumes of both glass micromodels were determined by flooding a dyed liquid into the porous domain through a syringe pump. The volume injected to fill the whole domain represents the total pore volume of a micromodel.

4.2.1.2 2Surface Area (Whole Domain)

The surface area of all the etched surfaces in the porous patterns was calculated through COMSOL software. The actual porous patterns were imported into the COMSOL software and the surface area was calculated through a surface integration option.

4.2.1.3 Depth

The depth of the micromodels refers to the average distance between the flat glass surface and the sandblasted etched surface in which the fluid flowed. The calculation of this parameter was required because the actual depth of cut after the sandblasting operation was unknown. This parameter was obtained through dividing the total pore volume by the surface area of the whole domain.

4.2.1.4 Cross-Sectional Area of the Inlet Port

The cross-sectional area of the inlet channel was determined by multiplying the width and the depth of the inlet port. The width of the inlet channel of both micromodels was

adjusted by 0.1 cm during the designing of the patterns. This cross-sectional area was used in the simulation study in order to specify the inlet velocity. Figure 4-13 describes the schematic of the width and depth of the micromodels and Table 4-4 summarises the calculation and values derived in considering the full porous domain.
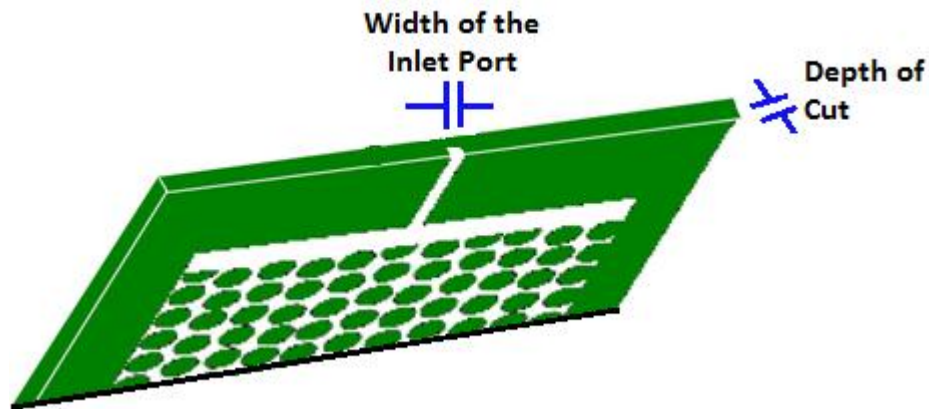
Figure 4-13: Schematic of 3-D View of the Micromodel

Table 4-4: Experimental Calculations Considering Full Domain

	Pattern 1	Pattern 2
Pore Volume total (PV) (cm^3)	1.2	1.25
Total Surface Area (TSA) (cm^2)	25	28
Depth (PV/TSA) (cm)	0.048	0.044
Inlet Cross-Sectional Area (Depth*Width of Port) (cm^2)	0.048*0.1 = 0.0048	0.044*0.1 = 0.0044

4.2.2 Calculations in the Grains Domain

The 'grains domain' of the micromodel refers to that region of interest where the grains are located. The dead area provided to stabilise the flow was therefore not considered. Figure 4-14 shows the actual porous domain of the two micromodels.
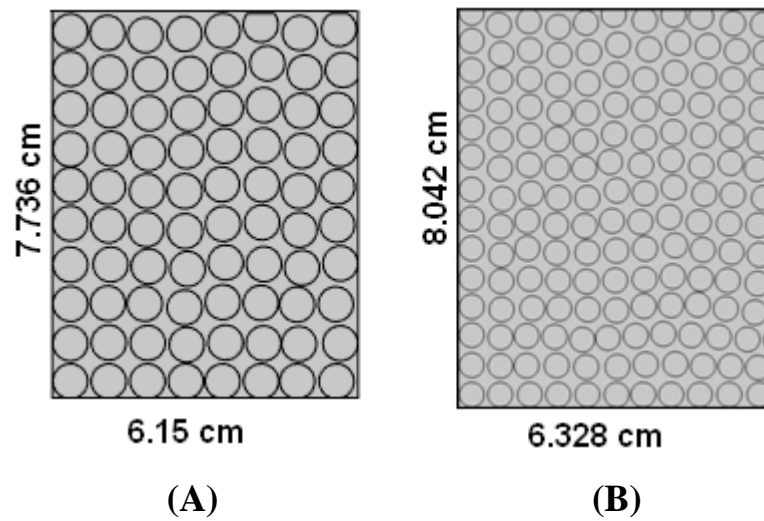
Figure 4-14: Grains Domain of the Patterns used in the Experimental Study (A) Pattern 1 (B) Pattern 2

4.2.2.1 Total Grains Area

The total grains area was obtained by multiplying the length and width of the area of interest. The dimensions of the micromodels as shown in Figure 4-14 was used in this regard.

4.2.2.2 Surface Area (Grains Domain)

A similar procedure was adopted to calculate the surface area of the porous domain through COMSOL software as was adopted for the calculation of the surface area of the whole domain (section 4.2.1.2). However, the area of interest was limited in the surface integration.

4.2.2.3 Porosity

The 'porosity' of the micromodels (as a ratio rather than a percentage) is defined as the ratio between the surface area and the total area, that is:

$$Porosity = \frac{Surface\ Area\ of\ the\ Grains\ Domain}{Total\ Area\ of\ the\ Grains\ Domain} \tag{4.1}$$

4.2.2.4 Effective Width

The 'effective width' is the average width available to the fluids to propagate in the grains domain. This can be obtained by using the following relation:

$$Effective\ Width = \ Porosity * Width\ of\ Micromodel \tag{4.2}$$

4.2.2.5 Grains Domain Velocity and Injection Rate Determination

The average velocity of the injected fluid in the grains domain was determined by the following relationship:

$$Grains\ Domain\ Velocity = \frac{Injection\ Flow\ Rate\ (from\ pump)}{Effective\ Width*Depth\ of\ Micromodel} \quad (4.3)$$

The grains domain velocity and injection flow rate are the two unknowns in equation (4.3). The injection flow rate was required to be adjusted so that it represented the flow in both near wellbore and in the reservoir. Therefore, a value of 0.005 cm³/min was selected for the injection rate of the first micromodel, which corresponds to the domain velocity of 2.21 ft/day (representing near wellbore condition). Similarly, for the second micromodel, the injection rates of 0.005 and 0.002 cm³/min were selected, which corresponds to the domain velocities of 2 ft/day (near wellbore region) and 0.8 ft/day (reservoir region) respectively. Table 4-5 summarises the calculation and values derived in the grains domain.

Table 4-5: Experimental Calculations Considering Grains Domain

Parameter	Pattern 1	Pattern 2
Total Area (Grains Domain) (cm²)	6.15 x 7.736 = 47.58	6.328 x 8.042 = 50.89
Surface Area (Grains Domain) (cm²)	17.2	21.2
Porosity (Grains area/Grains Surface Area)	0.36	0.42
Effective Width (Porosity*Actual Width) (cm)	0.36*6.15 = 2.22	6.328*0.42 = 2.64
Domain Velocity (for 0.005 cm³/min Injection Flow Rate)	0.005/(2.22*0.048) = 0.0469 cm/min = 2.21 ft/day	0.005/(2.64*0.044) = 0.043 cm/min = 2.03 ft/day
Domain Velocity (for 0.002 cm³/min Injection Flow Rate)	N/A	0.002/(2.64*0.044) = 0.017 cm/min = 0.81 ft/day

In order to verify that the selected injection flow rates represented the dispersion and convection domain, a relation developed by Perkins and Johnson (1963) was used. According to Perkins and Johnson (1963), a dimensionless number $\frac{V\sigma d_p}{D_o}$ decides the type of fluid flow in the porous medium. Where V is the domain velocity, σ is the inhomogeneity factor, d_p is the grains diameter and D_o is the diffusion coefficient between the fluids. According to Perkins and Johnson(1963), if the values of this dimensionless number is less than 50 then molecular dispersion will dominate in the transverse mixing. Values higher than this provide a convection-dominated flow. Therefore, the value of this dimensionless number was calculated for two micromodels. The velocity values were taken from Table 4-5, the diameter of grains for a particular micromodel was used from the geometric arrangement as shown in Figure 4-12, the heterogeneity coefficient was taken as "1" due to relatively simple geometry, and the diffusion coefficient of 6.57375 x 10^{-10} m^2/s between iso-octane and butanol was used. The complete discussion of the diffusion coefficient will be discussed in section 5.4.2**.**

The related calculation for Perkins and Johnson's dimensionless number is shown in Table 4-6 which shows that a flow rate of 0.005 cm^3/min in the first and second micromodel reflects a convection-dominated flow as the values of the dimensionless number exceed 50. However, the flow rate of 0.002 cm^3/min in the second model represents a flow of molecular dispersion as the value derived for the dimensionless number is less than 50.

Table 4-6: Calculation of the Perkins and Johnson (1963) Dimensionless Number

Model	Rate cm^3/min	Velocity m/s	Homogeneity Coefficient σ	Diameter of Grains (d) M	Diffusion Coefficient, D b/w two fluids m^2/s	$\frac{V\sigma d}{D}$
1	0.005	7.8E-06	1	0.007	6.50E-10	84.09
2	0.005	7.08E-06	1	0.005	6.50E-10	54.46
2	0.002	2.83E-06	1	0.005	6.50E-10	21.77

4.3 Experimental Results

4.3.1 Experiments Representing Near Wellbore Flow Rates

4.3.1.1 Experiment with First Model

Iso-octane was injected in the first micromodel at the constant flow rate of 0.005 cm^3/min. The injection was carried out at 0°, 30°, 45°, 60° and 90° with respect to the vertical. The snapshots at different time steps were taken during the experimental studies with different angles, as shown in Figure 4-15 (A). The results show that the propagation of front is fairly stable when the gravity is acting in the direction of flow. The gravity segregation helps to perform a uniform displacement in this case and the breakthrough time is delayed. However, when the micromodel was tilted, gravity override came into play and the early breakthrough of the injected fluid occurred. The breakthrough time became progressively shorter as the angular tilt increased. For the horizontal case (90°), the gravity override reached a maximum point and the breakthrough occurred within 30 minutes of operation. Few signs of viscous channelling along with gravity override were also witnessed in this case.

Figure 4-15 (B) and Figure 4-15 (C) represent the pre- and post-breakthrough saturation profile of the cases when iso-octane was injected in butanol at different angles, with the rate of 0.005 cm^3/min, in the first micromodel. The saturation at each step was calculated by processing the image. The snapshots in Figure 4-15 (A) shows that approximately 80% of insitu fluid was displaced in the vertical case before any breakthrough occurred; however, a complete horizontal system can recover just over 10% before breakthrough at the same injection rate. Through image processing, the estimate of unswept volume at the breakthrough was made. This showed that the unswept percentage at the breakthrough in 0°, 30°, 45°, 60° and 90° cases were 19.2%, 29.2%, 44.1%, 63.8% and 87% respectively. However, it is to be noted that at this flow rate, the front advancement was observed to be rather fast towards the end of the experimental study. This is because the inner diameter of the glass syringe reduces slightly at the upper end of the syringe to ensure a good seal. This minor change in the inner diameter of the syringe slightly disturbed the injection rate towards the end of this study after approximately 150 minutes of operation. Due to this experimental limitation

of the syringe used, the percentage values might be slightly overstated towards the end of the experimental study.

The post-breakthrough saturation profile in Figure 4-15 (C) shows that besides the reduction in the breakthrough saturation, the overall trend of the saturation profile of all angular tilts (except the 90° case) seem similar to each other. It reflects that the higher injection can ultimately produce similar recovery regardless of tilt angles if the tilt angle remains below 90°. This could be due to the use of a simplified porous geometry. When the tilt approaches this value, the gravity forces dominate and no further recovery is obtained.

Figure 4-15: (A) Snapshots of Experiments Conducted in the First Micromodel at Injection Rate of 0.005 cm^3/min (B) Pre-Breakthrough Profile (C) Pre- and Post-Breakthrough Profile

4.3.1.2 Experiment with Second Model

Iso-octane was injected in the second micromodel at the constant flow rate of 0.005 cm^3/min, which also demonstrates the near wellbore condition. The injection was carried out at 0°, 30°, 45°, 60° and 90° with respect to the vertical. The experimental results are shown in Figure 4-16. The snapshots captured during the experiments are shown in Figure 4-16 (A). The saturation profile of different experiments until the breakthrough is shown in Figure 4-16 (B) and the pre- and post-breakthrough saturation profile is shown in Figure 4-16 (C). The results show a similar trend to what was observed in the experimental study with the first pattern at the same rate. The propagation of front was fairly stable in the 0° case; however, the gravity override occurred when the tilt angle was increased and the breakthrough time was shortened compared to the preceding cases. Due to high injection velocity, the flow in the domain is convection dominated.

The post-breakthrough saturation profile in Figure 4-16 (C) reflects that if the injection is continued after the breakthrough, similar recovery can be achieved if the tilt angle is equal to or below 60°. Above 60° the gravity effects dominated and the injected fluid remained in the upper section of the domain, while the bottom section remained unswept no matter how much time was allowed. Estimation through image processing shows that the percentage of unswept volume at the breakthrough in 0°, 30°, 45°, 60° and 90° cases were 17.2%, 31.8%, 41.5%, 58.7% and 93.4% respectively.
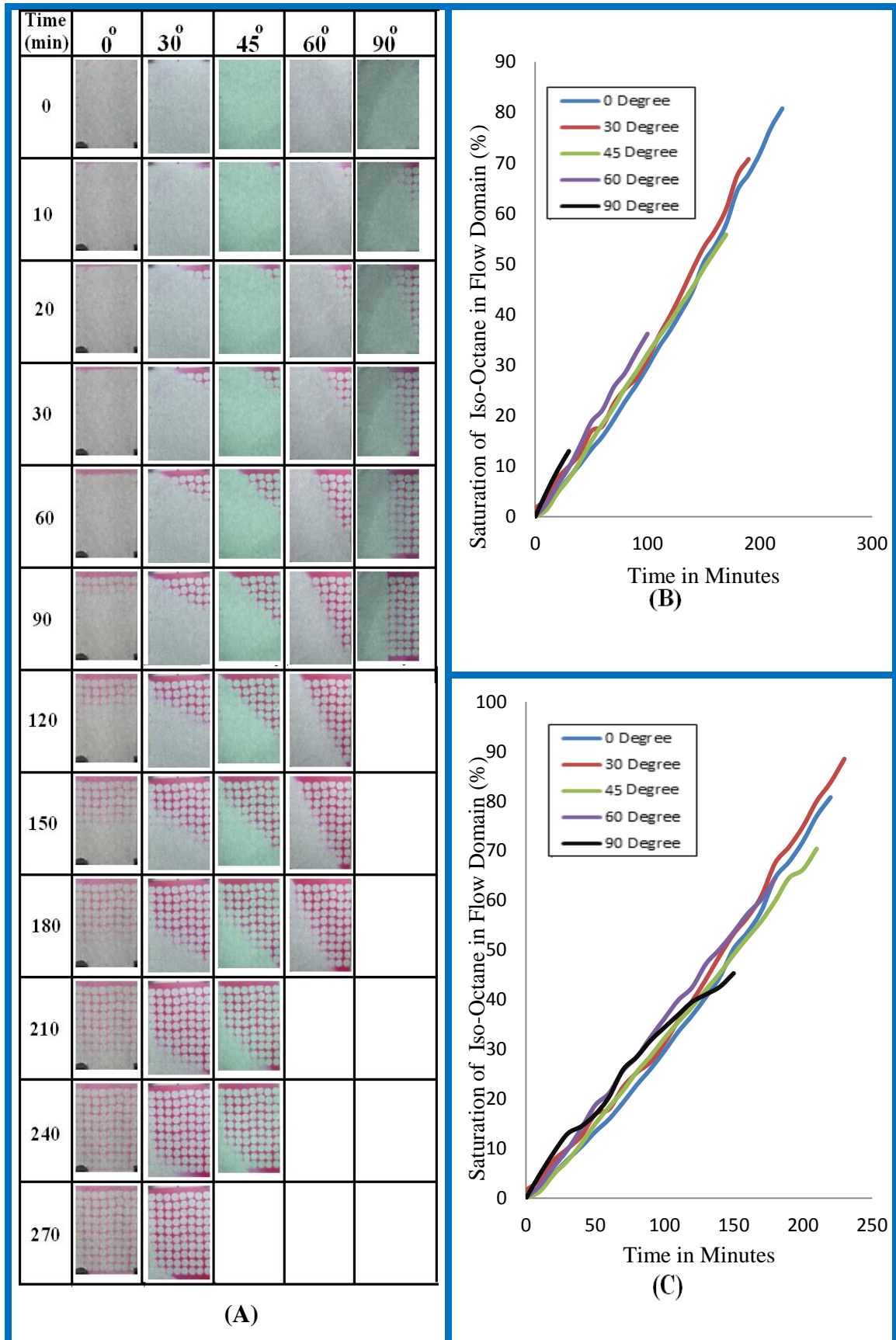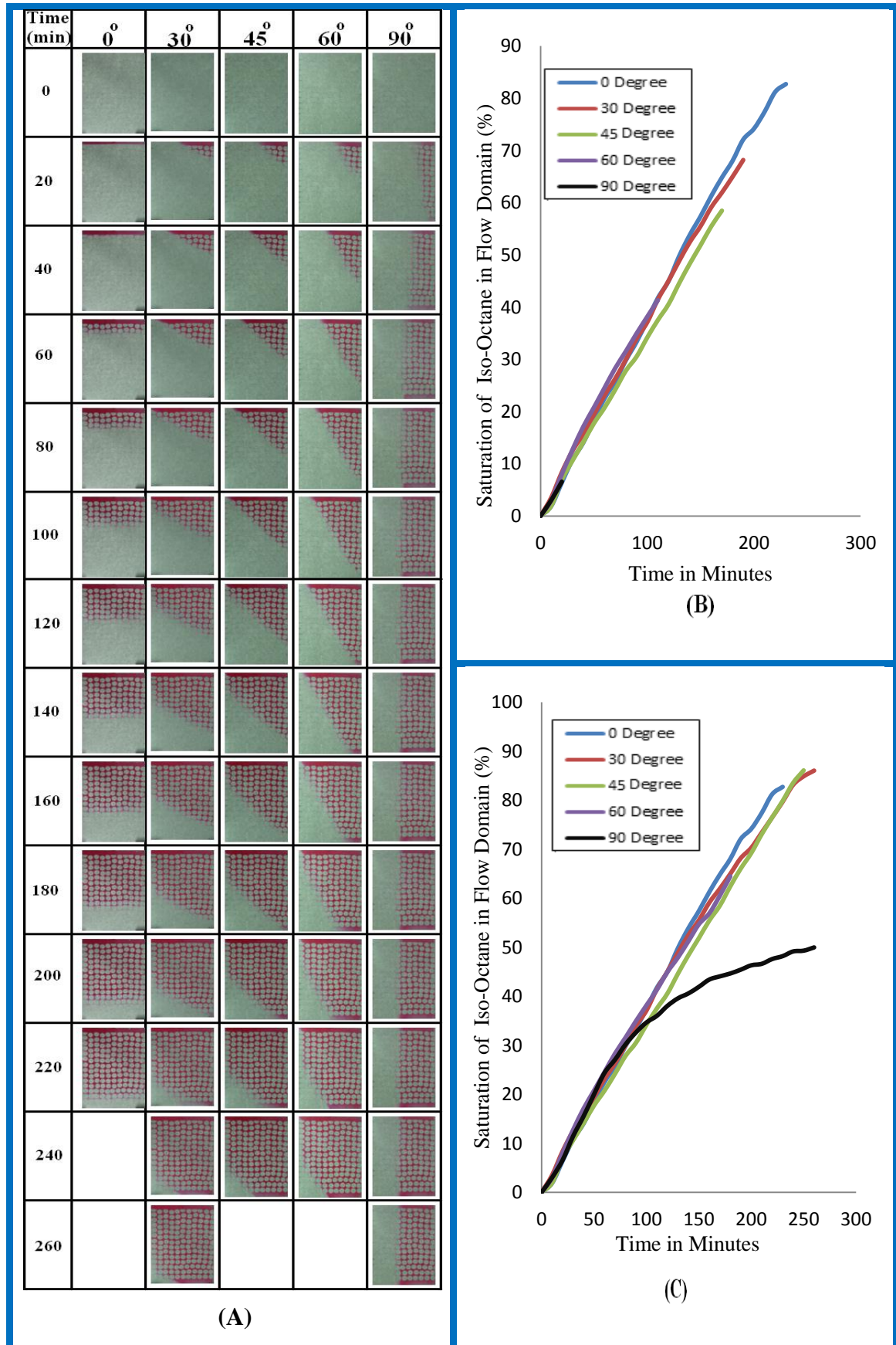
Figure 4-16: (A) Snapshots of the Experiments Conducted in the Second Micromodel at Injection Rate of 0.002 cm³/min (B) Pre-Breakthrough Profile (C) Pre- and Post-Breakthrough Profile

4.3.2 Experiments Representing Reservoir Flow Rates

Iso-octane was injected in the second micromodel at the constant flow rate of 0.002 cm^3/min. This represents a domain velocity of 2.8 x10^{-6} m/s (0.8 ft/day), which is found in reservoir rocks. The snapshots captured during the experiments are shown in Figure 4-17 (A), the saturation profile of different experiments until the breakthrough is shown in Figure 4-17 (B) and the pre- and post-breakthrough saturation profile is shown in Figure 4-17 (C). Figure 4-17 shows a delay in estimating the initial entry time of fluid in the micromodel. This can be noticed by observing in Figure 4-17 (B) and (C) that the injection fluid concentration in cases with higher tilt angle was not sensed until 30–40 minutes of operation. This is because the injection rate was quite low and the gravity effects were quite large, which sometimes gave the impression that the fluid had already entered the system. The misjudgement in the estimation of fluid entry time causes a delay in identifying the front in the system and gives an impression that the fluid has already entered the system.

Since the domain velocity is low compared to the previous cases, diffusion/dispersion effects become more important. These effects are prominent at the leading edge of the front where the injected fluid meets the inplace fluid. Thus, if the angular tilt is higher, the injected fluid tends to rise due to gravity segregation and the mixing effects can be witnessed at the top edge, which originates a finger. The result in Figure 4-17 (A) signifies that when the tilt angle increases from 0°, more mixing occurs at the leading edge which allows the fluids to spread, but in the direction of finger, which causes breakthrough due to mixing effect rather than velocity effect. Thus mixing might produce a negative effect if the tilt angle is higher. The misjudgement of fluid entry time explained in the above paragraph might be due to the fact that due to gravity effects, the lighter fluid tends to rise and molecular mixing occurs only at the top layer. However, due to the molecular level mixing, it was only visible at the latter stage.

Figure 4-17 (C) shows that the saturation profile of all cases did not overlap each other as in the cases with high fluid velocity. On the contrary, the graphs are separated from each other following a decline in the breakthrough saturation with increase in angular tilt. This might be due to the limitations of image processing as the hue value was selected between 0.2 and 0.6 as described in section 4.1.6, which does not take light pinkish colour into account. Therefore, as the angular tilt increased, more mixing

occurred at the top leading edge. However, this mixing effect was not captured during the image processing. It is also to be noted that since the injection rate is low compared to previous cases, the slight reduction in the diameter of the syringe at the upper end of the syringe did not disturb the flow rate. For this reason the abrupt change of saturation profile at the end of the experiment was not noticed.
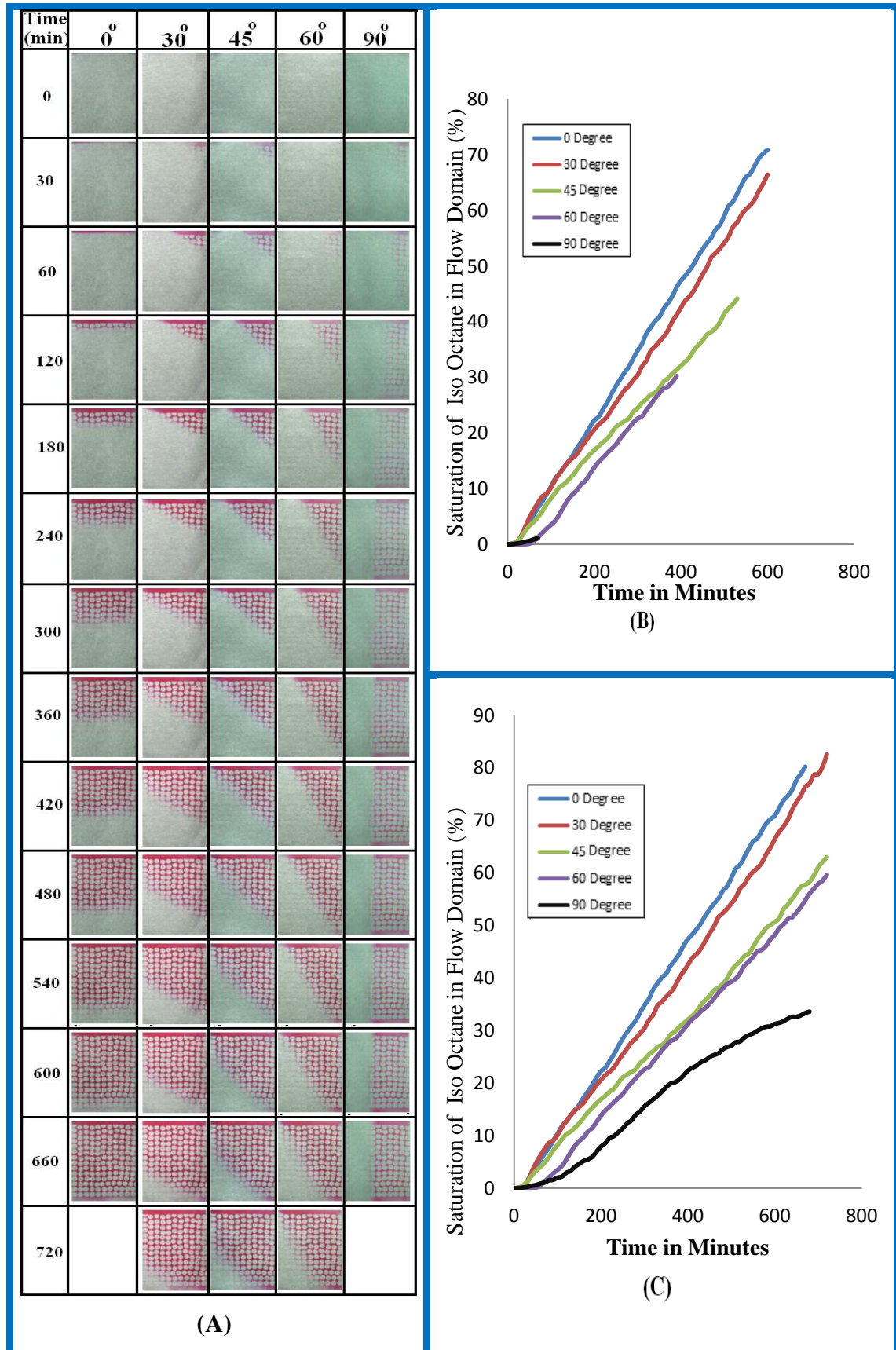
Figure 4-17: (A) Snapshots of the Experiments Conducted in the Second Micromodel at Injection Rate of 0.002 cm³/min (B) Pre-Breakthrough Profile (C) Pre- and Post-Breakthrough Profile

4.4 Experiment with Different Orientations

In all of the cases described in section 4.3, the angular tilt was observed to be the most sensitive parameter. Therefore, the cases described in this section were studied separately according to the tilt angle. Figure 4-18 to Figure 4-22 describe the comparison of all the cases at 0°, 30°, 45°, 60° and 90° respectively. The angles marked in the figures were measured manually and therefore might provide only a rough idea of front advancement.

4.4.1 0 Degree Cases

The comparison for cases at 0° in Figure 4-18 (A) shows that regardless of the injection velocity and the pattern, the front is fairly stable and the change in injection velocity hardly produces any impact on the front stability. The front propagates all the time at approximately 0°. Few signs of penetration were found in the first micromodel case, which might be due to a sudden increment of injection rate due to the changing diameter of the syringe. The saturation comparison of the cases until breakthrough is shown in Figure 4-18 (B), which shows that the saturation profile in pattern 1 and 2 at the flow rate of 0.005 cm^3/min and 0° inclination follows the same trend and produces similar values at breakthrough. The injection flow rate of 0.002 cm^3/min in the second pattern produces a slightly smaller value compared with the cases with 0.005 cm^3/min. However, the slight increment in the breakthrough saturation of the 0.005 cm^3/min case might be due to the limitation of image processing as the smaller concentration values of the concentration were not picked. Therefore, by comparing all of the cases of 0°, it was noticed that an increment in the injection rate produces little or no impact on the stability of the front.

4.4.2 30 Degree Cases

Figure 4-19 (A) shows that in both of the micromodels when the injection rate was 0.005 cm^3/min, the displacement front was started with an angle lower than 30°, and remaining between 23° and 27°, until it eventually reached a value equal or close to 30°. After this point, the inclination of the front started to decline and again reached a value of around 25°.

Figure 4-19 (A) shows that when the injection was performed at 30° in the second micromodel at the rate of 0.002 cm^3/min, the front was initiated with an angle of 30°. However, after some time the front readjusted itself to a similar value of around 25° as was experienced in the first two cases. This shows that at this angular tilt the combined effect of gravity and fluid mixing remains unaffected because of the injection velocity.

The saturation profile in Figure 4-19 (B) also shows that the saturation trend is similar for both of the models when the iso-octane was injected at the rate of 0.005 cm^3/min. The saturation profile of the second micromodel, which was flooded with iso-octane at the rate of 0.002 cm^3/min, shows a few fluctuations as the angle of the frontal advancement is also changing. However, when breakthrough occurs, the saturation of iso-octane in the flow domain shows a similar value to that of the 0.005 cm^3/min case because the inclination of the front at the breakthrough was found to be similar.

4.4.3   45 Degree Cases

The comparison in Figure 4-20 (A) shows that in both of the models when iso-octane was injected at 0.005 cm^3/min, the front inclination was started with an angle higher than 45 degrees (49°–50°). However, this inclination was gradually reduced, and this trend continued until the breakthrough occurred at the inclination between 34° and 37°. This was due to the fact that the flow rate was high and the fluids were not allowed to settle.

In contrast, the front inclination trend in the model when iso-octane was injected at 0.002 cm^3/min was different, as shown in Figure 4-20 (A). The front in this case started with an inclination close to 45° and then stayed at this angle throughout the experiment until the breakthrough occurred. This might have occurred because the gravity forces tended to favour the lighter iso-octane to override the heavier butanol and, since the flow rate was low, more mixing occurred at the top leading edge and kept the interface at the fixed angle. Figure 4-20 (B) also shows the agreement with the phenomenon described.

4.4.4   60 Degree Cases

The comparison in Figure 4-21 (A) shows that in both of the models when iso-octane was injected at 0.005 cm^3/min, the two characteristic inclination trends at the leading

and trailing edge of the front were observed. In the beginning, the leading edge of the front was started from a relatively small angular inclination, while the trailing edge stayed at the value close to 60°. This trend remained constant until the breakthrough occurred. The effect at the leading edge was because of the interplay between gravity and inertial force. When the tilt angle was higher, the fluid tended to override. However, the flow rate was higher too, which favours convection dominated inertial flow. The competition between these two forces resulted in a leading edge front of angle of less than 60°.

In contrast, when the injected flow rate was lower, the two characteristic angular inclinations appeared in the beginning of the experiment. These two inclination trends were then merged to a single inclination of 60° until the breakthrough occurred. This occurred because the fluids were adjusted due low flow rate and thus gravity forces dominated and the mixing occurred at the leading edge.

4.4.5 90 Degree Cases

The comparison in Figure 4-22 (A) shows that in the 90° case the gravity forces are dominating, which results the convection or dispersion of the injected fluid to happen in the top-most layer.

In the case when iso-octane was injected in the first micromodel at the rate of 0.005 cm^3/min, the iso-octane tended to invade the top-most pore spaces due to less density. The same trend was observed when iso-octane was injected in the second micromodel at this rate.

In the case when iso-octane was injected in the second micromodel with a rate of 0.002 cm^3/min, additional mixing was observed in the top edge due to the dispersion of fluids. Due to this dispersion and gravity forces, the iso-octane reached breakthrough at a very low saturation level, leaving approximately 99% of the volume uninvaded as shown in Figure 4-22 (B).

Figure 4-18: (A) Comparison of all Cases at 0° (B) Saturation Profile Comparison of all Cases at 0° until Breakthrough
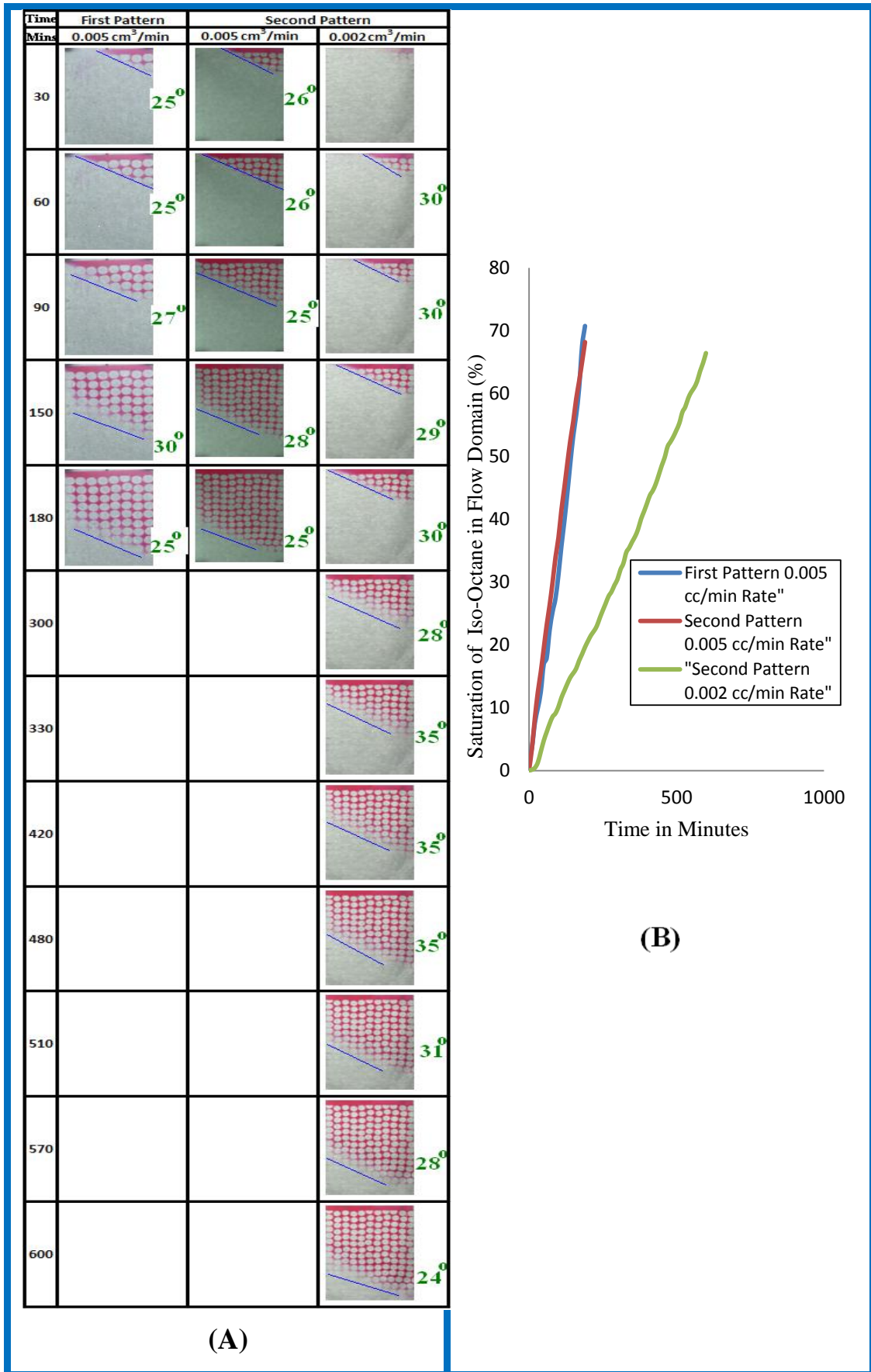
Figure 4-19: (A) Comparison of all Cases at 0° (B) Saturation Profile Comparison of all Cases at 30°
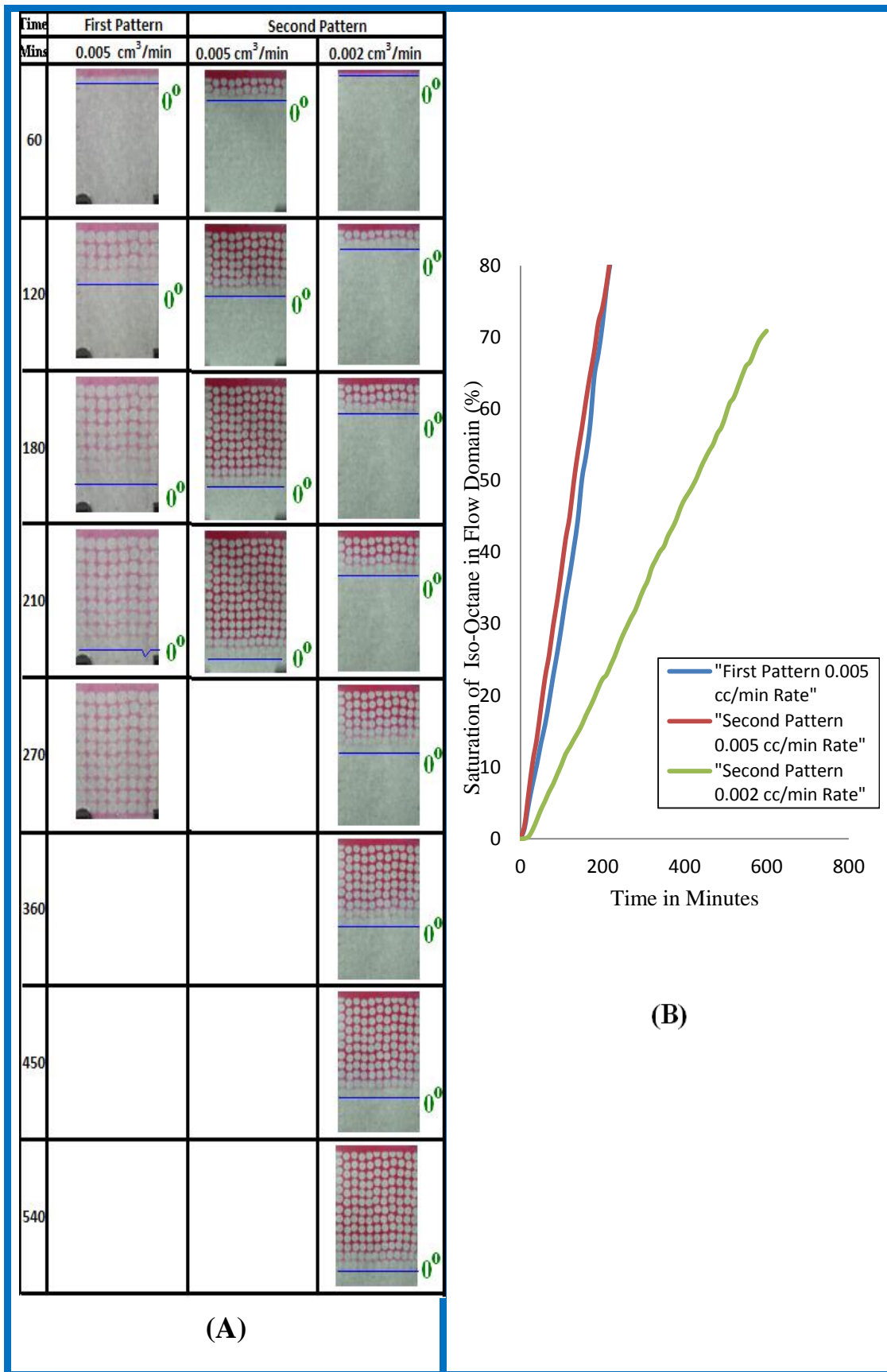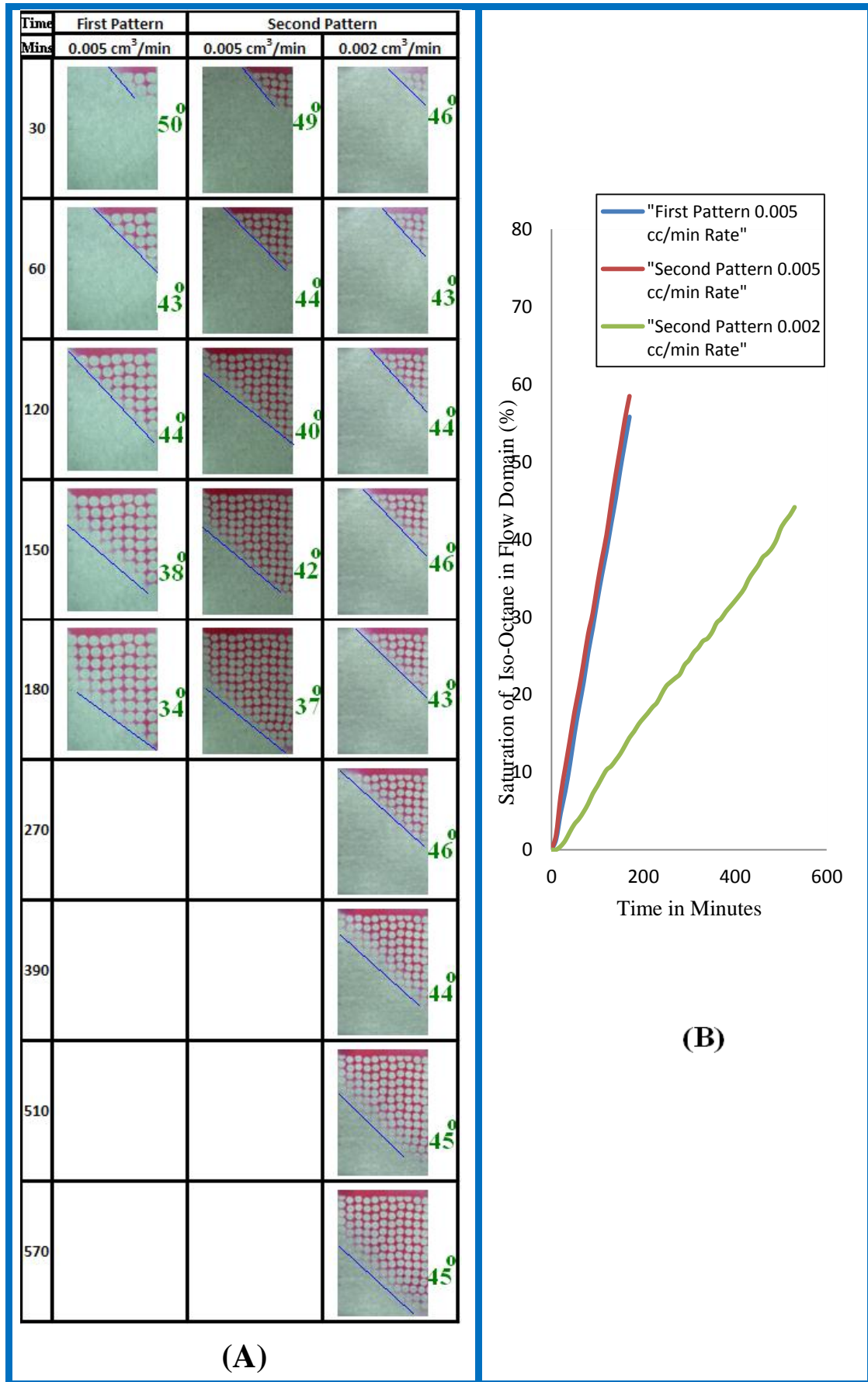
Figure 4-20: (A) Comparison of all Cases at 45° (B) Saturation Profile Comparison of all Cases at 45°
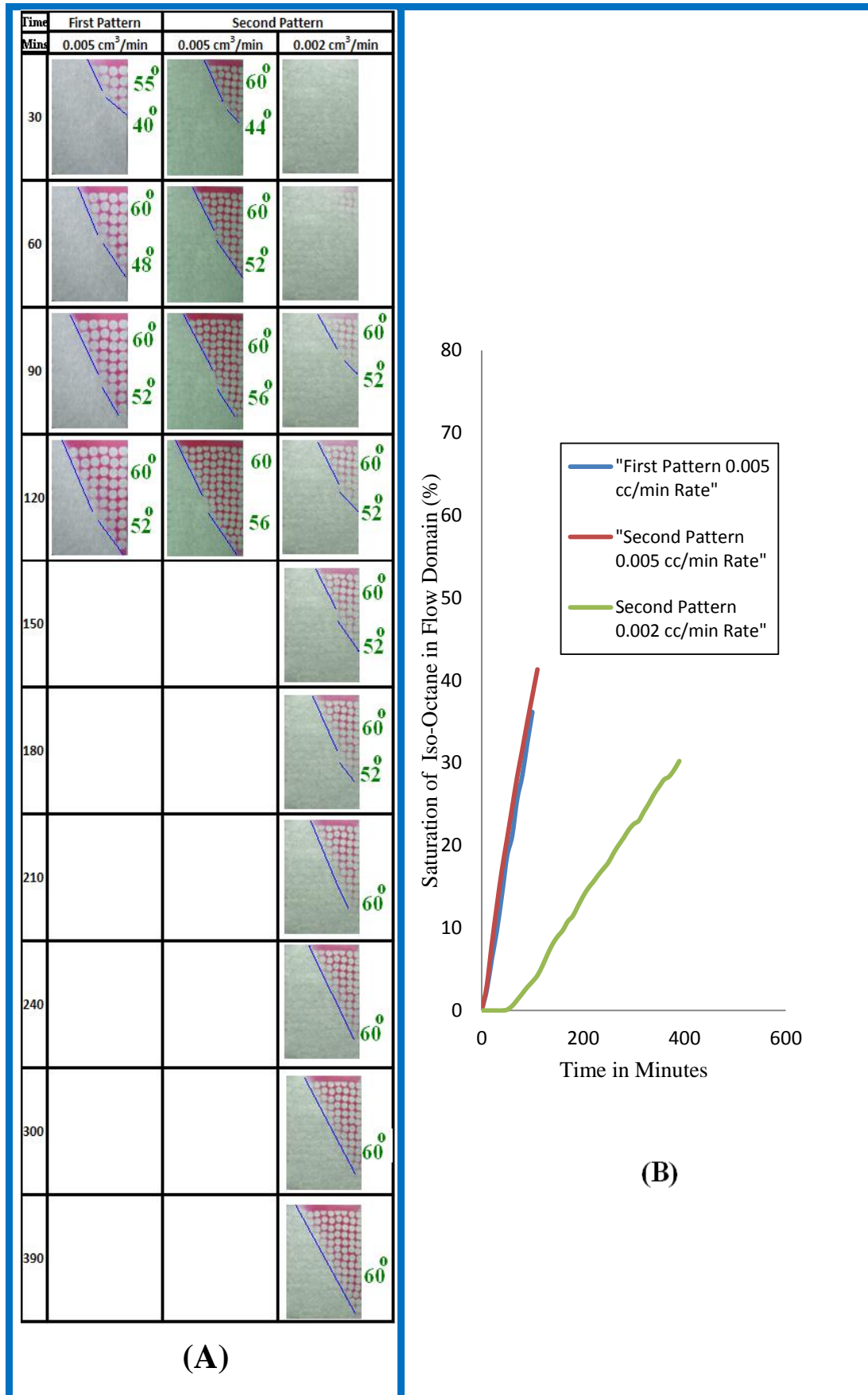
Figure 4-21: (A) Comparison of all Cases at 60° (B) Saturation Profile Comparison of all Cases at 60°
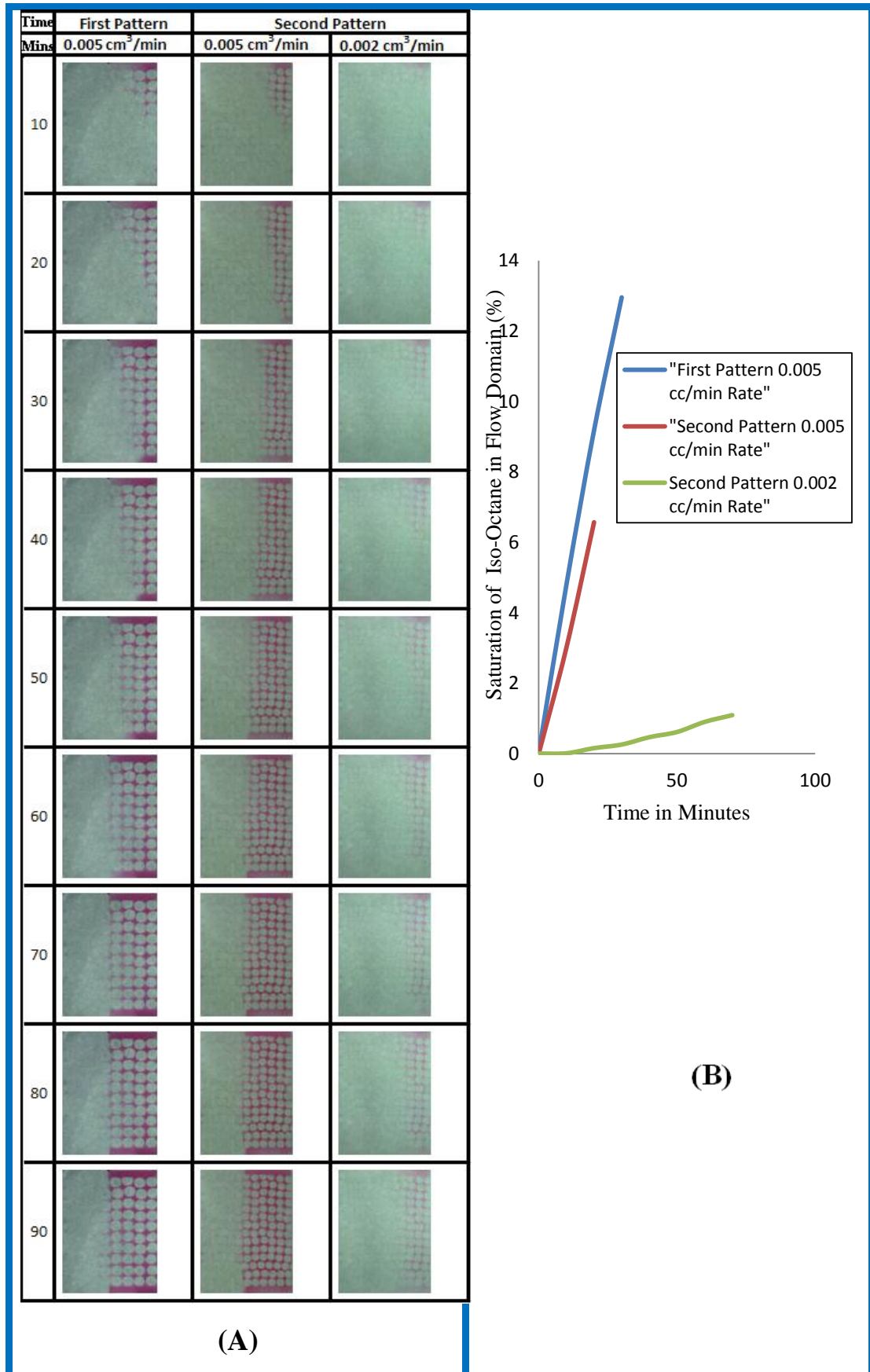
Figure 4-22: (A) Comparison of all Cases at 90° (B) Saturation Profile Comparison of all Cases at 90°

The results shown from Figure 4-18 to Figure 4-22 clarify that angular tilt and injection velocity are the most important parameters to be considered. The shape of the invading fluid largely depends on these two parameters. Only two velocities were considered in the experimental study as further reduction of the injection flow rate was not possible due to experimental limitations. More sensitivity studies were therefore required and were conducted during the simulation studies.

4.5 Error Analysis

Experimental studies always possess some operational challenges and uncertainties. In this section, some sources of errors have therefore been highlighted which should be taken into account when considering the results.

4.5.1 Sources of Error (Human)

- Camera adjustment: care was taken to capture only the flow domain; however, sometimes there was a little bend in camera adjustment so the captured flow domain was not straight and cropping of the image was needed to include this dead area. This area created some error in image processing.

- Error during mounting the glass model as it was based on local observation and not by some instrument. This caused a slight difference in the tilt angle adjustment.

- Misjudgement in estimating when the fluid arrived into the system, which affected the start time of the experiment.

- Although care was taken, dye concentration/strength might have varied from one experiment to another as sometimes the iso-octane dyed solution ran out and a new solution needed to be prepared. This affected the image processing of the final image.

4.5.2 Sources of Error (Instrument)

- Syringe pump precession to operate low flow rates.

- Leaks caused bubbles and restricted flow rates.

- Syringe diameter was big to operate low flow rates and a small diameter syringe was not possible due to the dead volume of the pipes to be filled.

- Syringe inner diameter towards the upper end was slightly less to ensure a good seal. However, this caused a slight disturbance in the flow rate, especially towards the end of the experiment as the flow rate might have increased due to the reduction of the syringe diameter.

- Some areas were not invaded by either the injected or in-place solvent as air blocked those channels. Figure 4-23 shows the case when the fluid was unable to invade the corners of the micromodel.
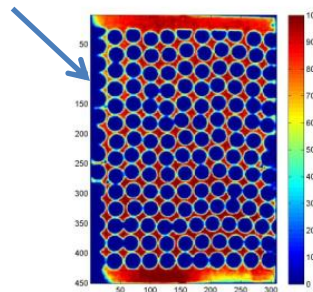
Figure 4-23: Volume Ignored due to Air Lock

- The movie created by the camera was in parts so it might have missed some small time fraction.

- The movie was originally captured in .Mts format which was converted to .Avi. The conversion might have reduced the quality of the picture, which may have affected the image processing.

- Error due to lighting at the back. Since the experiment ran for a long time, some parts of the movie were captured during the day and some parts during the night.

- Error due to capturing lower-quality picture from screen shots.

4.5.3 Sources of Error (Calculation and Estimation)

- Error due to image processing as the final image might not have been 100% saturated, but it was considered as it is fully invaded by the injection fluid.

- Images were cropped to select only the flow domain of the micromodel. However, sometimes the frame was not straight which resulted in bad cropping. Thus, in image processing, the small area was also considered. This was an error.

- The HSV range was considered to be between 0.2 and 0.6 in which most of the reddish was located. However, for the small concentration values in the porous domain when mixing occurred at the microscopic level (which especially occurred for the high-tilt angle cases), the lower values of reddish tint were ignored.

CHAPTER 5   FLOW SIMULATION

For modelling and flow simulation, COMSOL Multiphysics V4.2a was used, which is a finite element analysis simulation package that allows solving partial differential equations of a coupled system. Few studies were reported in the literature (Jha, John et al. 2006; Garmeh, Johns et al. 2007) which utilise COMSOL for modelling petroleum engineering related problems.

The geometry of flow patterns used in the experimental results comparison was the same as that adopted in the experimental work. Details of the geometry of patterns used in the experimental results comparison are described in the following section. In the sensitivity studies, a few more flow patterns were simulated along with the one that was used during the experimental results comparison. Details of these new flow patterns will be discussed in section 6.2.3 of Chapter 6.

5.1   Model Geometry used in Experiments Results Comparison

The porous geometry that was initially used in the experimental study was exported to COMSOL so that the geometric features and geometric scale of the original pattern remained unchanged. This allowed a direct comparison between the experimental and the simulation results at any time interval. The original MATLAB code used to generate the grains patterns was therefore modified to COMSOL-compatible format. A comparison of the porous geometry used in the experimental and simulation studies is shown in Figure 5-1.
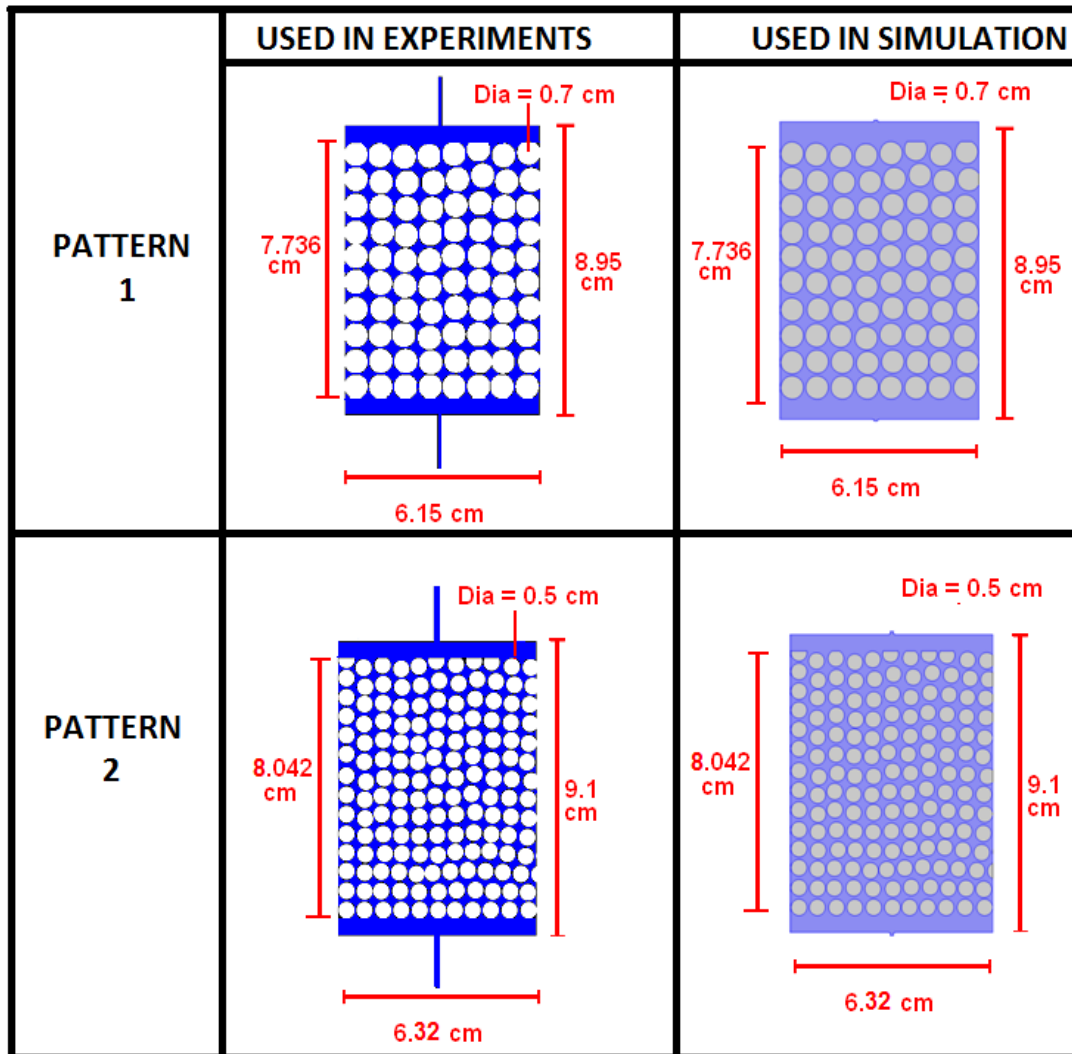
Figure 5-1: Porous Geometry used in Experimental and Simulation Studies

Figure 5-1 shows that the geometric dimensions of the porous domain used in the experimental and simulation studies were plotted exactly on the same scale. However, the inlet and outlet connections used in the experimental study were modified in the simulation studies. This was because the elongated inlet and outlet ports of the experimental patterns provided a path to the syringe; however, once the syringe was inserted, it did fit the gap. The remaining gap between the syringe and the walls was filled with the sealant as described in section 4.1.1.7. Therefore, the inlet and outlet connections of 0.1 cm x 0.1 cm were drawn manually in the simulation model and the edges were filleted with the radius of 0.05 cm to reduce the numerical dispersion. Figure 5-2 shows the inlet/outlet port geometry before and after the filleting of the edges.

(A)   (B)
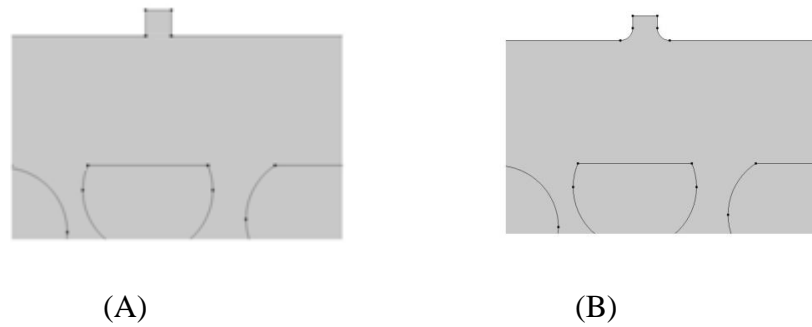
Figure 5-2: The Inlet port (A) without filleted edge and (B) with filleted edge

5.2 Mathematical Model

Flow simulation in COMSOL was performed throughout the flow domain. The injected fluid (solute) and the inplace fluid (solvent) were modelled as a single incompressible phase having a volume fraction C of injected fluid. Continuity and unsteady Navier–Stokes equations were used to calculate the velocity.

$$\nabla . v = 0$$

$$(5.1) \rho \frac{\partial v}{\partial t} - \mu \nabla^2 v + \rho(v. \nabla)v + \nabla P - \rho g \sin\theta = 0 \qquad (5.2)$$

Where:

ρ = Density

μ = Viscosity

P = Pressure

g = Gravitational Acceleration

$(\hat{\jmath}) = (\sin\theta, \cos\theta)$

The solution of equations 5.1 and 5.2 provide the pore velocities (v) at each node of the finite-element model. The simulations are at the pore scale, in that grain boundaries were explicitly modelled as no-slip boundaries (i.e. v=0). In addition, both of the side walls of the model were modelled as no-slip boundary (i.e. v =0). Both initial velocity and pressure in the porous domain were assumed to be zero i.e. $V_i=P_i=0$. The top inlet connection of 2 mm in length was added to simulate the effect of the syringe inlet connection that was used in the experiments. Injected fluid, with volume fraction C = 1, was continuously injected at a constant velocity from the inlet connection. The inlet

velocity calculation will be discussed in section 5.4.1. At the injection boundary there are no grains so that the mean pore velocity must increase within the pores as grains are encountered. Pore velocities can vary significantly over small distances depending on the size of the grains and pores. The pressure at the outlet is constant at atmospheric pressure. The gravity force was provided in the flow domain in terms of its x and y components as:

$$Fx = - \rho * g * \sin \theta \tag{5.3}$$

$$Fy = - \rho * g * \cos \theta \tag{5.4}$$

The density and viscosity of the fluid in the model was modelled as a linear function of concentration:

$$\rho = C * \rho_{injected} + (1-C) * \rho_{inplace} \tag{5.5}$$

$$\mu = C * \mu_{injected} + (1-C) * \mu_{inplace} \tag{5.6}$$

Where C is the concentration (or volume fraction) of the injected fluid (iso-octane). Once pore velocities were determined, the C was determined by solving the time-dependent convection-diffusion equation:

$$\rho \frac{\partial v}{\partial t} - \mu \nabla^2 v + \rho(v.\nabla)v + \nabla P - \rho g \sin \theta = 0$$

$$\tag{5.7}$$

Where D_o corresponds to the diffusion coefficient between the inplace and the injected fluid. The diffusion coefficient between butanol and iso-octane was calculated through a procedure that will be described in section 5.4.2 and was found to be 6.57 x 10^{-10} m^2/s. The boundary condition on all the grain boundaries and both the side walls was defined with no diffusive flux. The no-slip boundary condition in the fluid flow model ensured that no mass transport occurred through grains boundaries and through the side walls. At the outlet boundary, convection was assumed to be the dominating transport mechanism and diffusive transport was set to zero, that is:

$$D_o \nabla C = 0 \tag{5.8}$$

The initial concentration of injected fluid was assigned 0 mol/m^3, that is, the domain was completely filled with the inplace fluid. However, the concentration of injected

fluid at the inlet boundary was set to 1 mol/m^{3,} which represents the injection. The velocity (v) in equation 5.7 is obtained from the Navier–Stokes flow model. The flow and concentration models were solved simultaneously at each time step to yield the velocity and concentration of the fluids over time.

5.3 Meshing

In order to conduct simulation in the porous domain, the porous domain was discretised into smaller units of simple shapes known as 'mesh elements'. The defined model in the previous section was then introduced for each individual mesh element to obtain the system solution. Figure 5-3 shows the meshing of the porous domain into smaller shapes.
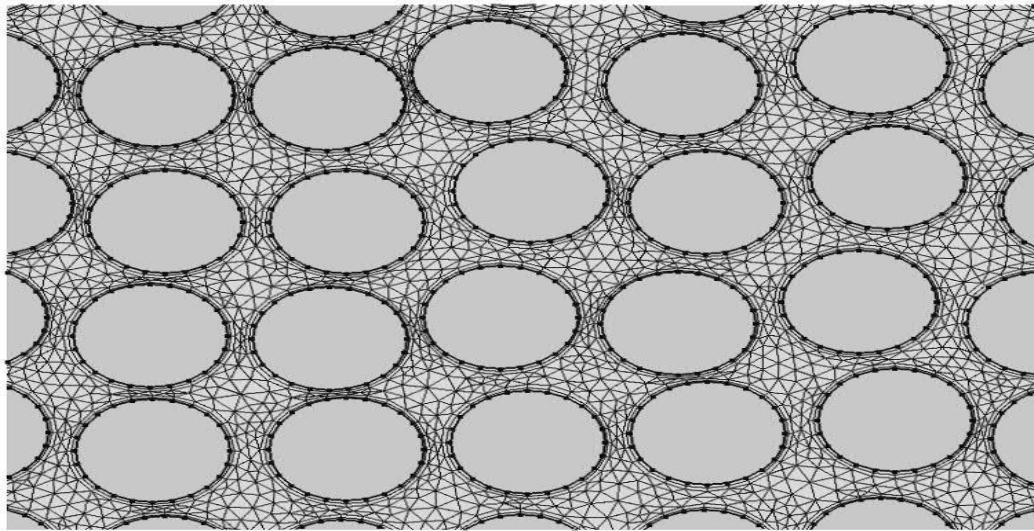
Figure 5-3: Meshing of the Porous Domain

The meshing in the porous domains was conducted automatically in COMSOL, which is calibrated for general physics. A total of 16827 (11117 triangular and 5710 quadrilateral) and 32866 (22762 triangular and 10104 quadrilateral) mesh elements were generated for patterns 1 and 2 respectively. The large number of mesh elements in the small area of the porous domain enhanced the accuracy of the simulation results. After the meshing of the domain, the time intervals and the step size were entered into the model, which depends on the nature of the simulation run. For example, the time interval defined during the experimental results comparison was the time required to complete an experiment for the particular case, and the frequency of the simulation

results output was adjusted so that it matched with the frequency of the snapshots captured during the experiments. The relative tolerance of 0.01 was adjusted through the simulation study, which controlled the internal time steps taken by the solver.

5.4 Model Parameters

5.4.1 Inlet Velocity

In the experimental study, the injected fluid was introduced in the system with a respective flow rate. However, in the defined numerical model, velocity was required to be supplied as an inlet boundary condition. The flow rate was required to be converted with respect to inlet velocity. Therefore, the injection flow rate from the syringe pump was divided by the inlet cross-sectional area of the micromodel to provide the inlet velocity.

$$Inlet\ Injection\ Velocity = \frac{Injection\ Flow\ Rate\ (from\ pump)}{Inlet\ Port\ Cross-Sectional\ Area} \tag{5.9}$$

The inlet cross-sectional areas for patterns 1 and 2 were calculated as 0.0048 cm^2 and 0.0044 cm^2 respectively in section 4.2.1.4. The inlet velocities used in the experimental results matching is given in Table 5-1

Table 5-1: Inlet Velocities Provided in Simulation during Experimental Results Matching

Micromodel Pattern Number	Injection Flow Rate (cm^3/min)	Inlet Cross-Sectional Area (cm^2)	Inlet Velocity (cm/min)	Inlet Velocity (m/sec)
1	5 x10^{-3}	4.8 x10^{-3}	1.04	1.73 x10^{-4}
2	5 x10^{-3}	4.4 x10^{-3}	1.13	1.89 x10^{-4}
2	2 x10^{-3}	4.4 x10^{-3}	0.45	7.55 x10^{-5}

The relation in equation 5.9 can also be written in terms of domain velocity, and the effective width depth of the micromodel as:

$$Inlet\ Velocity = \frac{Grain\ Domain\ Velocity\ x\ Effective\ Width\ \ x\ \ Depth\ of\ Micromodel}{Inlet\ Port\ Cross-Sectional\ Area} \qquad (5.10)$$

The description of depth and the effective width and domain velocity can be found in sections 4.2.1 and 4.2.2. The equation 5.9 can be used in situations when the injection flow rate is known (such as in the experiment comparison study), while the equation 5.10 can be used in situations when a case is required to be simulated with variable domain velocity (such as in the sensitivity studies).

5.4.2 Diffusion Coefficient

The diffusion coefficient or diffusivity, D_o is the rate of mass transport of solute (injected fluid) in solvent (inplace fluid) across the unit area. It is the measure of how quick one substance diffuses into other.

The diffusion coefficient between iso-octane and butanol could be determined through the Wilke and Chang (1955) correlation given below:

$$D_{AB} = \frac{7.4\ x10^{-8}\ x\ (\varphi\ x\ M_B)^{0.5} x\ T}{\mu\ x\ V_A{}^{0.6}} \qquad (5.11)$$

Where,

D_{AB} =   Diffusion coefficient of solute (iso-octane) in solvent (butanol)

M_B =   Molecular weight of solvent (butanol) i.e. 74.12

φ =   Association factor of solvent (butanol) i.e. 5.1 (Lusis and Ratcliff 1971)

T =   Absolute temperature i.e. 298 K

μ =   Viscosity of solvent (butanol) i.e. 3 cP

V_A =   Molar Volume of solute (iso-octane) in cm^3/mol

The respective values of all of the variables (except molar volume) are listed above. The molar volume of iso-octane could be determined by the Rackett (1970) correlation, the Tyne and Calus (1975) correlation and using the basic definition of the molar

volume. Molar volume was therefore calculated through all of these techniques and averaged to get a reasonable estimate.

5.4.2.1 Using Rackett (1970) correlation

$$(Molar\ Volume)_{Rackett} =$$
$$Critical\ Volume * Compressibility\ Factor^{\ (1-Reduced\ Temperature)^{0.2857}} \qquad (5.12)$$

$$(Molar\ Volume)_{Rackett} = 468 * 0.266^{\ (1-0.5478)^{0.2857}} = 162\ cm^3/mol$$

5.4.2.2 Using Tyne and Calus (1975) correlation

$$(Molar\ Volume)_{Tyne/Calus} = 0.285 * (Critical\ Volume)^{1.048} \qquad (5.13)$$

$$(Molar\ Volume)_{Tyne/Calus} = 0.285 * (468)^{1.048} = 179.16\ cm^3/mol$$

5.4.2.3 Using Basic Definition of Molar Volume

$$(Molar\ Volume)_{Definition} = \frac{Molar\ Mass\ in\ g/mol}{Density\ in\ g/cm^3} \qquad (5.14)$$

$$(Molar\ Volume)_{Definition} = \frac{114}{0.688} = 166.03\ cm^3/mol$$

Therefore,

Average molar volume = 169.35 cm^3/mol

Substituting values of all variables in the equation 5.11 gives:

Diffusion Coefficient between Iso-octane and butanol = 6.57375 x 10^{-10} m^2/s

5.5 Experimental and Simulation Results Comparison

The mathematical model described in section 5.2 was required to be verified before further sensitivity studies could be performed. A study was therefore conducted to simulate the experiments described in section 4.3. The comparison between the results can be used to authenticate the simulation model. It is to be noted that this comparison

cannot be treated as normal history matching to tune parameters because most sensitive parameters are known in micromodel e.g. permeability is not required as the actual geometry is being solved.

In this study, the experimental and simulation results were compared based on the concentration of iso-octane (injected fluid) in the porous domain and instead of effluent concentration. This concentration was compared using two different approaches:

(a) Qualitative comparison and

(b) Quantitative comparison.

5.5.1   Qualitative Comparison

Qualitative comparison refers to the photographical comparison of the experiment and simulation injection front advancement in the porous domain at the same time steps. In order to perform this comparison, images were captured during the experimental study and the respective time was recorded. The captured images were processed and the concentration profile was assigned as described in section 4.1.6.

The same experiments were simulated in COMSOL using the model described in section 5.2. Snapshots were captured from the corresponding simulation case at the same time as the image was captured during the experimental study. A comparison of frontal advancement of injection fluid was made between the simulated and the experimental processed images at the same time step. This provided a direct comparison between the simulation and the experimental results throughout the process rather than only relying on matching the breakthrough concentration.

5.5.1.1   Qualitative Comparison of Cases in the First Pattern

The experiments conducted on the first micromodel pattern were discussed in section 4.3.1.1. Since the iso-octane was introduced in the micromodel at the rate of 0.005 cm^3/min, the respective inlet velocity of 1.73 x 10^{-4} m/s was provided as the inlet boundary condition as calculated in section 5.4.1. In addition, the tilt angle was provided to compare the respective cases. The qualitative comparison between the experimental and simulation results of the first pattern cases are shown in Figure 5-4.
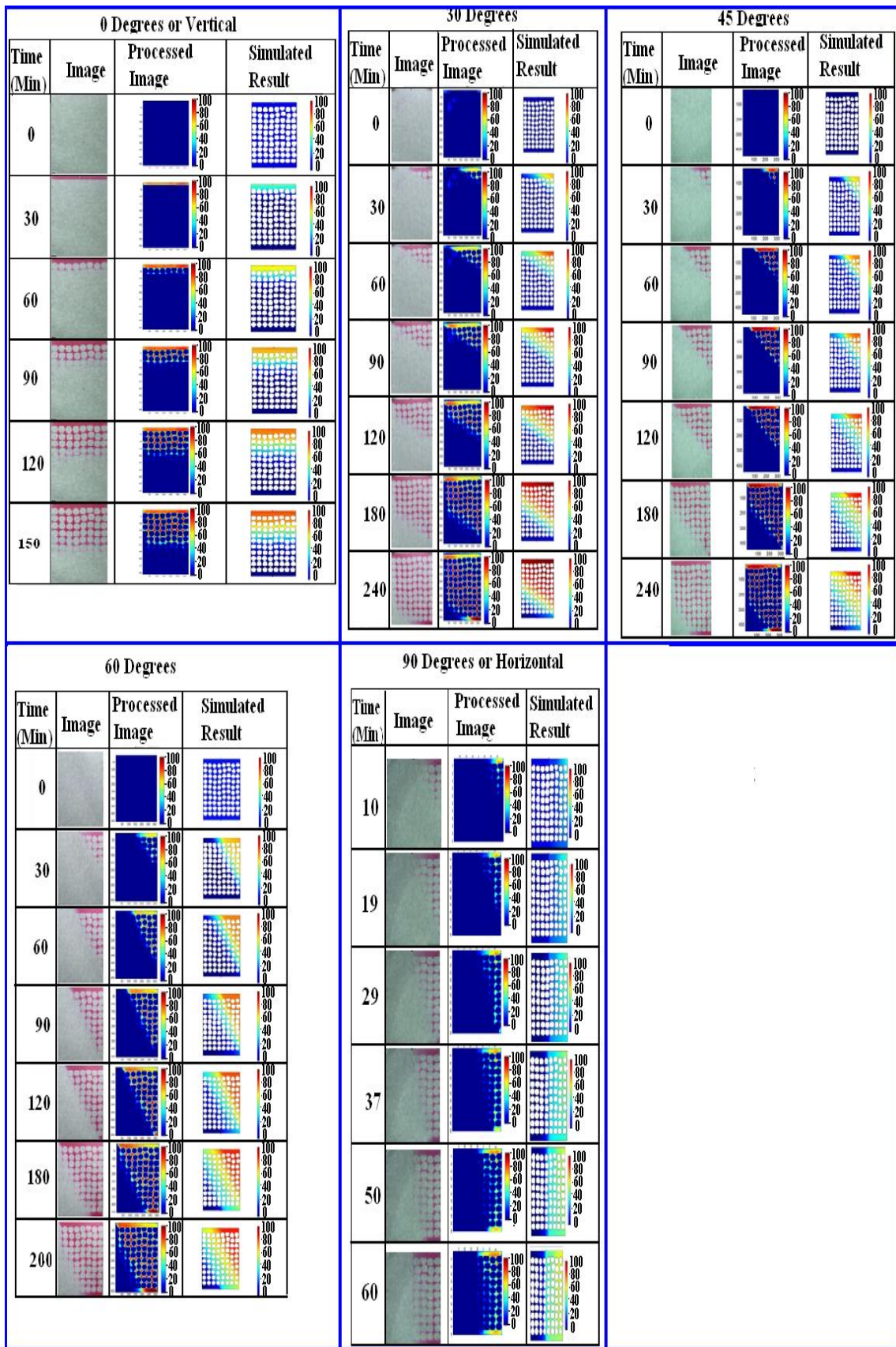
Figure 5-4: Qualitative experimental and simulation comparison for the first pattern

The qualitative comparison between the experimental and simulation results for the first pattern demonstrates that the trend of front propagation is similar in both simulation and experiment. However, towards the end of the experiments, the front propagates slightly faster, which is due to the limitation of the glass syringe used for injection purposes as discussed in section 4.3.1.1. The inner diameter of the glass syringe slightly reduced at the upper end of the syringe in order to have a good seal, and as a result the injection rate was disturbed a little.

5.5.1.2 Qualitative Comparison of Cases in the Second Pattern

The experiments conducted on the second micromodel pattern were discussed in sections 4.3.1.2 and 4.3.2. The experiments on the second pattern were conducted at different dipping angles with injection flow rates of 0.005 cm^3/min and 0.002 cm^3/min. The corresponding inlet velocities were calculated as 1.89 x 10^{-4} m/s and 7.55 x 10^{-5} m/s in section 5.4.1.

5.5.1.2.1 Injection at the Rate of 0.005 cm³/min

Figure 5-5 shows the qualitative comparison between the experimental and simulation cases when injection was carried out at the rate of 0.005 cm^3/min in the second pattern at various dipping angles. Figure 5-5 shows the similar behaviour of experiment and simulation front propagation at the same time steps. Besides a little separation towards the end of the experiment, the overall match found good. The late time mismatch is for the same reason as described in section 4.3.1.2. The experiment and simulation results show that the breakthrough in the vertical case occurred at a larger time compared to other cases due to the favourable gravitational force. However, when the micromodel was tilted, the breakthrough occurred earlier than in the vertical case. Furthermore, the percentage of unswept butanol at the breakthrough increased when the tilt angle was increased.

Figure 5-5: Qualitative experimental and simulation matching for the second pattern at 0.005 cm^3/min injection rate

5.5.1.2.2 Injection at the Rate of 0.002 cm³/min

The qualitative comparison between the experimental and simulation cases of 0.002 cm^3/min is shown in Figure 5-6. This Figure shows that the experimental front followed the same trend as the simulation, although with a short delay. This delay in front advancement was due to the false estimation of injected fluid in the porous domain during the experimental study as reported in section 4.3.2. Besides this delay, the trend in experiment and simulation was very similar.

In addition, since the injection flow rate was small enough, the slight change in the diameter in the upper end of the syringe did not produce any significant increment in the front velocity as was seen in the cases with 0.005 cm^3/min. Hence the simulation and experiment front propagate with the same trend.
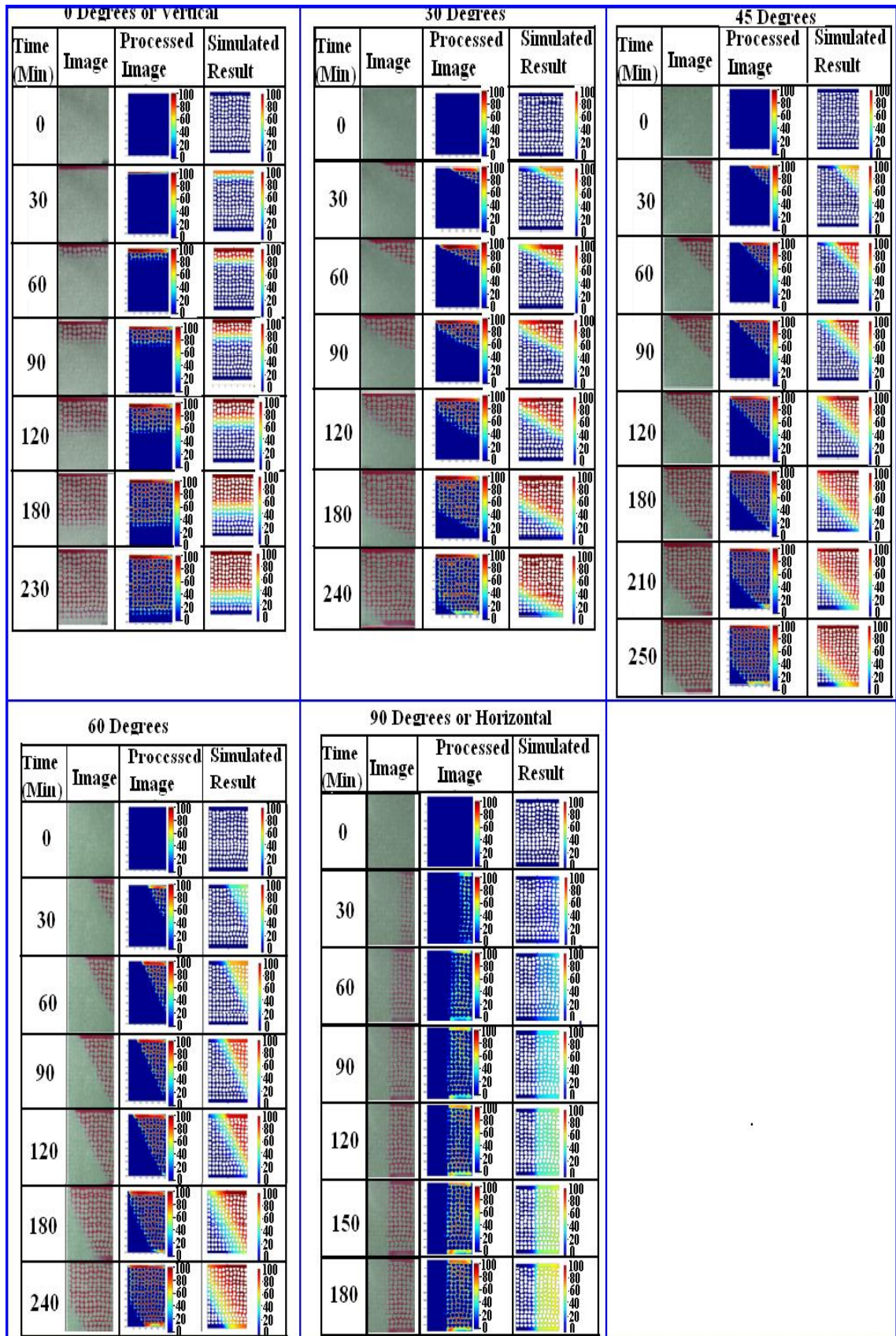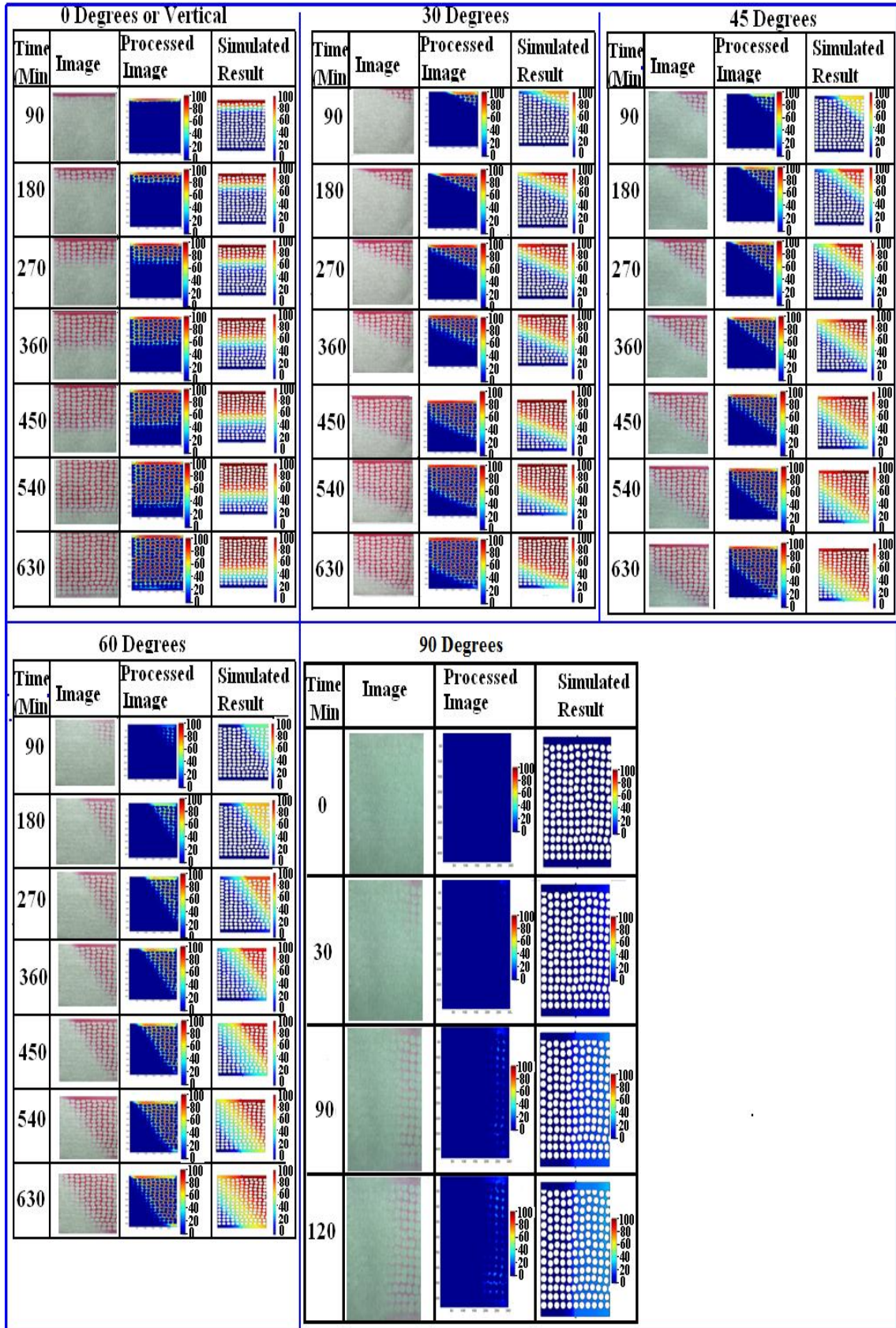
Figure 5-6: Qualitative experimental and simulation matching for the second pattern at 0.002 cm^3/min injection rate

5.5.2 Quantitative Comparison

Quantitative comparison refers to a graphical comparison between experimentally processed injected fluid concentration and the values of injected fluid concentration obtained during simulation. This comparison might have some limitations due to the image processing approximations of the experimentally obtained images. However, it can provide a rough assessment to evaluate the contrast between the experiment and the simulation. In addition, like qualitative analysis, this comparison was also based on the concentration of the injected fluid in the micromodel rather than on comparing the effluent concentration. Therefore, concentration values observed during the experiment and the simulation were compared at the same time steps.

The concentration of the injected fluid in the experiments was calculated through image processing. However, this image processing provides an estimated value which might have some operational error(s) discussed in section 4.5. Therefore, qualitative matching could be preferred over quantitative matching because the trend of front advancement was used as a comparison rather than relying on estimated values.

The concentration of the injected fluid in the simulation was obtained in COMSOL through the surface integration of concentration of the iso-octane throughout the flow domain. This provides the average concentration of iso-octane at different time intervals.

5.5.2.1 Quantitative Comparison of Cases in the First Pattern

The quantitative matching between the experimental and the simulation results for the first pattern is shown in Figure 5-7. The simulated and experimental saturation of injected fluid in the domain is plotted against the elapsed time.

For the 0° case, the first 150 minutes matching between experiment and simulation concentration values seems very close. However, after 150 minutes the experimental profile tends to accelerate, which might have occurred due to the slight reduction in the diameter of the syringe. Similar behaviour is observed in the 30° case, for the saturation front remains similar until 150 minutes and then separation occurs.

The comparison of the 45° case shows that initially the simulation front starts with a slightly higher saturation value. However, after 100 minutes both the simulation and experimental values become the same and then, from this point, the experimental values supersede the simulation front. Regardless of this inter-crossing, the saturation values in both the simulation and the experiments remain similar until 150 minutes of operation. The further separation after 150 minutes of operation might be due to the slight reduction in the syringe diameter.

The comparison of the 60° and 90° cases shows that the iso-octane saturation value in the experiments and simulation remains the same for approximately 100 minutes and then the experimental and simulation curve trend separated. This separation might be due to the early breakthrough in the higher-dipping angle cases. The effect of syringe radius can also be counted in this trend separation.

For all of the tilt angles, the trend in both the simulation and the experiments was found to be similar, especially for the early time. The late-time profiles mismatch occurred as the experimental front propagates slightly fast towards the end of experiment due to the limitation of the glass syringe used for injection purposes. In addition, exact-values matching was not possible due to the known constraints of image processing.
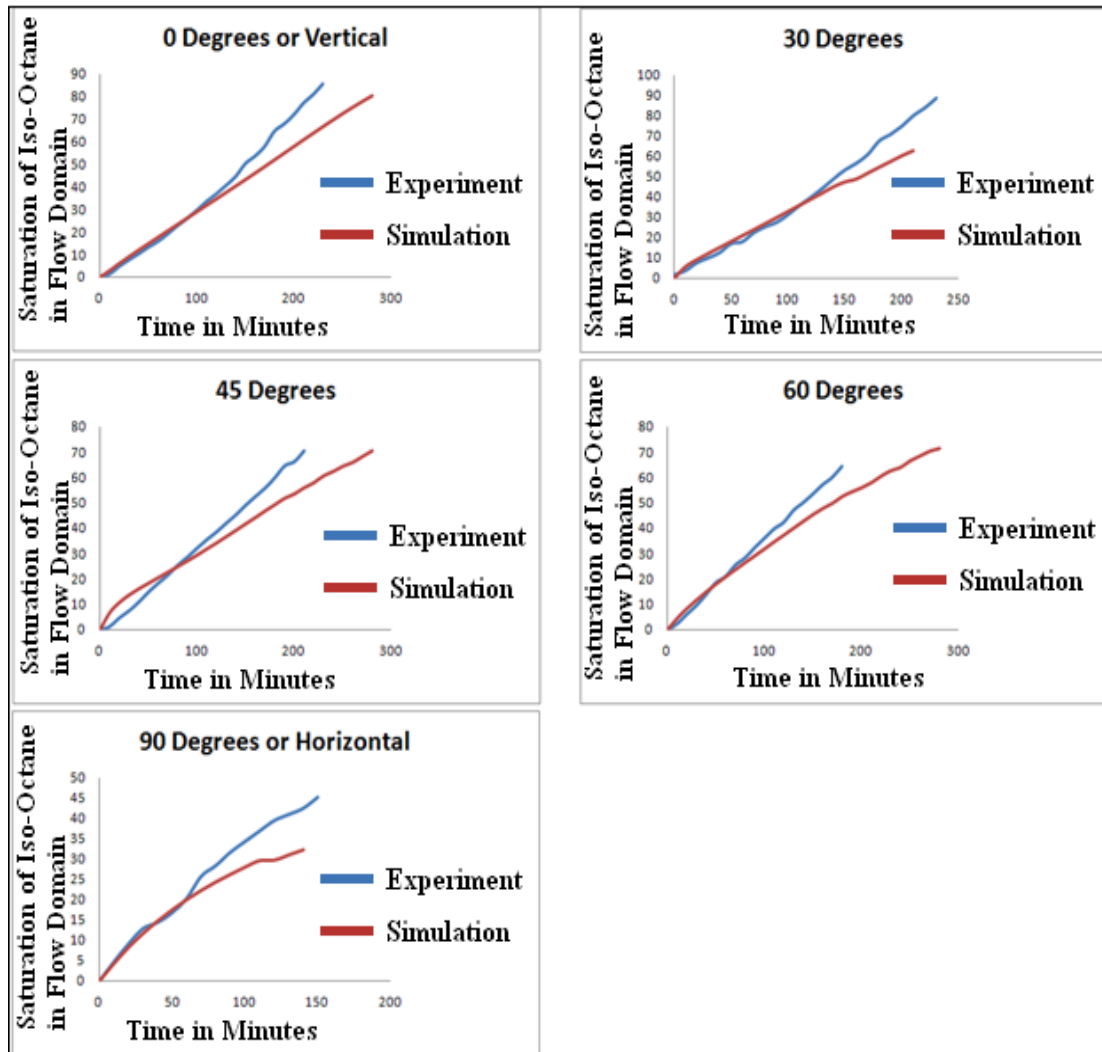
Figure 5-7: Quantitative experimental and simulation matching for the first pattern (flow rate 0.005 cm^3/min)

5.5.2.2 Quantitative Comparison of Cases in the Second Pattern

5.5.2.2.1 Injection at the Rate of 0.005 cm³/min

The quantitative matching of the experimental and simulation results for the second pattern when injection was carried out at the rate of 0.005 cm^3/min is shown in Figure 5-8. This Figure shows that for the cases with less angular dip, the saturation profile for the experiment and simulation is very similar especially for the initial operation. A little separation was found in the late time which might be due to the syringe effect.

For the cases with high angular dip (i.e. 60° and 90°), the separation between the simulation and experimental curves is prominent. This might be due to the fact that the breakthrough of iso-octane in these cases occurs quite early compared with the cases

with less angular dip. Once the breakthrough occurs, iso-octane flows more easily in the experimental cases, which results in higher saturation in the micromodel.
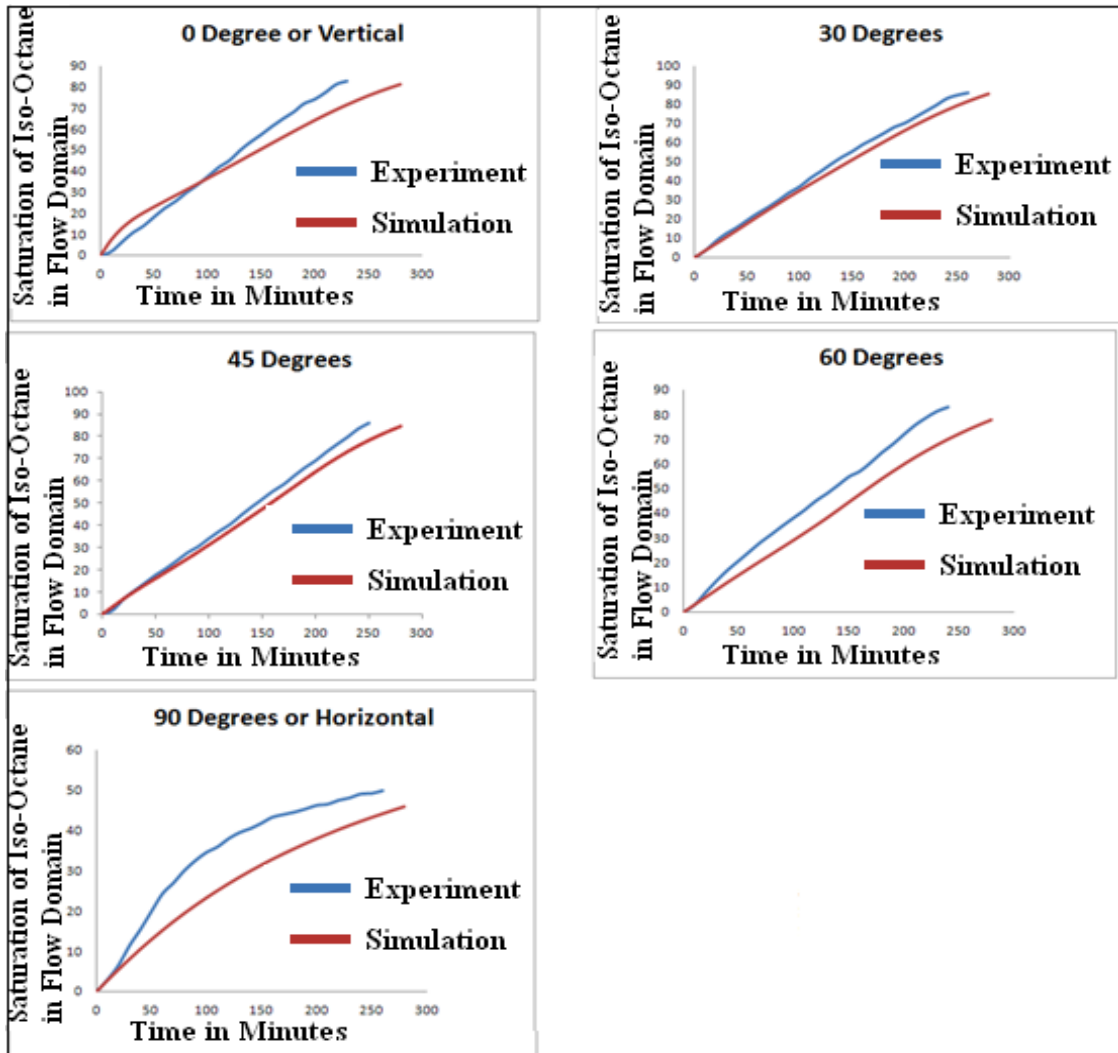
Figure 5-8: Quantitative experimental and simulation matching for the second pattern (flow rate 0.005 cm^3/min)

5.5.2.2.2 Injection at the Rate of 0.002 cm³/min

The quantitative matching of the experimental and simulation results for the second pattern when injection was carried out at the rate of 0.002 cm^3/min is shown in Figure 5-9. This Figure shows that in this case, the experimental values are lower compared to the simulation results, especially in the cases with higher tilt angle. This could be due to the fact that the domain velocity is lower, which promotes dispersion/diffusion-mixing of the fluids in the porous media. Also, the angular tilt is high, which promotes the lighter fluid to override. Since mixing occurs at the microscopic level, the visual change

cannot be estimated with the naked eye. Also, the concentration of the injected fluid at the leading edge could be too low as it could not be captured in the image processing as described in section 4.5.3. This caused the injection fluid concentration to drop. Due to this reason the injection concentration in the higher tilt angle was not deducted in the image processing until some significant volume of the inplace fluid was displaced by the injected fluid.

Figure 5-9 also shows that no sudden increment in the concentration was observed in the experimental concentration profile. This was because the flow rate was small enough to be less sensitive to the slight change of the syringe diameter. This effect was also discussed in section 4.3.2.

Figure 5-9 shows that for the 0° and 30° cases, the simulation and experiment concentration curves were in reasonably good agreement. For the cases with a tilt angle higher than 45°, the trend of simulation and experimental curves was found to be similar. However, the exact values were not matched, which could be due to the limitation of image processing.
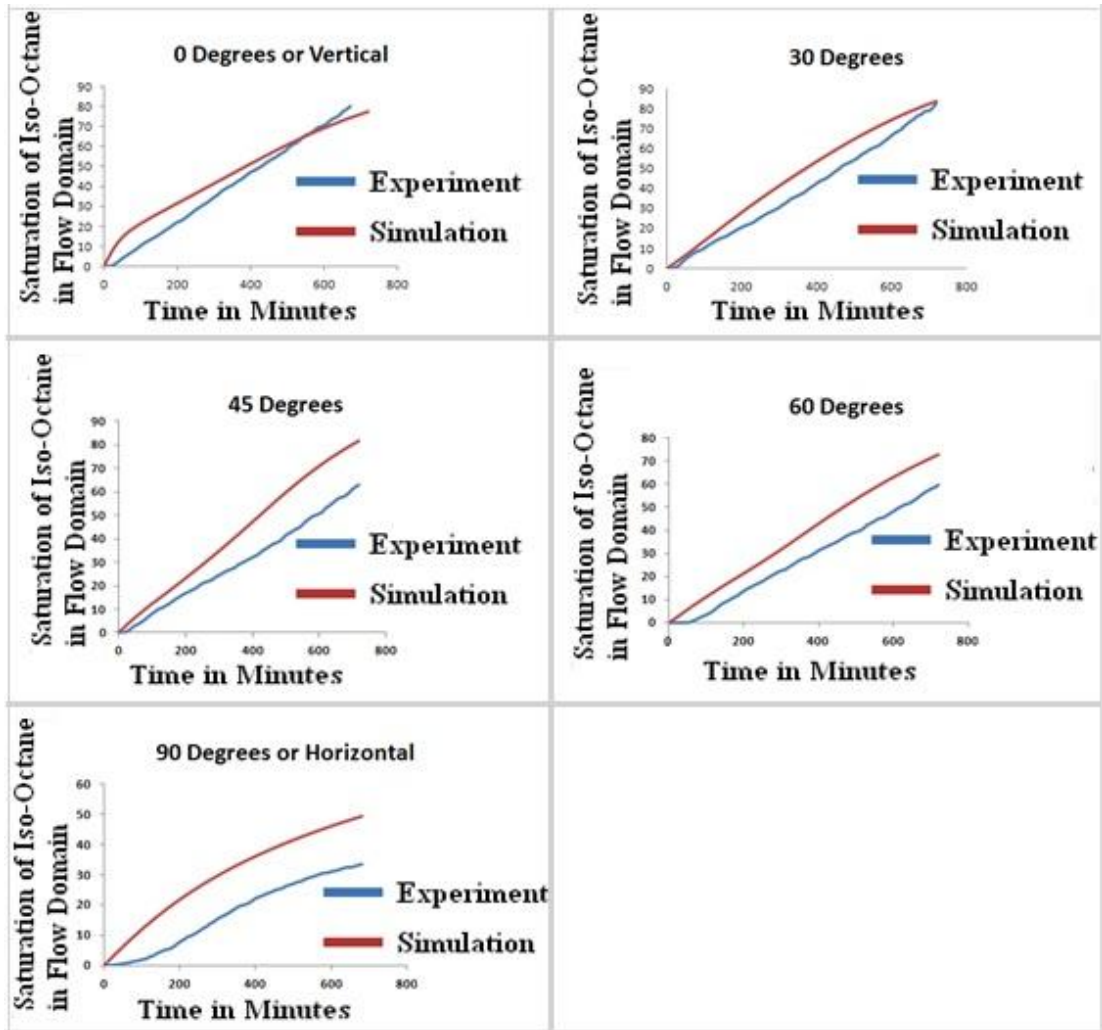
Figure 5-9: Quantitative experimental and simulation matching for the second pattern (flow rate 0.002 cm^3/min)

The micromodels had some depth of cut to allow fluid flows. Although this depth was quite small, it represented a 3-D system. However, the simulation studies assume a 2-D system, which might result in some variations. Nevertheless, a few exceptions due to the image processing errors and/or numerical disturbance are also present.

Taking all of these assumptions into consideration, the overall comparison of experiments and simulation through qualitative and quantitative approach shows similar behaviour. This validates the assigned physics and the boundary conditions used. This similar behaviour might be due to the fact that exact geometry of porous material was used in the simulation and experimental work. Furthermore, more exact physics was assigned in the porous media rather than on relaying on the pipe-flow equations. Therefore, the applied physics was used in further sensitivity analysis.

CHAPTER 6   SIMULATION STUDIES

This Chapter mainly discusses the simulation studies carried out using the numerical model defined in Chapter 5. These studies can be divided into two parts:

1- Comparison with previous work

2- Sensitivity studies

6.1   Comparison with a Previous Work

An existing numerical simulation study conducted in past by Stevenson et al.(2004) was re-simulated with the present methodology and the results were compared. The aim of performing this study was to compare the results between the old and the new methodology, to explore the research gaps further and to perform sensitivity studies to fill those gaps.

6.1.1   The Work of Stevenson et al.

Stevenson et al. (2004) conducted a miscible displacement study for top- and bottom-injection scenarios using a pore-network model. Pipe flow Poiseuille's equation was used to calculate the pressure drop. Diffusion and mixing of fluids were not accounted for in this work, and the front propagation was determined through a defined quantity 'interfacial width'. The breakthrough saturation of the injected fluid was plotted against a dimensionless Darcy–Rayleigh Number, G, for different mobility ratios. The Darcy–Rayleigh Number was defined as:

$$G = \frac{\Delta\rho \, g \, k}{\mu_{\text{inplace}} v}$$

Where

$\Delta\rho$ = density difference between the inplace and the injected fluid,

g   = acceleration due to gravity,

k = permeability,

$\mu_{inplace}$ = inplace fluid viscosity

v = velocity of the injected fluid in the porous domain.

G was considered positive for top injection and negative for bottom injection. Three different mobility ratios (0.1, 0.33 and 1.0) were considered. The definition adopted for the mobility ratio (M) was reversed from the normal convention, that is:

$$M_{Stevenson} = \frac{\mu_{injected}}{\mu_{inplace}}$$

This definition is the reciprocal of the definition adopted in the present research, that is:

$$M = \frac{\mu_{inplace}}{\mu_{injected}}$$

Therefore, the mobility ratios of Stevenson et al. (2004) were treated as 1, 3 and 10 in the research study. The breakthrough saturation of the process was treated as the proxy displacement efficiency. The breakthrough saturation refers to the injected fluid concentration in the domain. The results of Stevenson et al.'s (2004) work have been illustrated in Figure 6-1. The values quoted in Figure 6-1 for the mobility ratios are the converted values as per the definition adopted in the present research.

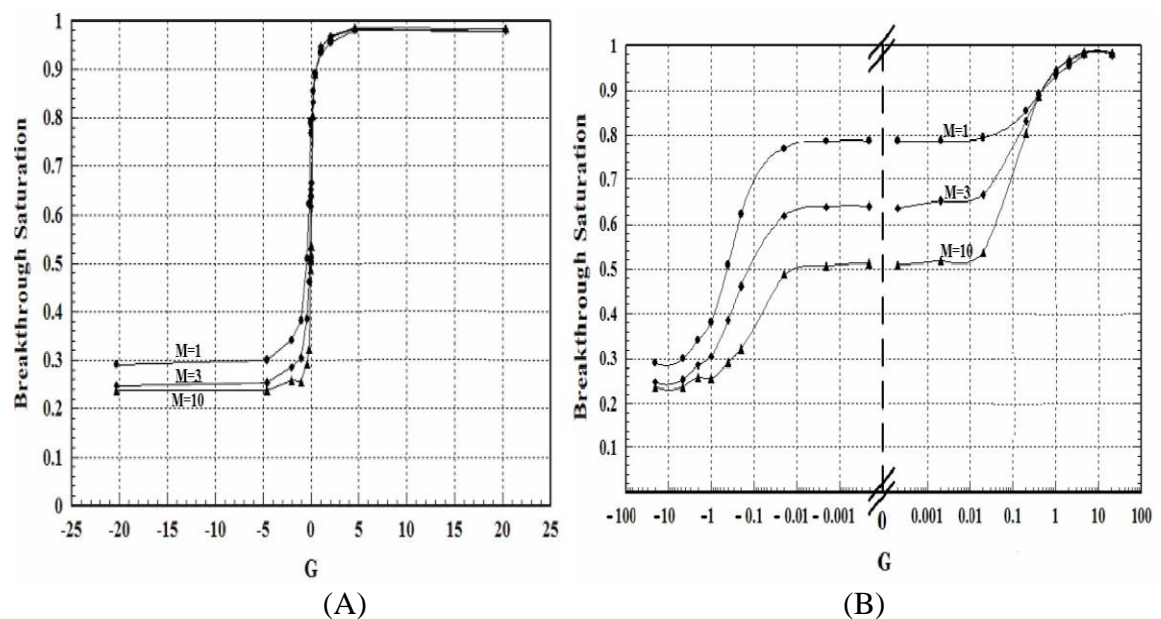Figure 6-1: Graph of Breakthrough Saturation versus Darcy–Rayleigh Number (G)

Figure 6-1 (A) and Figure 6-1 (B) are the Cartesian and semi-log plots between the Darcy–Rayleigh number, G, and the breakthrough saturation S_b respectively. The semi-log graph was plotted to highlight the sensitivity of the mobility ratio in the smaller range of G. The positive and negative values correspond to the top (0°) and bottom

(180°) injection cases respectively. The study provides insufficient data to find which parameter was changed to obtain different values of G. However, a trend can be seen which suggests that for both the top and bottom injections, higher values of G are insensitive to the S_b as no change was observed in the S_b. Sensitivity of G on breakthrough is only observed if the value of G remains very small. This plot does not provide detailed information and thus the stability can be determined using some other dimensionless number.

6.1.2   Simulation Study using Developed Numerical Model

In order to compare the methodology adopted by Stevenson et al. (2004) and the one used in the current research, a study was conducted. The same dimensionless number was used; however, permeability was replaced by the square of the average distance between grains. Pattern 2, as described in earlier chapters, was used as a geometric pattern. The average distance between any two grains in Pattern 2 was adjusted to 0.8 mm. The simulation model as described in section 5.2 was used to simulate the cases in COMSOL. The calculations made were based on the grains domain rather than on considering the whole area enclosed in the pattern, as discussed in section 4.2.2.

Mobility ratios of 1, 3 and 10 were considered and the dimensionless number was varied by five orders of magnitude by changing the density difference of 0.1,1,10,100,1000 and 10000 kg/m^3 between the inplace and the injected fluid. Two injection scenarios of top and bottom injection were studied. The grains domain velocity of 0.017 cm/min or 2.8 x$10^{-6} m/s$ was used, which corresponds to the inlet-flow rate of 0.002 cm^3/min as calculated in section 4.2.2.5.

The breakthrough concentrations, S_b, were plotted against the Darcy–Rayleigh number, G. Breakthrough concentration is defined here as the concentration of injected fluid in the porous domain at a particular time when the injected fluid can be sensed at the exit boundary. In practice, there should have been some standard of the sensed concentration at the exit boundary as it ranged from a very small to a high value of mol/m^3. Therefore, two different breakthrough scenarios were considered in the present study. These scenarios considered different breakthrough time when a concentration front of 0.2 and 0.5 mol/m^3 was sensed at the exit boundary. Figure 6-2 shows a case

when the concentration peak of 0.2 mol/m^3 was detected at the exit boundary after 418 minutes of a case. This time is considered as breakthrough time for 0.2 mol/m^3 scenario.
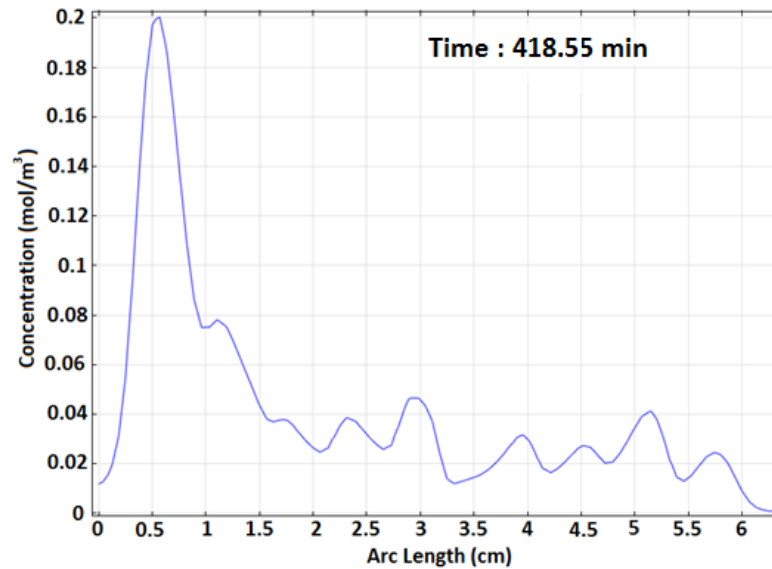
Figure 6-2: Concentration Peak 0.2 mol/m^3 at the Exit Boundary

6.1.2.1 First Breakthrough Scenario

The first scenario considers the breakthrough when the first concentration peak of 0.2 mol/m^3 was sensed at the exit boundary. The plot between S_b and G for different mobility ratios is shown in Figure 6-3. Figure 6-3 (A) shows a Cartesian plot and a semi-log plot is given in Figure 6-3 (B). The semi-log plot is plotted for only positive G values as the log values take only positive values into account and generate an error for a negative value.

Figure 6-3 (A, B) shows a similar trend of S_b versus G as reported by Stevenson et al. (2004) in Figure 6-1. However, the values of the breakthrough saturation are found to be different due to the definition of S_b. Figure 6-3 (A) shows that the bottom injection cases with negative G produces smaller S_b compared to top injection. This is due to the effects of gravity on the displacement front. For higher values of G, no significant effect of mobility ratio is noticed at fixed angles of tilt and the same value of S_b is obtained. This shows that for both, the top and bottom injection, if the density difference is high, then the S_b remains independent of the density difference and the mobility ratio. The Cartesian plot is unable to provide enough information in the region of small density differences. A semi-log plot in Figure 6-3 (B) helps to understand this region as it

shows that for small density differences, mobility ratio affects the recovery when lighter fluid is injected from the top. The Figure shows that if the mobility ratio is increased, the S_b value decreases. However, this dependence of mobility ratio on S_b is for a short transition as when the density difference increases, the values again converge to provide a similar value. Similar behaviour was observed when the light fluid is injected from the bottom, which can be witnessed by the pore-scale images shown in Figure 6-4. In order to make consistent with the vertical cases, the images of the bottom injection cases are rotated in an upside down position. The pore-scale images show that when the fluid is injected from the bottom, the mobility ratio produces a slight difference when the density difference is 100 kg/m^3. A mobility ratio of 1 helps to sweep more fluid before a 0.2 mol/m^3 front reaches the exit boundary when the density difference is 100 kg/m^3. However, when the density difference is increased to 1000 kg/m^3, the mobility ratio does not play any role as all the images seem to be very similar to each other.

(A)   (B)

Figure 6-3: Comparison between Breakthrough Saturation, Sb, (%) against the Calculated Darcy–Rayleigh Number, G, for the First Breakthrough Scenario (A) Cartesian Plot and (B) Semi-Log Plot
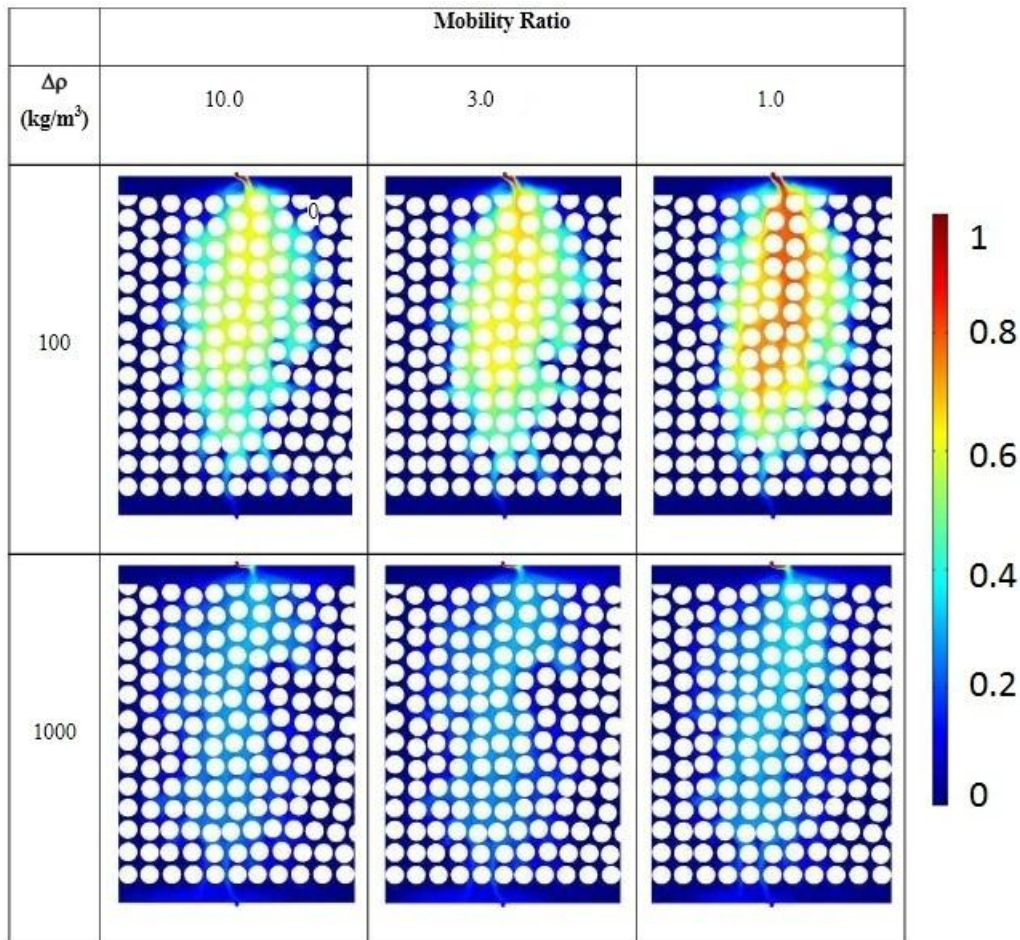
Figure 6-4: Pore-Scale Images for the First Breakthrough Scenario (Injection from Bottom)

6.1.2.2 Second Breakthrough Scenario

The second scenario considers the breakthrough when the first concentration peak of 0.5 mol/m³ was observed at the exit boundary. This breakthrough definition allows more fluid to exit the boundary. The plot between S_b and G for different mobility ratios is shown in Figure 6-5. Figure 6-5 (A) shows a Cartesian plot and a semi-log plot is given in Figure 6-5 (B). Similar to the first scenario, the semi-log plot is plotted for only positive G values as the log values take only positive values into account and generate an error for a negative value.
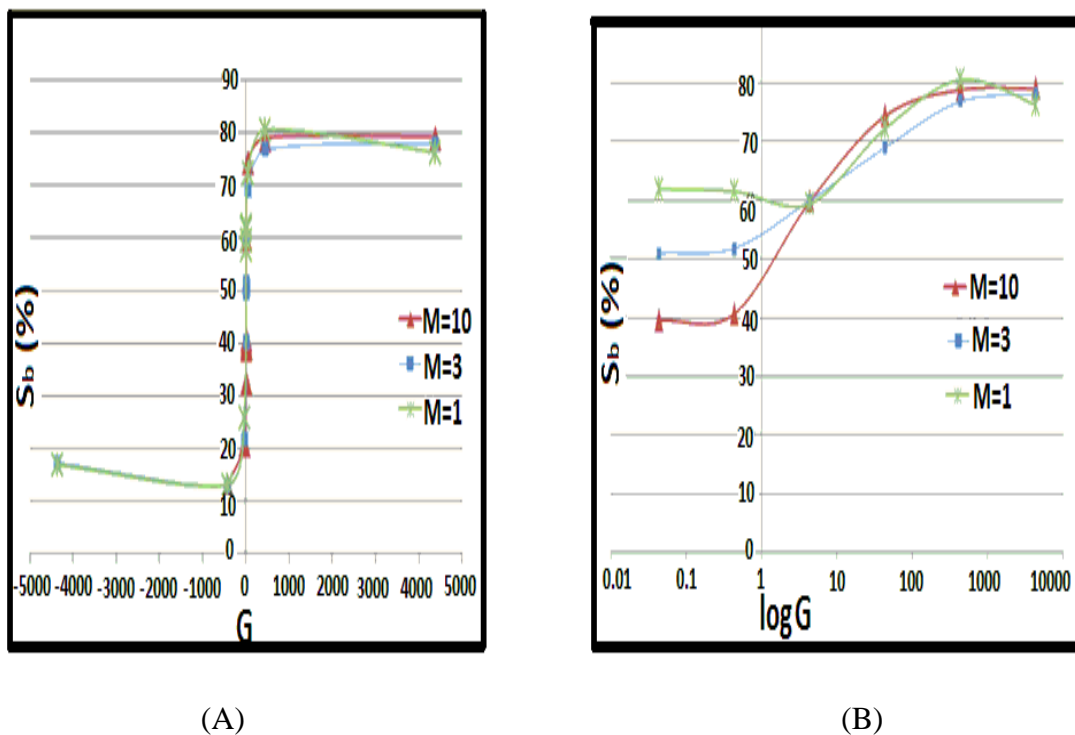
(A)　　　　　　　　　　　　　　　　　　(B)

Figure 6-5: Comparison between Breakthrough Saturation, S_b, (%) against the Calculated Darcy–Rayleigh Number, G, for the Second Breakthrough Scenario (A) Cartesian Plot and (B) Semi-Log Plot
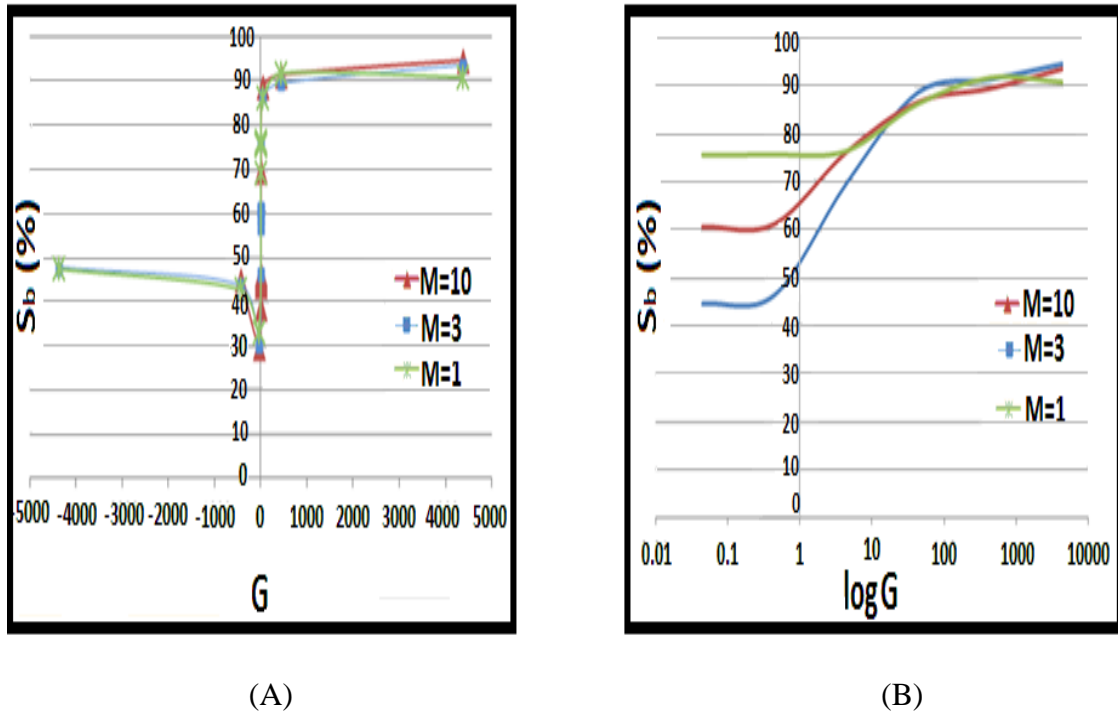
The Cartesian plot in Figure 6-5 (A) shows that for positive values of G, S_b ranges between 90–95% compared to 78–80% in the first scenario of breakthrough. This increment in S_b is obvious as more fluid was allowed to leave the system at the exit boundary to consider a breakthrough. The overall trend for the positive G values remained similar to the first scenario as the S_b reached a plateau after a short increment of G. The small range near the 0 value is not clear in the Cartesian plot, which can be clarified by the semi-log plot shown in Figure 6-5 (B) for the positive values of G. This plot also shows a similar trend as was observed in the first scenario as for smaller G values, the S_b becomes inversely related to the mobility ratio. The positive values of G suggest that for a very small density difference between the injected and the inplace fluid, S_b depends on the mobility ratio; however, S_b becomes insensitive to the mobility ratio if this density difference becomes large.

The trend in Figure 6-5 (A) for the negative values of G shows a distinctive characteristic. This Figure shows an increment in the values of S_b as the value of G increases from 0 in the negative x axis. This is because when the density difference increases, the buoyant forces become more active, promoting early breakthrough and a small concentration might be sensed at the exit boundary. However, according to the

definition of breakthrough in this particular scenario, breakthrough can only be reported to occur if a front of 0.5 mol/m^3 can be sensed at the exit boundary, which requires more fluid to be displaced from the domain. This is further clarified in Figure 6-6 which shows the breakthrough concentration profile in the pore-scale images when the lighter fluid is injected from the bottom. The pore-scale images were captured when the peak of 0.5 mol/m^3 was sensed at the top exit boundary. The pore-scale images show that when the density difference is 1000 kg/m^3, a large volume of inplace fluid is required to be swept out from the system in order to achieve a breakthrough saturation of 0.5 mol/m^3 at the exit boundary.
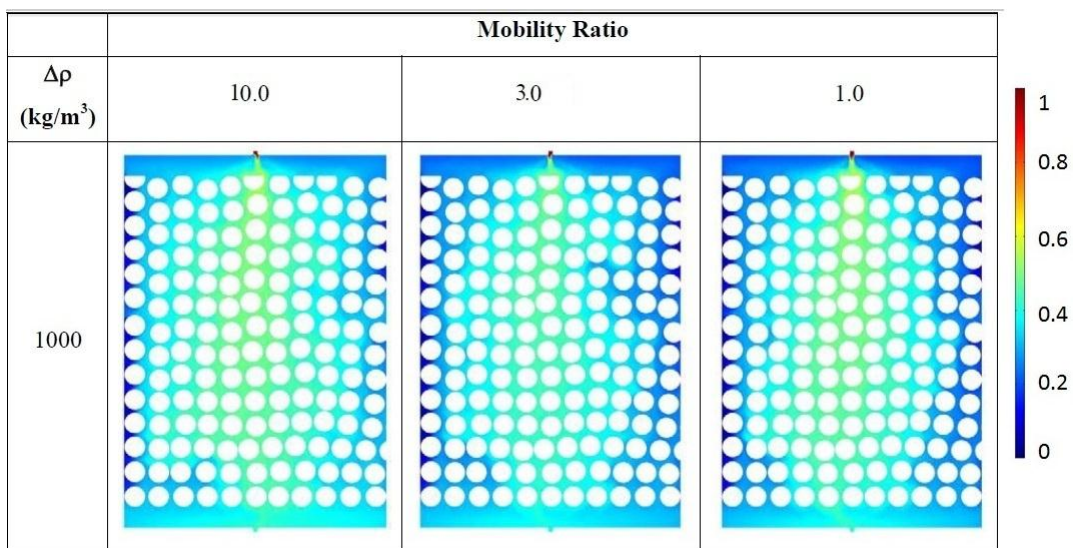
Figure 6-6: Pore-Scale Images for the Second Breakthrough Scenario (Injection from Bottom)

A comparison of the results with Stevenson et al. (2004) suggests an analogy in terms of a general trend of S_b behaviours. However, Stevenson et al. considered an ideal scenario of pipe flow according to which a pore throat behaves as a pipe. Also, no fluid mixing was considered, which is one of the prime requirements of miscible flooding. These approximations result in an over-estimation of S_b, which approaches approximately 100%. The definition of breakthrough also needs to be clarified. It is observed, however, that when the S_b definition is increased to a larger value, abrupt change in the S_b value is observed. Furthermore, Stevenson et al. (2004) considered only two extreme scenarios of top and bottom injection. Therefore, more sensitivity work was required in order to investigate the effect at the intermediate angles of tilt. In

addition, different scenarios of mobility ratio and heterogeneity were required to be studied.

6.2 Sensitivity Studies

Sensitivity analysis was conducted to investigate the effect of different parameters on the stability of gravity-dominated miscible displacement. The sensitivity studies were conducted at a lower domain velocity because unlike the experiments, the simulation allows various scenarios at a desirable condition to be tested depending on the availability of the computing facilities. The sensitivity analysis for the present research has been divided into three main categories:

1. Based on mobility ratio, density difference and angle of tilt.

2. Based on different domain velocities.

3. Based on heterogeneity of geometry.

6.2.1 Sensitivity Based on Mobility Ratio, Density and Angle of Tilt

The aim of this study was to identify the role of fluid properties (density and viscosity) on the gravity-dominated miscible displacement at different dip angles. Pattern 2 described in section 4.1.1.1 and Figure 4-12 was used in this sensitivity study. All the cases in this sensitivity study were simulated at a fixed velocity. Stalkup (1983) stated that the average velocity of fluids in the reservoir varies between 0.1 and 1.0 ft/day ($3.5x10^{-7}$ – 3.5 $x10^{-6}$m/s). Therefore, a value of average grains domain velocity was required to lie in this range. A value of 0.8 ft/day ($2.8x10^{-6}$m/s) was thus deemed appropriate for this sensitivity study. The inlet velocity corresponding to this grains domain velocity was derived as 7.3 x 10^{-5} m/s using equation (5.10). In addition, a diffusion coefficient of a CO_2–oil system (2 x 10^{-9} m^2/s) as calculated by Grogan et al. (1988) for the Maljamar Oil, was used for the sensitivity studies. Further details of the variables used in the sensitivity study are given in Table 6-1.

Table 6-1: Variables Range in the Sensitivity Study

Variable	Values Used
Dip Angle (with Respect to Vertical)	0°, 30°, 45°, 60°, 90°, 120°, 135°, 150° and 180°
Mobility Ratio ($\mu_{inplace}/\mu_{injected}$)	1, 3, 10 and 100
Density Difference ($\rho_{inplace}-\rho_{injected}$)	50, 100, 200 , 400 , 600, 800 and 900 kg/m^3

The different combinations of mobility ratios and density differences given in Table 6-1 were simulated with different dipping angles. A breakthrough scenario of 0.2 mol/m^3 as shown in Figure 6-2 was adopted in the sensitivity study. Based on the force of gravity acting during the miscible displacement, the obtained results were divided into two regions:

6.2.1.1 Region 1

This refers to a region when the dipping angle remains equal to or below 90° with respect to the vertical, that is, $0 \leq \theta \leq 90$. The sensitivity study was conducted by simulating the various density and mobility scenarios mentioned in Table 6-1 with dipping angles of 0°, 30°, 45°, 60° and 90°. Snapshots given in Figure 6-7 (A–D) show the saturation profiles of the injected fluid at breakthrough in the porous domain. The breakthrough profiles in Figure 6-7 compare the effect of density change and angular tilts for mobility ratios (M) of 1, 3, 10 and 100. Figure 6-7 (A–D) shows that the effects of overriding appear in all density difference cases when the dip angle increases from 0° with respect to the vertical. The lighter injected fluid tends to override the dense in situ fluid, leaving small to large proportions of unswept zones depending on the increase of angular tilt.

6.2.1.1.1 0 Degree Cases

By comparing cases of density difference—50 kg/m^3 and 200 kg/m^3 at 0° with M = 1 in Figure 6-7 (A)—it can be observed that when the density difference is increased from 50 to 200 kg/m^3, a little improvement in breakthrough profile occurs, which might lead to a slightly better recovery factor. This improvement occurs due to the increment of the

density difference in the vertical direction ($\theta = 0$) because the lighter injected fluid tends to stay in the top region, which promotes piston-like displacement. The gravity segregation helps the displacement, which results in a small increment of the S_b. Comparing the cases of density difference of 200 kg/m^3 and 900 kg/m^3 at 0° shows that the further increment in the density difference does not produce any significant effect at 0°.

Figure 6-8 (A–D) and Figure 6-9 (A–D) further elaborate the phenomenon described in the above paragraph. Figure 6-8 (A–D) shows the graphs of S_b versus cosine of dipping angles of 0$\leq\theta\leq$90 for various density differences at particular mobility ratio, and Figure 6-9 (A–D) shows the graphs of S_b versus cosine of dipping angles for different mobility ratios at particular density differences. Figure 6-8 shows that for all mobility ratios (that is, M = 1, 2, 10 and 100) at 0° (cos θ = 1), a case of $\Delta\rho$ = 50 kg/m^3 produces the least S_b (or recovery) among the rest of the cases with different densities at the respective mobility ratio. Figure 6-9 shows that at 0° the density difference of 50 kg/m^3 (shown in Figure 6-9 (A)) produces the least among the rest of the density difference cases (Figure 6-9 (B–D)).

6.2.1.1.2 Cases with Dip Angle Higher than 0 Degrees

Considering Figure 6-7 (A) again, it can be noticed that when the dipping angle increases from 0°, the trend described in the above paragraphs is reversed; that is, the increase in density difference acts against the stability of the process. This phenomenon can be observed when comparing cases of density difference of 50 kg/m^3 and 900 kg/m^3 at angles more than 0° in M= 1. The Figure 6-7 (A) shows that when the density difference is increased in the 45° or 60° cases, the gravity segregation acts against the displacement. The concentration of lighter injected fluid in the pattern reduces and it tends to override the inplace fluid. This trend remains the same when the tilt angle is progressively increased to 90°. At 90°, when the density difference is increased to 900 kg/m^3, the effect of overriding reaches a maximum value and the breakthrough occurs at very small injected fluid concentration. This effect is clearer in Figure 6-8 (A–D), which shows that in all mobility ratio cases, when dip angle (or cos θ) increases, the S_b of injected fluid (or recovery of inplace fluid) falls. The $\Delta\rho$ = 50kg/m^3 case, which was initially producing the least S_b among all the cases at 0° dip angle, produces the highest

S_b at 45°–90° (i.e.$0{\leq}cos\theta{\leq}0.7$). This shows that the effect of increasing density difference produces a negative impact on cases with a more than 0° tilt angle.

6.2.1.1.3 Role of Viscosity Change

If a comparison is made between respective dip angle cases of M= 1 in Figure 6-7 (A) and M = 100 in Figure 6-7 (D) with the density difference ($\Delta\rho$) of 50 kg/m^3 only, it can be observed that an increase in M from 1 to 100 causes more channelling; that is, the increase in M and the increased angular dip both act against the stability of the displacing front at this $\Delta\rho$.

If a comparison is made between respective dip angle cases of M= 1 in Figure 6-7 (A) and M = 100 in Figure 6-7 (D) with the density difference of 200 and 900 kg/m^3, it can be noted that the increase in M from 1 to 100 causes little or no effect as the corresponding images of the same angle show either a small, or no, difference. Thus, the effects of mobility are more prominent when the density difference is small; however, when the density difference is high, the viscosity effects become suppressed and the gravity-overriding phenomenon dominates. For example, at 90°, when M is increased from 1 to 100, more viscous fingering with gravity override can be seen in cases of 50 kg/m^3 compared with the cases of 200 kg/m^3.

This effect can be clarified in Figure 6-9. At first, consider Figure 6-9 (A) which shows that when $\Delta\rho$ is 50 kg/m^3 then the increment in M produces a negative impact on Sb (or recovery). Increase in M causes more instability and the S_b saturation to fall, which can be witnessed by the separated lines in Figure 6-9 (A). This shows that at lower $\Delta\rho$, the competition of viscous and gravity forces exists, especially in the cases with higher dip angles, which results in lower values of S_b when the dip angle and M are high. It is noticed, however, that when the density difference is increased—see Figure 6-9 (B–D)—the effect of increase in M produces no effect as all the curves overlap each other.
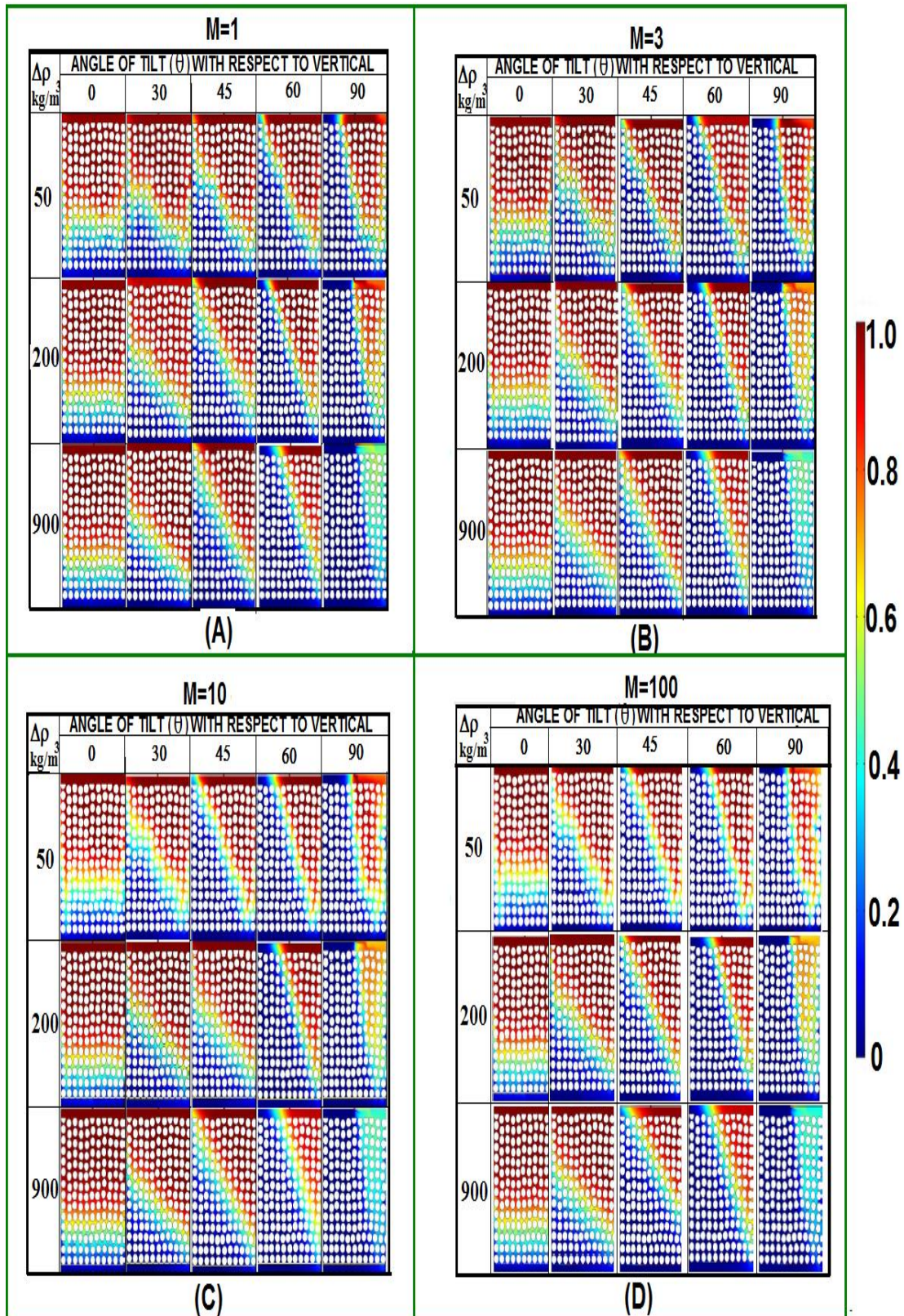
Figure 6-7: Snapshots for Different Mobility Ratios and Density Differences Cases for Region 1
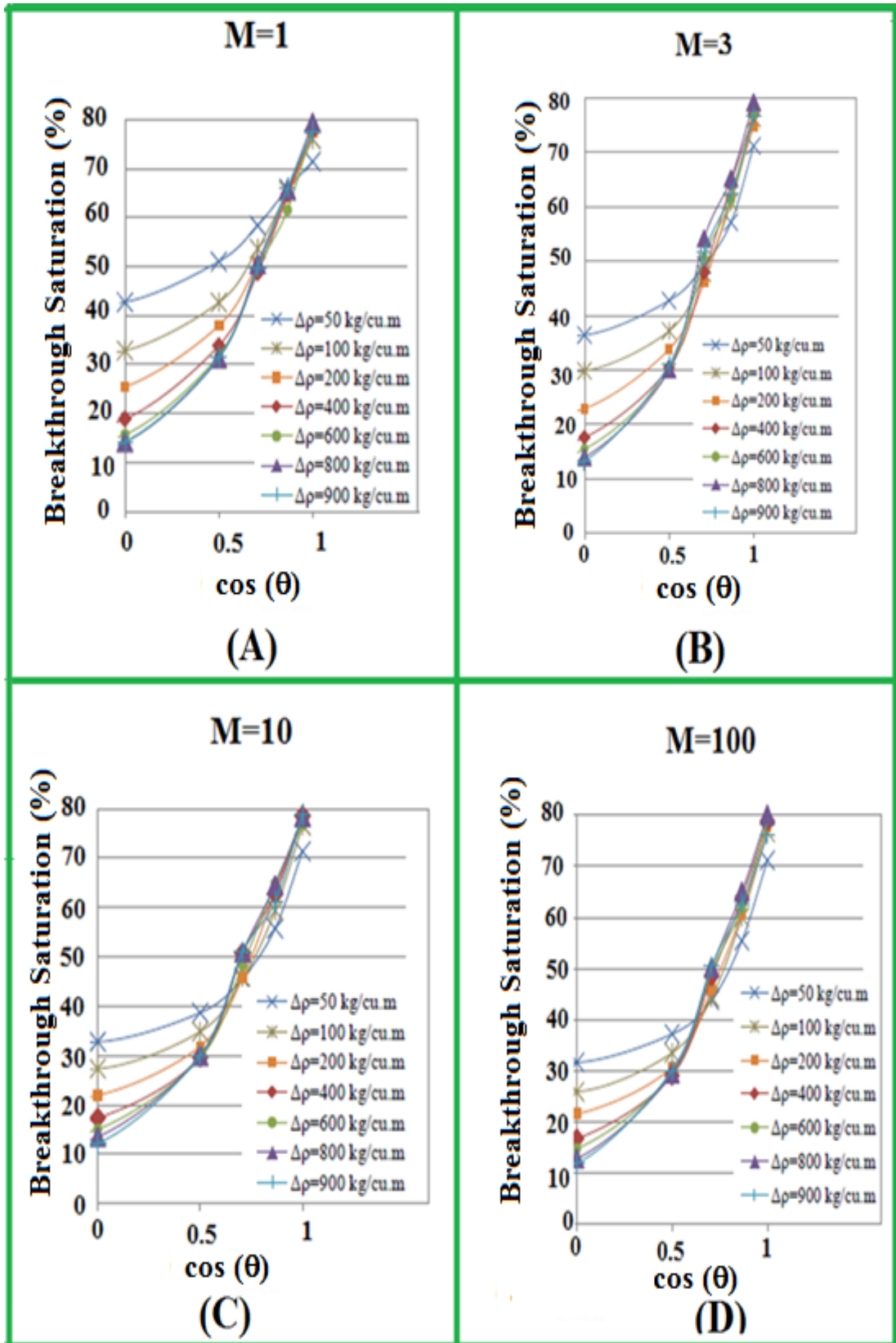
Figure 6-8: Graphs of S_b vs. Cos θ for Various Density Differences at Particular Mobility Ratios in Region 1
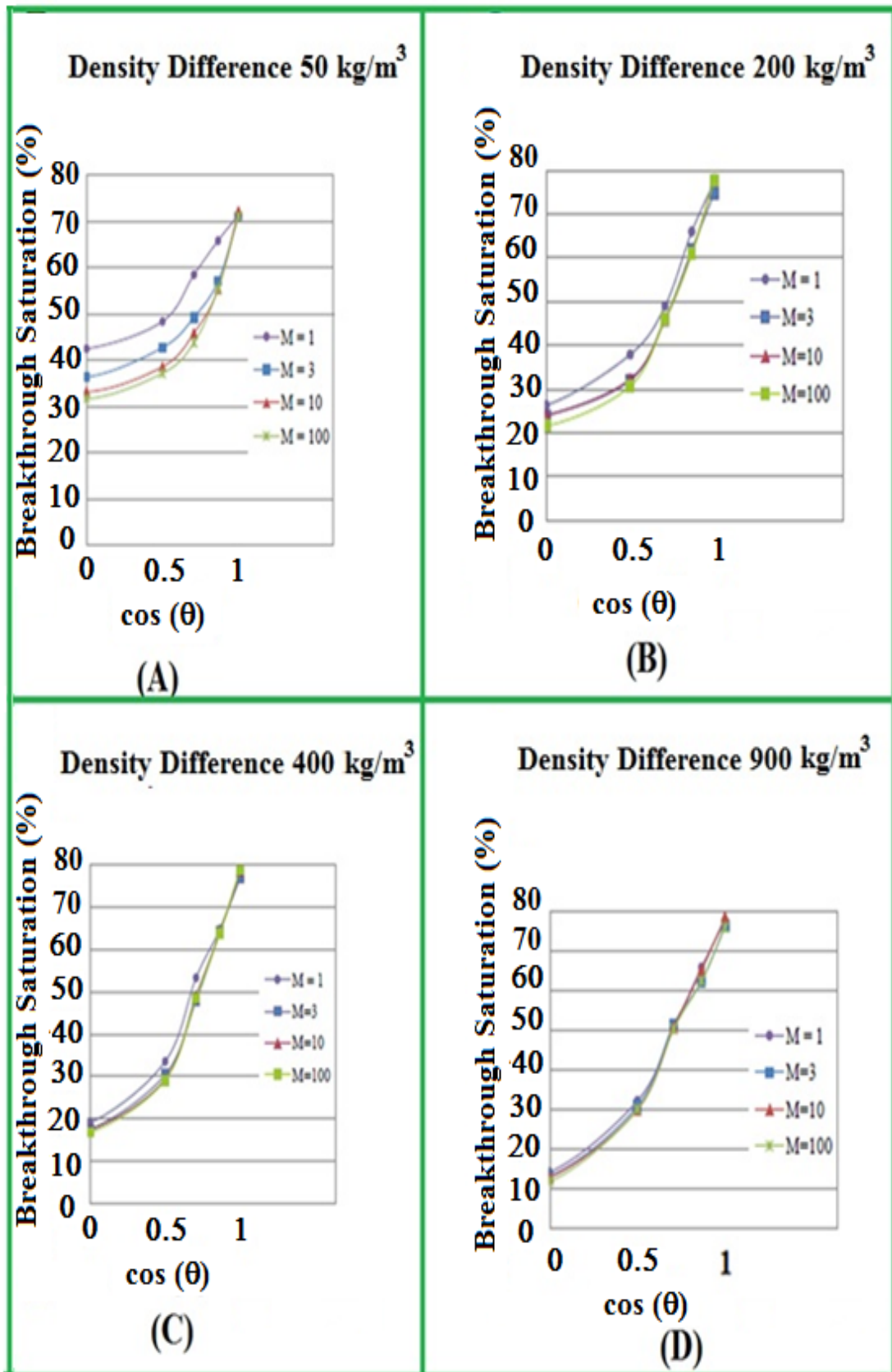
Figure 6-9: Graphs of S_b vs. Cos θ for Various Mobility Ratios at Particular Density Differences in Region 1
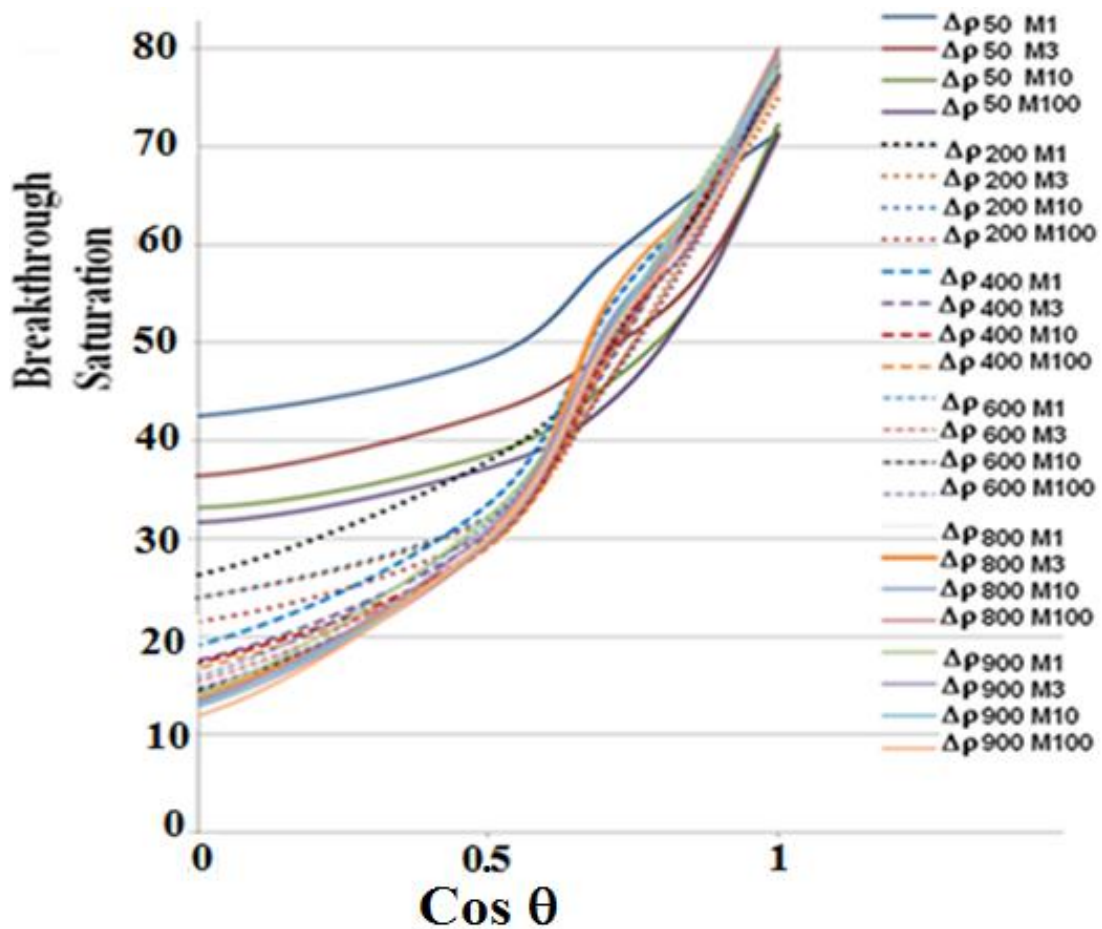
Figure 6-10: Breakthrough Saturation vs. Cos (θ) for Range of Mobility Ratios and Density Differences

Figure 6-8 and Figure 6-9 were combined in Figure 6-10 to elaborate the concept. This figure shows that the role of the angle of dip (θ) is found to be the most important parameter, especially when the density difference is equal to, or greater than, 200 kg/m^3. As the angle of tilt increases from 0° (or cos θ = 1), the breakthrough saturation starts to decrease. This trend continues as the angle of tilt approaches 90° (or cos θ = 0). All the other density difference curves fall on top of this curve regardless of the change of mobility ratio. This signifies the fact that when the density difference is large, density forces are dominating and the effects of gravity are more predominant, which causes the decrease in the breakthrough saturation. When the density difference is less than 200 kg/m^3, the mobility ratio between the inplace and the displacing fluid has an increased effect, and the displacing and inplace fluids behave similarly because the density difference between the two fluids is less.

6.2.1.2 Region 2

The region 2 refers to a region where the gravity forces act against the fluid displacement, that is, $90<\theta\leq180$. Pore-scale images outlined in Figure 6-11 show saturation profiles of the injected fluid at breakthrough. These breakthrough profiles compare the effects of density change and angular tilt between 120° and 180° with viscosity ratios of 1, 3, 10 and 100 respectively.

By comparing cases of density difference of 50 kg/m^3 at angles between 120° and 180° with M = 1 in Figure 6-11 (A), it can be noticed that since gravity acts against the displacement, the injected fluid tends to rise and breakthrough, leaving large proportions of the inplace fluid. When the dip angle is increased from 120° to 180°, a small variation in the front propagation is observed. The gravity finger tends to rise in the middle of the pattern leaving a great proportion along its side, unswept. Since the volume of the pattern is not large, a small variation in the breakthrough saturation was expected.

By comparing cases of density difference of 50 kg/m^3 and 200 kg/m^3 at angles between 120° and 180° with M = 1 in Figure 6-11 (A), it can be noticed that buoyancy forces are more prominent and increasing density difference promotes the gravity-fingering phenomenon. In both of the cases it is to be noted that when the dip angle reaches 180° the gravity fingering reaches maximum and a single finger appears that tends to breakthrough at the exit boundary. It is also to be noted, though, that the dip angle does not have a large impact on the breakthrough as was observed in Region 1 (that is, $0\leq\theta\leq90$) because in Region 2 (that is, $90<\theta\leq180$) the gravity acts against the displacement and the lighter fluid tends to reach the boundary as quickly as possible.

By comparing cases of density difference of 50 kg/m^3 at angles between 120° and 180° with M = 1 and M = 100 in Figure 6-11 (A) and Figure 6-11 (D), it can be noticed that when the mobility ratio is increased from 1 to 100 the viscous scattering effects were witnessed along with gravity fingers. This further reduces the process efficiency and the breakthrough occurs, displacing a very small proportion of the inplace fluid. A similar trend can be observed when a comparison is made for the cases of 200 kg/m^3 at angles between 120° and 180° with M = 1 and M = 100 in Figure 6-11 (A) and Figure 6-11 (D). It is, noticed, however, that when a comparison is made for the cases of 900 kg/m^3

at angles between 120° and 180° with M = 1 and M = 100 in Figure 6-11 (A) and Figure 6-11 (D), no significant change was observed. This is because when the density difference is high, the viscous forces do not play any significant role and even the M = 100 behaves similarly to that of M = 1. Thus, similar to Region 1, the effect of M in Region 2 also occurs when the density difference is small. However, the role of angular dip is not as significant in Region 2 as it is in Region 1.
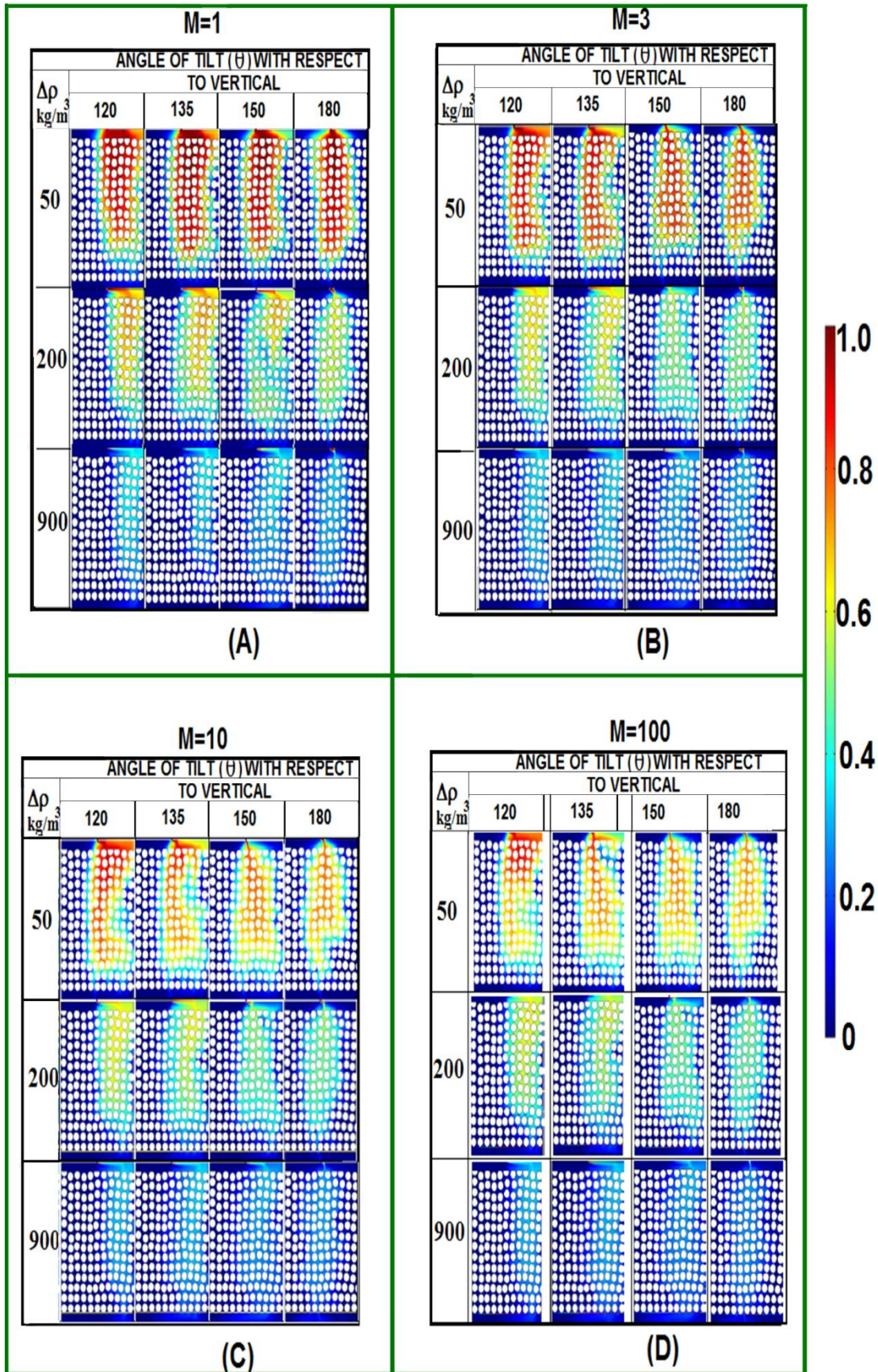
Figure 6-11: Snapshots for Different Mobility Ratios and Density Differences Cases for Region 2

Figure 6-12 and Figure 6-13 further elaborate the concept that changing the angle at the fixed density difference and mobility ratio produces little or no effect on S_b. A respective line therefore became approximately flat regardless of the change of angular tilt. Towards the end of the line at 180°, the S_b value drops due to the opposing gravity forces. Angular tilt in all the cases does not show any sensitivity.

Figure 6-13 (A–D) shows that when the density difference is low, then mobility ratio could be a sensitive parameter. However, when the difference increases, the viscous forces become suppressed by the gravity forces. Figure 6-13 (D) shows that when the density difference reaches 900 kg/m^3, the mobility effect is suppressed and all the lines fall approximately on top of each other.

It is to be noted that throughout this sensitivity study the breakthrough concentration criteria of 0.2 mol/m^3 is used which might be low, especially for the cases when a light fluid is injected against the gravity. In these cases, buoyancy forces are more prominent and the light injected fluid can form channels through the porous model. As a result, a small concentration of the injected fluid can be sensed at the outlet boundary too early, which results in constant breakthrough saturations at various angles between 120° and 180°. The overall results of region 1 and 2 obtained in this sensitivity study are shown in Figure 6-14.
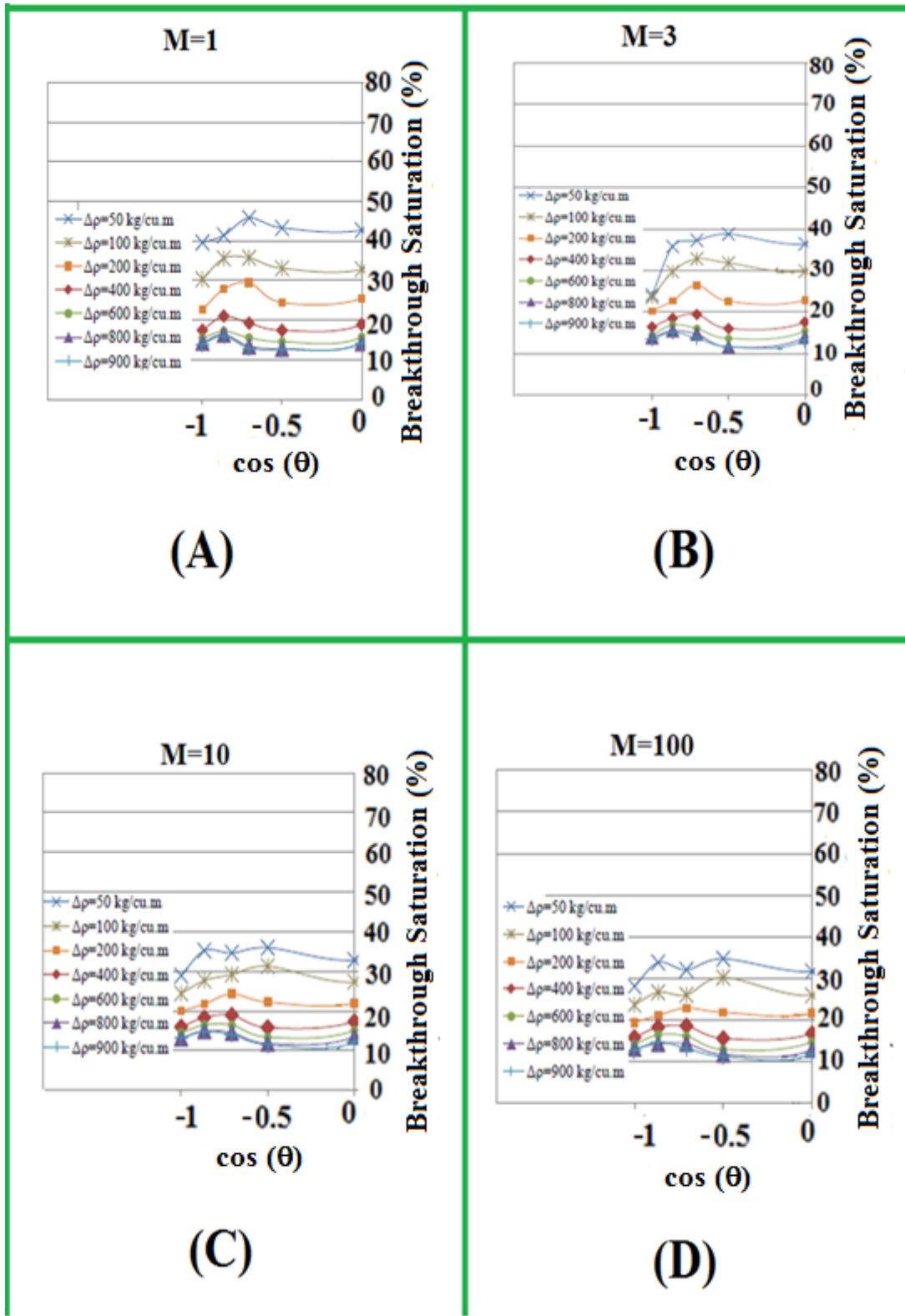
Figure 6-12: Graphs of S_b vs. Cos θ for Various Density Differences at Particular Mobility Ratios in Region 2
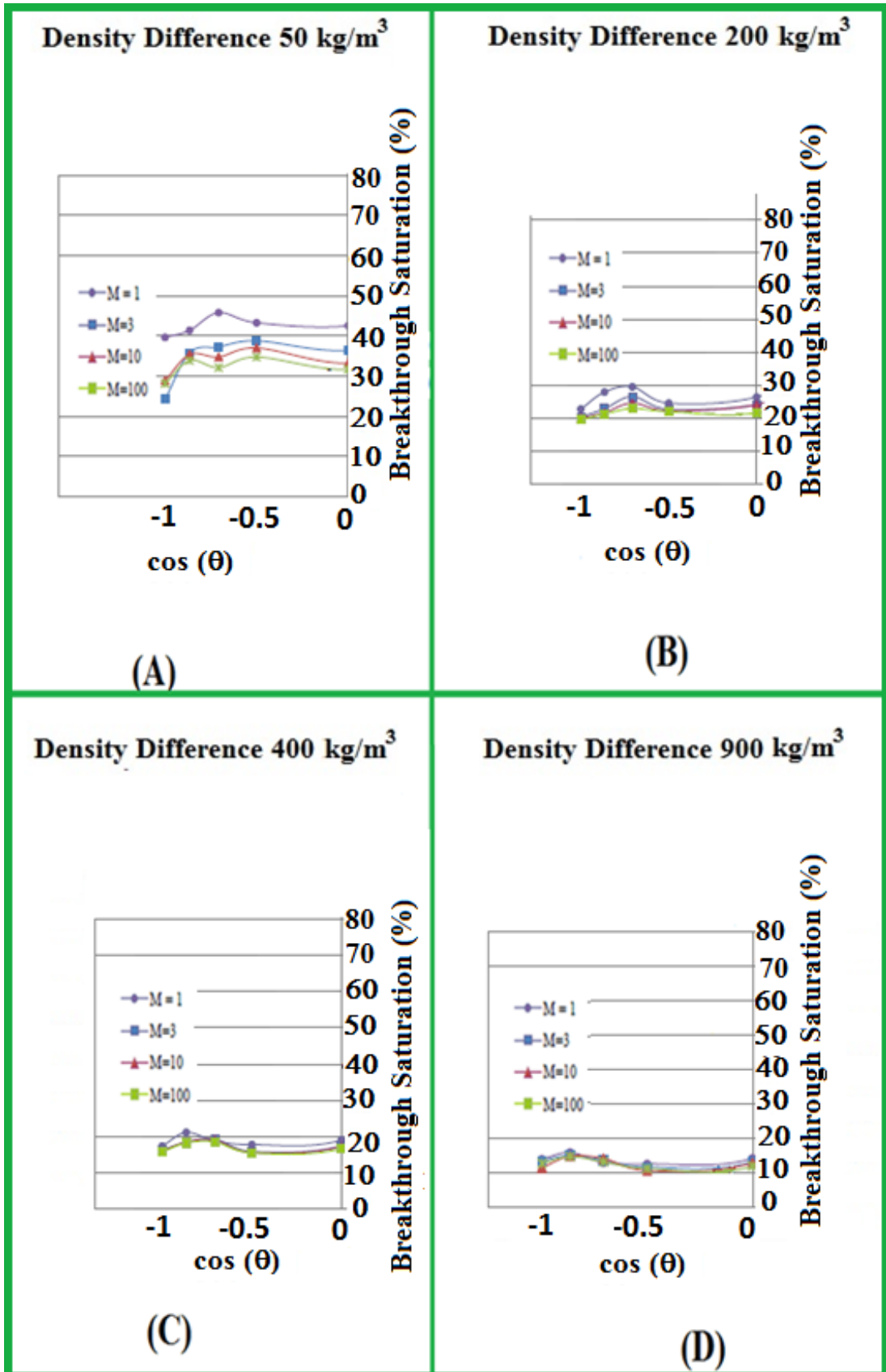
Figure 6-13: Graphs of S_b vs. Cos θ for Various Mobility Ratios at Particular Density Differences in Region 2

Figure 6-14: Breakthrough Saturation vs Cos (θ) for Range of Mobility Ratios and Density Differences using Domain Velocity of 0.8 ft/day

6.2.2 Sensitivity Based on Domain Velocity

A sensitivity analysis was performed in order to evaluate the effect of the domain velocity on gravity-dominated miscible displacement. A smaller velocity of 3.71×10^{-5} m/s was selected, which represents a domain velocity of 0.4 ft/day (1.411×10^{-6} m/s) by using Equation (5.10). The aim of investigating the effect of domain velocity was to evaluate whether or not velocity assists in the gravity-dominated miscible displacement process. A simulation study was performed with the density differences between 50 kg/m^3 and 900 kg/m^3, with mobility ratios ranging from 1 to 100, and with nine angles of tilt with respect to the vertical plane, ranging from 0° to 180°. Figure 6-15 shows the plot of breakthrough saturation (S_b) versus cos θ for this sensitivity study. Comparing the results obtained in this study with the results from the previous sensitivity study as given in Figure 6-14 shows that the reduction in the domain velocity ultimately reduces the inertial effects, which in turn decreases the value of breakthrough saturation compared with the case of higher velocity. These results confirm the statement of Blunt and Fayers et al. (1993) given in Chapter 1 that when the flow rate is high, then a small

time is allowed for fluids to settle, which might prevent the overriding phenomenon. Since in the present study the model length is small, this effect is also witnessed.

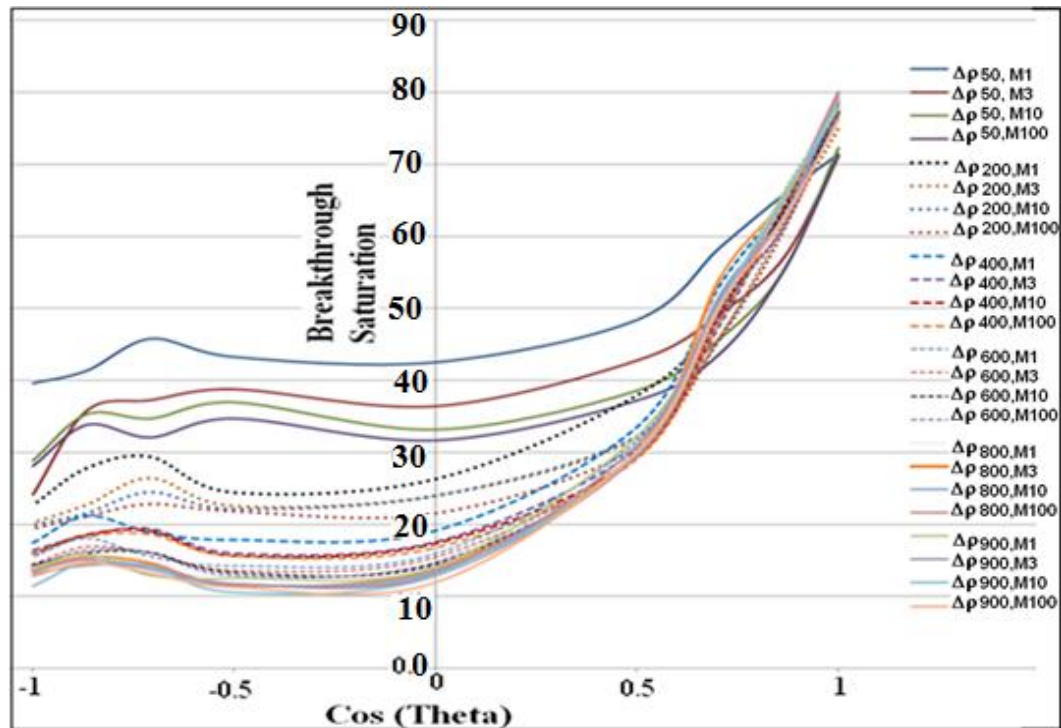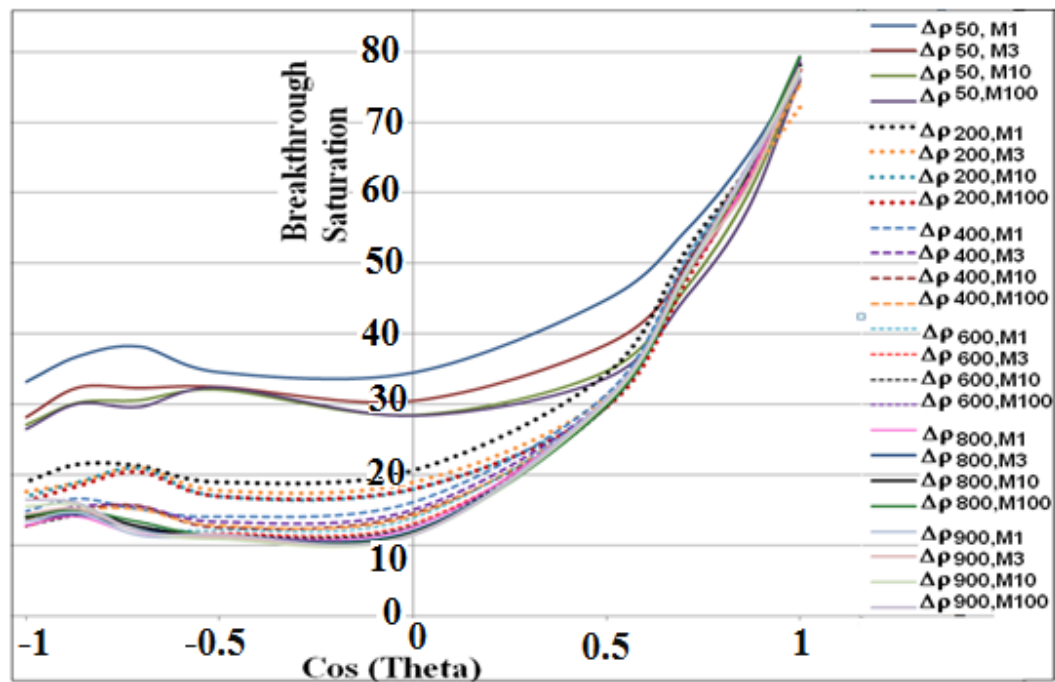

Figure 6-15: Breakthrough Saturation vs Cos (θ) for Range of Mobility Ratios and Density Differences using Domain Velocity of 0.4 ft/day

6.2.3 Sensitivity Based on Heterogeneity

Sensitivity based on heterogeneity is divided into two parts:

a) Heterogeneity based on grains packing in a single layer (Local Heterogeneity).

b) Heterogeneity based on layers of different grains packing (Global Heterogeneity).

6.2.3.1 Heterogeneity Based on Grains Packing

This sensitivity study was conducted to determine the effect of localised heterogeneity on miscible displacement under gravity. To study this effect, three new patterns were generated. The patterns represented the scenarios of tightly packed, moderately packed and loosely packed heterogeneous systems. All three patterns were generated using 253 circular grains with a 0.15 cm radius. The distance between the grains' centres were varied to produce the effect of heterogeneity. The sizes of the patterns were therefore

different from each other as the distance between the grains were varied. The geometric arrangements of the designed patterns for this sensitivity study are given in Table 6-2.
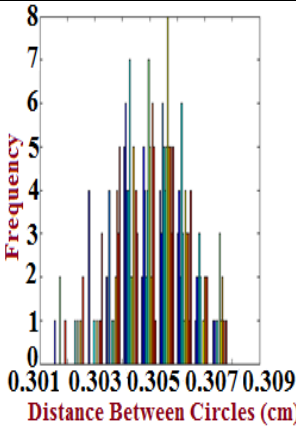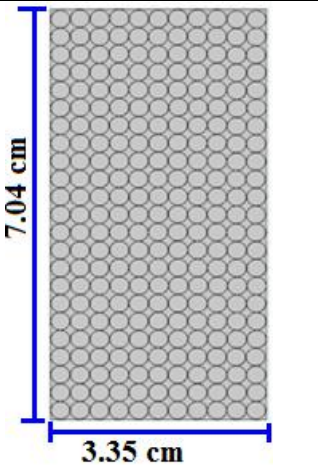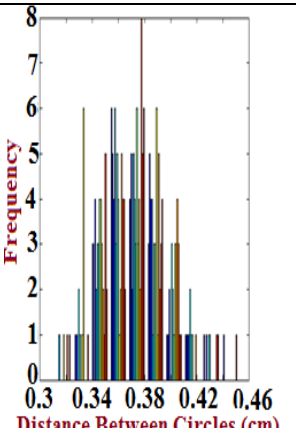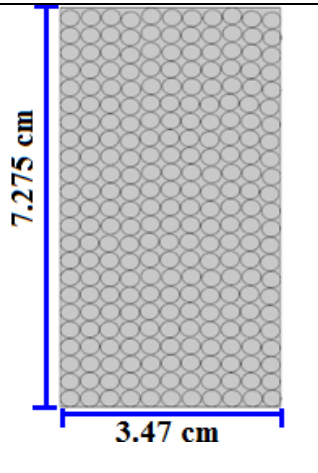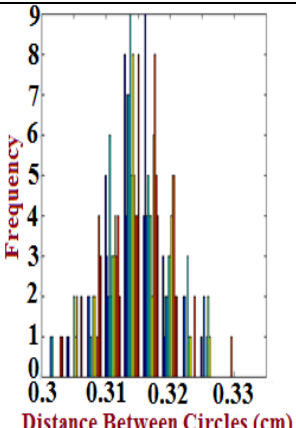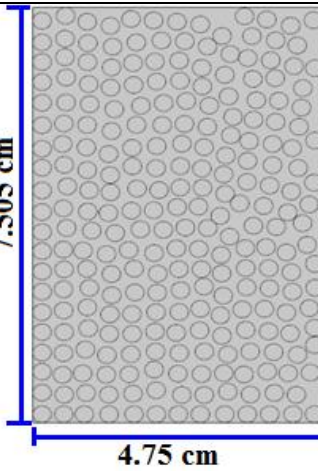
Table 6-2: Geometric Arrangements of the Designed Patterns

Property	Tight Pack	Moderate Pack	Loose Pack
Mean Distance between the centre of any two circles (cm)	0.305	0.315	0.37
Mean Distance between any two circles' edge (cm)	0.305–0.3 = 0.005	0.315–0.3 = 0.015	0.37–0.3 = 0.07
Standard Deviation (cm)	1.25×10^{-3}	5×10^{-3}	2.33×10^{-2}

The patterns were generated using the MATLAB program given in Appendix A. The generated patterns along with the grains distribution and the values of the patterns' porosities are shown in Table 6-3. The mobility ratio M and the density difference were adjusted to 1 and 100 kg/m^3 respectively. Simulation studies were conducted at an angle of 0°, 90° and 180° to study the extreme scenarios.

The injection of fluid was carried out throughout the inlet boundary rather than through a needle connection. The injection velocity was calculated so that it represented the domain velocity of 0.4 ft/day (1.411×10^{-6} m/s). Equation (5.10) was used to convert the domain velocity to the injection velocity. The depth of the patterns was assumed uniform in the calculation. Inlet velocities of 3.44×10^{-7} m/s, 4.19×10^{-7} m/s and 7.12×10^{-7} m/s were obtained for tight, moderate and loose patterns respectively, which represents the domain velocity of 0.4 ft/day (1.411×10^{-6} m/s). in the respective domains. Breakthrough was considered to have occurred when the leading front reached a concentration value of 0.2 mol/m^3. Domain concentration was recorded at that breakthrough time for all cases.

Table 6-3: Patterns used to Study Heterogeneity Based on Grains Packing

Pattern	Distribution of Centre – Centre Distance	Pattern Schematic	Total Area cm²	Porous Area cm²	Porosity
Tight Pack			23.5	5.76	0.24
Moderate Pack			25.2	7.496	0.297
Loose Pack			35.6	18	0.505

The snapshots at the breakthrough are reported in Table 6-4 which shows that the effect of dip angle is prominent in the loose packing, but insensitive in the tight and moderate grain packing. The narrow path between the grains increases the fluid mixing in the tight and moderate packing, which suppresses the gravity effects.

Table 6-4: Snapshots at the Breakthrough
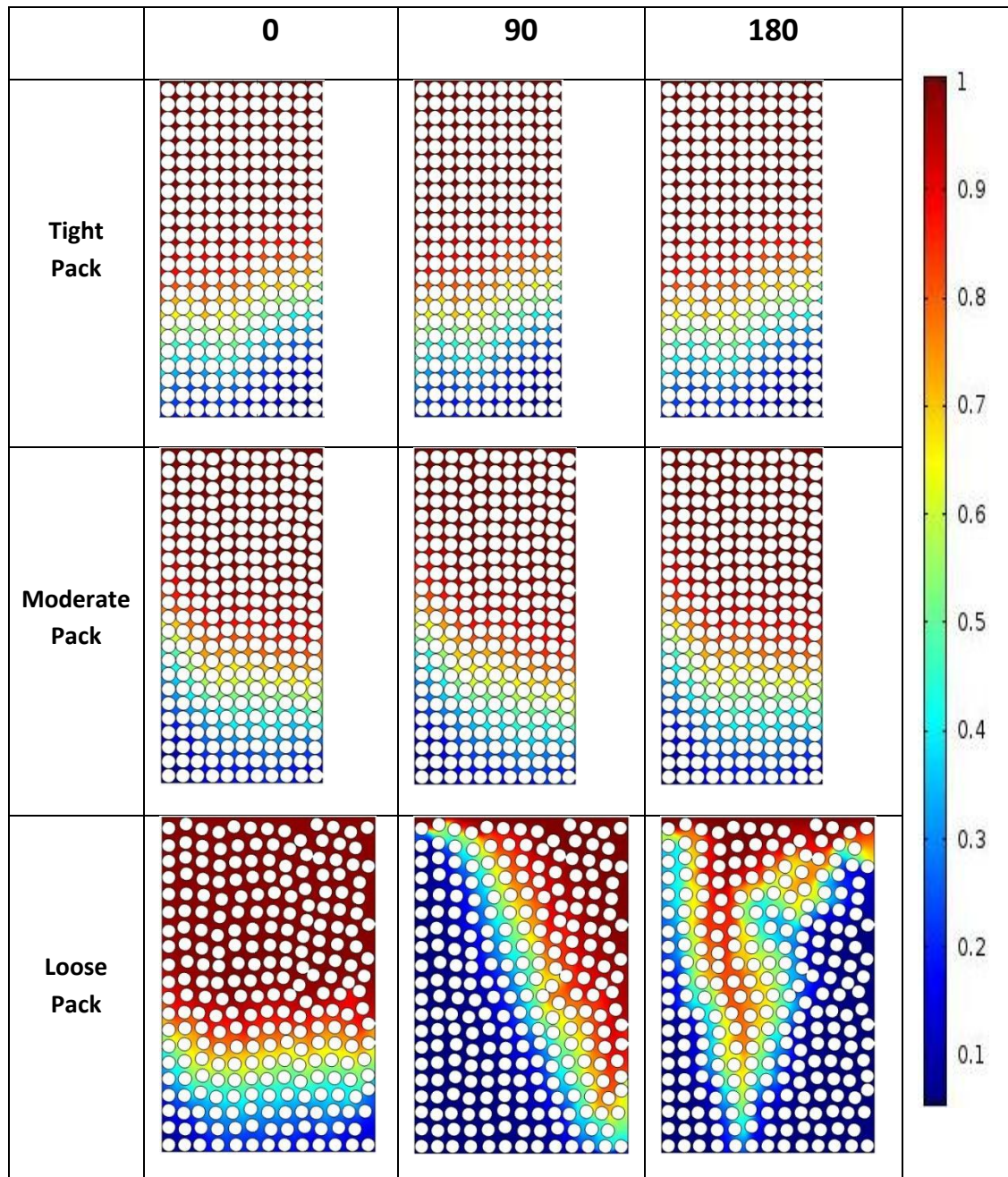
The gravity effect might be visible in the moderate and tight packing if the length of the pattern increases. However, due to computational limitations for the present research it

was not possible to simulate long patterns. Nevertheless, a study was performed to examine the effects of different layers of grains' patterns. This study aimed to provide more information about the interplay between gravity and mixing.

6.2.3.2 Heterogeneity Based on Layers of Different Grains Packing

In order to investigate the effect of different layers of grains, a pattern was designed using a MALTAB program given in Appendix D. Two layers of grains were generated so that the porosity of one pattern was half of the porosity of the other pattern. Both patterns contained circular grains with a radius of 0.15 cm. The configuration of the two layers is given in Table 6-5 and the geometric distribution is given in Figure 6-16.

Table 6-5: Configuration of Pattern used to Study Heterogeneity Based on Layers of Different Grains Packing

Property	Pattern 2 (Bottom Layer)	Pattern 1 (Top Layer)
Pore Area (COMSOL) (cm^2)	5.21	7.87
Actual Area (cm^2)	22.04	16.46
Porosity	5.21/22.04 0.236	7.87/16.46 = 0.478
Ratio of Porosities	$\Phi2/\Phi1 = 0.236/0.478 = 0.5$ => $\Phi2 = 0.5\ \Phi1$	
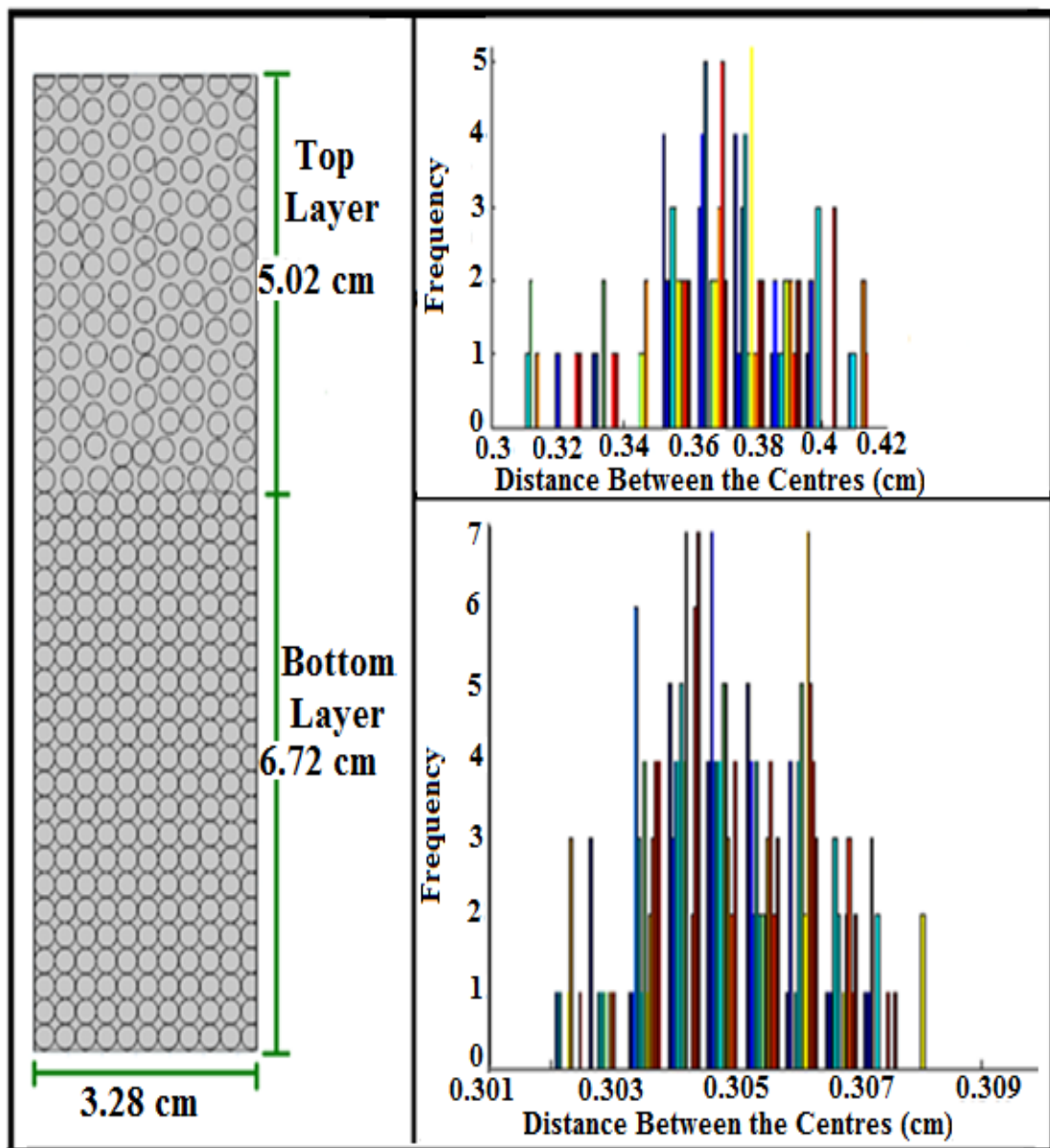
Figure 6-16: Pattern used to Study Heterogeneity Based on Layers of Different Grains Packing

Three angular dips of 0°, 90° and 180° were simulated to study the three extreme scenarios. Inlet velocity of 4.73 x 10^{-7} m/s was calculated by using Equation (5.10) which represents t

he average domain velocity of 0.4 ft/day (1.411 x 10^{-6} m/s). in the two layers. It is to be noted that the fluid velocity in the tightly packed layer needed to be higher than that for the loosely packed layer. Therefore, individual domain velocity could not be maintained with a single inlet velocity. Hence, the average velocity was calculated based on the

total porous and original areas. The injection was carried out throughout the inlet boundary of the top layer—that is, the loose pattern.

The results of the simulation are given in Figure 6-17. The two columns in the Figure show the breakthrough profiles when the breakthrough of injected fluid occurs in the top and bottom layers respectively.

For the case of 0°, Figure 6-17 shows that the injection front is nearly flat and the displacement is almost piston-like in the top layer. Besides a few signs of penetration, the overall front is fairly uniform at the breakthrough. This provides a fairly stabilised feed to the bottom layer and, due to gravity effects and small grains spacing, the trend of a stabilised front tends to continue until the breakthrough occurs.

Figure 6-17 shows that for the 90° case, the gravity effects are prominent in the top layer where the packing of the grains is loose. The injected fluid tends to override and the behaviour is similar as was described in section 6.2.1. The dip angle plays a very important role here as the injected fluid tends to override the inplace fluid. Therefore, when the breakthrough occurs in the top layer, the injected fluid displaces most of the upper section while the lower section of the model remains unswept. This provides a fairly unstable feed to the tight bottom layer. The results show, however, that when the breakthrough occurs in the bottom layer, almost all of the inplace fluid in the top layer is displaced. In addition, a large proportion of the inplace fluid in the bottom layer is displaced too. The breakthrough profile shows some signs of injected fluid overriding in the bottom layer; however, the extent of overriding is less compared to that which occurs in the top layer. This shows that although the feed to the bottom layer is fairly unstable, the tight grains packing helps to stabilise the displacing front. This behaviour shows that the tight grains arrangement enhances the effect of dispersion and fluid mixing, which helps to counter the negative effect of gravitational forces which cause the lighter injected fluid to override.

The results for the 180° case show similar behaviour to that of the 90° case. The effect of gravity is prominent in the loose pattern and a gravity tongue was witnessed when the breakthrough occurred in the top layer. It is noted, however, that the tight grains arrangement helps to counter the effect of gravity due to dispersion and diffusion effects, which results in a fairly stable breakthrough at the bottom layer's boundary.
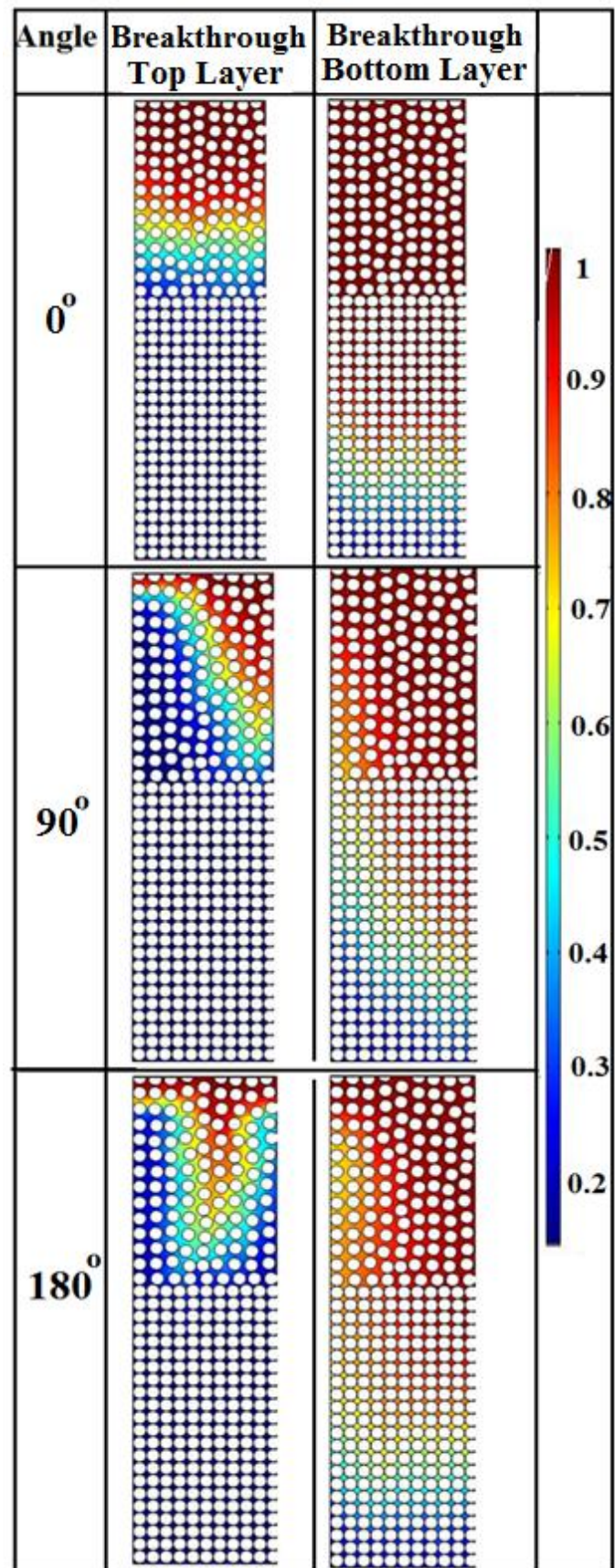
Figure 6-17: Snapshots at the Breakthrough

The graph shown in Figure 6-18 compares the S_b in the top and bottom layers at different dip angles. The Figure shows that the S_b in the top layer at 0° is highest among the rest of the cases at 90° and 180°. This is because gravity forces are more significant in the loose packing grains arrangement, and when the angle is increased from 0°, the overriding occurs in the 90° case and a gravity tongue forms in the 180° case, which in turn reduces the S_b. A difference of 18.7% S_b in the top layer is noticed between the 0° and the 90° cases.
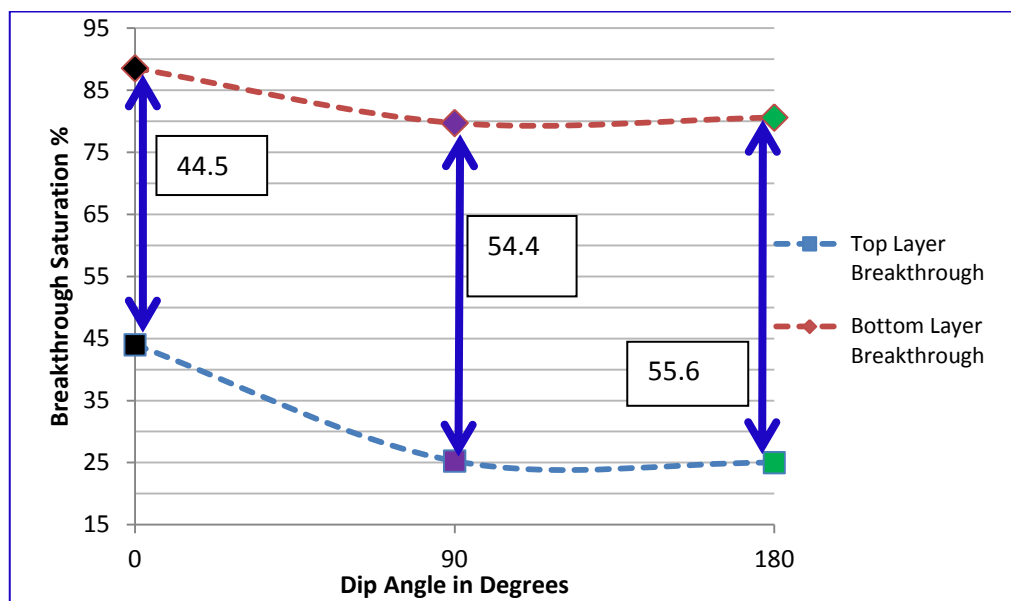
Figure 6-18: Comparison of Breakthrough Occurring at Different Dip Angle in Mix Pattern

Comparing the breakthrough curves of the top and the bottom layers for the 0° degree case in Figure 6-18, a linear increment of S_b values in the 0° case can be observed as the S_b value increases from 44% in the top layer to 88% in the bottom layer. However, a significant improvement in the S_b values of the 90° and 180° cases in the bottom layer can be observed where the S_b values improve from almost 25% in the top layer to 80% in the bottom layer. This reduces the difference between the S_b values of the 0° and 90° cases from 18.7% in the top layer to 10% in the bottom layer.

The behaviour of changing the S_b values with grains packing was quite promising. In order to understand this effect, a dimensional analysis was performed on incompressible continuity, Navier–Stokes and convection diffusion equations:

$$\frac{\partial u_i}{\partial x_i} = 0 \tag{6.1}$$

$$\rho \left(\frac{\partial u_i}{\partial t} + u_j \frac{\partial u_c}{\partial x_j} \right) = -\frac{\partial p}{\partial x_i} + \frac{\partial}{\partial x_j} \left\{ \mu \left(\frac{\partial u_i}{\partial x_j} + \frac{\partial u_j}{\partial x_i} \right) \right\} + g\rho f_i \tag{6.2}$$

$$\frac{\partial c}{\partial t} + u_j \frac{\partial c}{\partial x_j} = D \frac{\partial}{\partial x_j} \left(\frac{\partial c}{\partial x_j} \right) \tag{6.3}$$

The following dimensionless variables were considered:

$$u^* = \frac{\hat{u}}{U}, \ x^* = \frac{\hat{x}}{L}, \ p^* = \frac{\hat{p}}{P}, \ t^* = \frac{\hat{t}}{T} \ \text{and} \ T = \frac{L}{U}$$

Also:

$$\rho = \rho_1(1 - c) + \rho_2 c \tag{6.4}$$

And:

$$\mu = \mu_1(1 - c) + \mu_2 c \tag{6.5}$$

Where subscript 1 is for the inplace fluid, subscript 2 is for the injected fluid and C is the concentration of injected fluid.

Considering Equation (6.1):

$$\frac{\partial u_i}{\partial x_i} = 0$$

$$\Rightarrow \frac{U}{L} \frac{\partial u^*}{\partial x^*} = 0$$

$$\Rightarrow \frac{\partial u^*}{\partial x^*} = 0 \tag{6.6}$$

Now, consider Equation (6.2):

$$\rho \left(\frac{\partial u_i}{\partial t} + u_j \frac{\partial u_c}{\partial x_j} \right) = -\frac{\partial p}{\partial x_i} + \frac{\partial}{\partial x_j} \left\{ \mu \left(\frac{\partial u_i}{\partial x_j} + \frac{\partial u_j}{\partial x_i} \right) \right\} + g\rho f_i$$

$$\frac{U}{T} \rho \left(\frac{\partial u^*}{\partial t} + u_j \frac{\partial u^*}{\partial x^*} \right) = -\frac{P}{L} \frac{\partial p}{\partial x^*} + \frac{U}{L^2} \frac{\partial}{\partial x^*} \left\{ \mu \left(\frac{\partial u^*}{\partial x^*} + \frac{\partial u^*}{\partial x^*} \right) \right\} + g\rho f_i \tag{6.7}$$

Since, $T = \dfrac{L}{U}$

$$\frac{U^2}{L}\rho\left(\frac{\partial u^*}{\partial t} + u^*\frac{\partial u^*}{\partial x^*}\right) = -\frac{P}{L}\frac{\partial p}{\partial x^*} + \frac{U}{L^2}\frac{\partial}{\partial x^*}\left\{\mu\left(\frac{\partial u^*}{\partial x^*} + \frac{\partial u^*}{\partial x^*}\right)\right\} + g\rho f_i \tag{6.8}$$

Multiplying and dividing LHS by ρ2 and RHS by μ2:

$$\frac{\rho_2 U^2}{L}\frac{\rho}{\rho_2}\left(\frac{\partial u^*}{\partial t} + u^*\frac{\partial u^*}{\partial x^*}\right) = -\frac{P}{L}\frac{\partial p}{\partial x^*} + \frac{\mu_2 U}{L^2}\frac{\partial}{\partial x^*}\left\{\frac{\mu}{\mu_2}\left(\frac{\partial u^*}{\partial x^*} + \frac{\partial u^*}{\partial x^*}\right)\right\} + g\rho f_i \tag{6.9}$$

Multiplying whole equation by $\dfrac{L^2}{U\mu_2}$:

$$\frac{L\rho_2 U}{\mu_2}\frac{\rho}{\rho_2}\left(\frac{\partial u^*}{\partial t} + u^*\frac{\partial u^*}{\partial x^*}\right) = -\frac{LP}{U\mu_2}\frac{\partial p}{\partial x^*} + \frac{\partial}{\partial x^*}\left\{\frac{\mu}{\mu_2}\left(\frac{\partial u^*}{\partial x^*} + \frac{\partial u^*}{\partial x^*}\right)\right\} + \frac{L^2 g\rho}{U\mu_2} f_i \tag{6.10}$$

Writing equation in terms of dimensionless numbers N:

$$N_1\frac{\rho}{\rho_2}\left(\frac{\partial u^*}{\partial t} + u^*\frac{\partial u^*}{\partial x^*}\right) = -N_2\frac{\partial p}{\partial x^*} + \frac{\partial}{\partial x^*}\left\{\frac{\mu}{\mu_2}\left(\frac{\partial u^*}{\partial x^*} + \frac{\partial u^*}{\partial x^*}\right)\right\} + N_3 f_i \tag{6.11}$$

It comes up with following dimensionless numbers:

$$N_1 = R_e = \frac{L\rho_2 U}{\mu_2}$$

$$N_2 = \frac{LP}{U\mu_2}$$

Let $P = \dfrac{\mu_2 U}{L}$

Then $N_2 = 1 \Rightarrow$ so it is not considered as a dimensionless number

$$N_3 = \frac{L^2 g\rho}{U\mu_2}$$

As we know:

$$F_r = \frac{U}{\sqrt{gL}}$$

So,

$$N_3 = \frac{R_e}{F_r{}^2} = \frac{L\rho_2 U}{\mu_2} \times \frac{gL}{U^2} = \frac{L^2 \rho_2 g}{\mu_2 U}$$

Now consider Equation (6.3)

$$\frac{\partial c}{\partial t} + u_j \frac{\partial c}{\partial x_j} = D \frac{\partial}{\partial x_j}\left(\frac{\partial c}{\partial x_j}\right)$$

$$\frac{1}{T}\frac{\partial c}{\partial t^*} + \frac{Uu^*}{L}\frac{\partial c}{\partial x^*} = \frac{1}{L^2}D\frac{\partial}{\partial x^*}\left(\frac{\partial c}{\partial x^*}\right) \tag{6.12}$$

Since

$$T = \frac{L}{U}$$

$$\frac{U}{L}\frac{\partial c}{\partial t} + \frac{Uu^*}{L}\frac{\partial c}{\partial x^*} = \frac{1}{L^2}D\frac{\partial}{\partial x^*}\left(\frac{\partial c}{\partial x^*}\right)$$

$$U\frac{\partial c}{\partial t} + Uu^*\frac{\partial c}{\partial x^*} = \frac{1}{L}D\frac{\partial}{\partial x^*}\left(\frac{\partial c}{\partial x^*}\right)$$

$$\frac{\partial c}{\partial t} + u^*\frac{\partial c}{\partial x^*} = \frac{D}{UL}\frac{\partial}{\partial x^*}\left(\frac{\partial c}{\partial x^*}\right) \tag{6.13}$$

$$N_4 = \frac{D}{UL}$$

The dimensionless numbers N_3 and N_4 are the most sensitive parameters which affect the gravity and mixing respectively. It is clear that the distance between grains (*L*) and domain velocity (*U*) are the main parameters which control the interplay between gravity and mixing. If the distance between grains is reduced, then the domain velocity increases, which decreases N_3 but increases N_4. Thus the mixing effects dominate when the distance between grains is reduced.

The dimensionless numbers obtained were applied on the mixed-pattern case to understand the interplay between inter-granular distance and gravity on miscible flooding.

As we know, $U_{domain} = Q/\Phi A$

Therefore, $U_{1domain} = Q/\Phi_1 A$ and $U_{2domain} = Q/\Phi_2 A$

So, $U_{2domain}/U_{1domain} = \Phi_1/\Phi_2$

Since $\Phi_2 = 0.5\ \Phi_1$,

So,

$U_{2 \text{ domain}} = 2U_{1\text{domain}}$

Also from Table 6-5:

$L_2 = 0.0714 \, L_1$

Therefore dimensionless number N_3 for pattern 2 can be written as:

$[N_3]_{\text{pattern2}} = \text{Re}/\text{Fr}^2 = \rho \, g \, (L_2)^2/\mu \, U_{2\text{domain}}$

$= \rho \, g \, (0.0714 \, L_1)^2/\mu \, 2U_{1\text{domain}}$

$= 0.00254898 * \rho \, g \, (L_1)^2/\mu \, U_{1\text{domain}}$

$= 0.00254898 * [N_3]_{\text{pattern1}}$

And the dimensionless number N_4 for pattern 2 can be written as:

$[N_4]_{\text{pattern2}} = D/U_{2\text{domain}} \, L_2$

$= D/ (0.5 \, U_{1\text{domain}} * 0.0714 \, L_1)$

$= 7(U/ U_{1\text{domain}} \, L_1)$

$= 7[N_4]_{\text{pattern1}}$

So when the grain distance (or inter-granular distances) is reduced to half, then the effect of gravity is reduced to 0.00254 of the initial value and the effect of diffusion is seven times more. Therefore, when we tilt the pattern, nothing changes in the tight pattern, but the effect of gravity is seen in the loose pattern.

CHAPTER 7   CONCLUSION

1. Experiments in two micromodels (domain velocity 2.36 ft/day or 8.33 x 10^{-6} m/s). and 1.88 ft/day or 6.63 x 10^{-6} m/s).) show that the breakthrough saturation and breakthrough time gradually decrease with the increase in angular dip due to gravity override. However, if the fluid injection continues, the inertial forces in the 0°, 30°, 45° and 60° cases help to ultimately produce similar final recoveries regardless of the angular dip. It is concluded that the gravity effect plays an important role in the 90° experiment case, which causes the recovery to fall considerably compared with other cases.

2. Experiments representing reservoir flow rates (domain velocity 0.8 ft/day or 2.82 x 10^{-6} m/s) in the close-packing micromodel show that the diffusion/dispersion effect is more important at the leading edge of the front allowing the injected fluid to spread. Thus, if the angular tilt is higher, the injected fluid tends to rise due to gravity segregation. Also, the mixing effects can be observed at the top edge which promotes fingering phenomenon. Since the inertial effects are less due to small domain velocity, the increment in angular dip causes the breakthrough recoveries to fall in all cases. The post-breakthrough profile also shows a similar trend.

3. A novel approach to simulate glass micromodel experiments was developed. In this approach, the porous media patterns used in the experimental study were exported to COMSOL, a finite element analysis software, through a code developed using COMSOL's Livelink to MATLAB. Since the porous media patterns were the same for both the experimental and the simulation work, geometrical uncertainties were minimised. Continuity and unsteady Navier–Stokes equations were used to calculate the velocity at each node of the finite-element model. The velocity was provided to the time-dependent convection–diffusion equation to determine the concentration of the injected fluid. The corresponding simulation was run with the same input data as used in the experimental study to validate the simulation model.

4. Qualitative (photographical) and quantitative comparisons were made between the simulation and the experimental concentration values at different time steps. Besides the late time trend deviation (due to the abrupt change of the syringe

diameter in the experiments), the overall match was found to be good. The qualitative match especially shows good agreement with the movement of the front. The minor mismatch could be due to the approximation of considering a glass micromodel as a 2-D plane. Other sources of errors, such as the limitation of image processing and calculation approximations, have also been discussed.

5. A comparison of the results from the present study with the results from a previously published work was also performed. The comparison suggests that more sensitivities are required to be conducted while taking different parameters into account, such as heterogeneity and angular dip.

6. A sensitivity study was conducted based on three categories: (1) mobility ratio, density difference and angle of tilt; (2) domain velocities; and (3) local and global heterogeneity.

7. The first sensitivity study suggests an angular dip sensitive region where $0 \leq \theta \leq 90$. Increasing θ in this region significantly reduces the process efficiency. However, the other region $90 < \theta \leq 180$ seems quite insensitive to the angular dip. Buoyancy forces in this region are dominating factor and the increase in angular tilt does not produce significant effect on the process efficiency. For both regions, mobility ratio could be a sensitive parameter if the density difference between the injected fluid and the inplace fluid is small. Furthermore, inertial effects could be helpful for better sweep if the velocity remains in the dispersion domain.

8. The second part of the sensitivity study was based on performing simulation using different velocity. In addition to velocity, all other parameters, such as mobility ratios, density differences and angular tilts, remained the same as those used in the first sensitivity study. This study shows that for the high permeable dipping cases, reduction in velocity allows fluids to settle causing the lighter fluid to rise and segregate. Therefore, diffusion/mixing becomes prominent in the upper zone causing the injecting fluid to penetrate as a finger causing early breakthrough. This validates the experimental results which show that the reduction in inertial forces in dipping conditions causes the breakthrough recovery to fall.

9. The third part of the sensitivity study was based on local and global heterogeneity. For the study of localised heterogeneity, three patterns—tightly packed, moderately packed and loosely packed systems—were studied. Mobility ratio and density difference were adjusted to 1 and 100 kg/m^3 respectively. The injection velocity for each model was calculated, which represents an average domain velocity of 0.4 ft/day (1.411 x 10^{-6} m/s). . This sensitivity study was performed at 0°, 90° and 180° to study the extreme scenarios. The results show that gravity effects are more prominent in the loose-packing pattern. The sensitivity study of global heterogeneity considered a mix of loose and tight grains packing arrangements. The study shows that the tight packing promotes fluid mixing (diffusion/dispersion), which could help to reduce the gravity effects. Therefore, based on pore-scale findings, it is concluded that in less permeable zones of a reservoir the overriding of lighter fluid may be reduced even in high-dipping conditions.

10. It is recommended that the findings of this study be extended, while excluding all those assumptions and limitations which were considered when conducting this research. The present research is based on the FCM conditions. It is therefore recommended that a study be conducted which incorporates the MCM conditions. This would require an improved experimental set-up and a better mathematical model. Due to budget limitations, the present experimental study was conducted at ambient conditions, so the construction of extended laboratory facilities would also be required to conduct different experiments on different combinations of fluids. In addition, more precise equipment should be employed to deliver the accurate flow rate in the flow domain. Furthermore, future research could utilise the design of the glass holding rig to conduct experiments in both the x-y and y-z planes. Experiments could also be performed using large micromodels to gain a better understanding of flow under gravity domination. Although attempts were made to conduct experiments with dip angles greater than 90°, the design of the present injection facilities did not allow to test these scenarios. Therefore it is highly recommended that the injection facilities design be improved so experiments for dip angles between 90° and 180° could be conducted.

Furthermore, the image processing code could be improved to achieve a more accurate estimate of the porous concentration in the flow domain.

11. In addition, due to present computational challenges, the thin section of porous media was not used in the simulation work. It is therefore recommended that upon the development of new technology, thin section of porous media should be used rather than relying on the simple grains arrangement. More sensitivity studies are required to be performed, especially in the region of $90 < \theta \leq 180$ and using tight grain arrangements. Although attempts were made, the computation facilities limit present research to using a large length of the models. Sensitivities can also be performed by varying different fluid combinations with different diffusion coefficients.

REFERENCES

Abbas, F. and D. A. Rose (2010). "Viscous Fingering and Gravity Segregation through Porous Media: Experimental Findings." Earth Interactions **14**(11): 1-13.

Afrapoli, M. S., S. Alipour, et al. (2012). "Analysis of Microscopic Displacement Mechanisms of a MIOR Process in Porous Media with Different Wettability." Transport in Porous Media: 1-15.

Alajmi, A. F., A. Grader, et al. (2008). "Visualization of Steam Zone Advancement during Heavy Oil Recovery". SPE Saudi Arabia Section Technical Symposium. Al-Khobar, Saudi Arabia.

AlHamdan, M., Y. Cinar, et al. (2011). "Experimental and Numerical Study of Compositional Two-Phase Displacements in Layered Porous Media". SPE Reservoir Characterisation and Simulation Conference and Exhibition, 9–11 October 2011, Abu Dhabi, UAE.

Asgarpour, S. (1994). "An Overview of Miscible Flooding." The Journal of Canadian Petroleum Technology, **33**(2): 13-15.

Bangia, V. K., F. F. Yau, et al. (1993). "Reservoir Performance of a Gravity-Stable, Vertical CO_2 Miscible Flood: Wolfcamp Reef Reservoir, Wellman Unit." SPE Reservoir Engineering **8**(4): 261-269.

Blackwell, R. J., J. R. Rayne, et al. (1959). "Factors Influencing the Efficiency of Miscible Displacement." Petroleum Transactions, AIME, **217**: 1-8

Blunt, M. J. (2001). "Flow in Porous Media -- Pore-Network Models and Multiphase Flow." Current Opinion in Colloid and Interface Science **6**(3): 197-207.

Blunt, M. J., F. J. Fayers, et al. (1993). "Carbon Dioxide in Enhanced Oil Recovery." Energy Conversion and Management **34**(9-11): 197-1204.

Booth, R. (2008). "Miscible Flow through Porous Media." PhD Thesis, University of Oxford.

Bora, R., B. B. Maini, et al. (2000). "Flow Visualization Studies of Solution Gas Drive Process in Heavy Oil Reservoirs using a Glass Micromodel." SPE Reservoir Evaluation & Engineering **3**(3): 224-229.

BP-Amoco (1999). Movie: Gas Injection- Many Ways to Recover More Oil

Buès, M. and M. Aachib (1991). "Influence of the Heterogeneity of the Solutions on the Parameters of Miscible Displacement in Saturated Porous Medium." Experiments in Fluids **11**(1): 25-32.

Campbell, B. T. and F. J. Orr (1985). "Flow Visualization for CO_2/Crude-Oil Displacements." SPE Journal **25**(5): 665-678.

Cardenas, R. L., R. B. Alston, et al. (1984). "Laboratory Design of a Gravity-Stable Miscible CO_2 Process." Journal of Petroleum Technology **36**(1): 111-118.

Chatzis, I., A. Kantzas, et al. (1988). "On the Investigation of Gravity-Assisted Inert Gas Injection using Micromodels, Long Berea Sandstone Cores, and Computer-Assisted Tomography". SPE Annual Technical Conference and Exhibition. Houston, Texas.

Christie, M. A., A. D. W. Jones, et al. (1990). Comparison between Laboratory Experiments and Detailed Simulations of Unstable Miscible Displacement Influenced by Gravity. North Sea Oil and Gas Reservoirs—II. A. T. Buller, E. Berg, O. Hjelmelandet al, Springer Netherlands**:** 245-250.

Coskuner, G. (1993). "Onset of Viscous Fingering for Miscible Liquid-Liquid Displacements in Porous Media." Transport in Porous Media **10**(3): 285-291.

Craig(Jr)., F. F., J. L. Sanderlin, et al. (1957). "A Laboratory Study of Gravity Segregation in Frontal Drives." Petroleum Transactions, AIME, **210**: 275-282.

Crane, F. E., H. A. Kendall, et al. (1963). "Some Experiments on the Flow of Miscible Fluids of Unequal Density through Porous Media." SPE Journal **3**(4): 277-280.

Crescente, C. M., A. Rekdal, et al. (2008). "A Pore Level Study of MIOR Displacement Mechanisms in Glass Micromodels using Rhodococcus sp. 094". SPE/DOE Symposium on Improved Oil Recovery. Tulsa, Oklahoma, USA.

Davis, J. A. and S. C. Jones (1968). "Displacement Mechanisms of Micellar Solutions." Journal of Petroleum Technology **20**(12): 1415-1428.

Dumore, J. M. (1964). "Stability Considerations in Downward Miscible Displacements." SPE Journal **4**(4): 356-362.

Engelberts, W. F. and L. J. Klinkenberg (1951). "Laboratory Experiments on the Displacement of Oil by Water from Packs of Granular Material". 3rd World Petroleum Congress. The Hague, the Netherlands.

Fatt, I. (1956). "The Network Model of Porous Media." Petroleum Transactions, AIME **207**: 144-181. .

Fayers, F. J., R. I. Hawes, et al. (1981). "Some Aspects of the Potential Application of Surfactants or CO_2 as EOR Processes in North Sea Reservoirs." SPE Journal of Petroleum Technology **33**(9): 1617-1627.

Fayers, F. J. and D. Zhou (1996). "On the Importance of Gravity and Three-Phase Flow in Gas Displacement Processes." Journal of Petroleum Science and Engineering **15**(2-4): 321-341.

Freytes, V. M., A. D'Onofrio, et al. (2001). "Gravity Driven Instabilities in Miscible Non-Newtonian Fluid Displacements in Porous Media." Physica A: Statistical Mechanics and its Applications **290**(3-4): 286-304.

Gardescu, I. I. (1930). "Behavior of Gas Bubbles in Capillary Spaces." Petroleum Transactions, AIME **86**: 351-370.

Gardner, G. H. F., J. Downie, et al. (1962). "Gravity Segregation of Miscible Fluids in Linear Models." SPE Journal **2**(2): 95-104.

Garmeh, G., R. T. Johns, et al. (2007). "Pore-Scale Simulation of Dispersion in Porous Media". SPE Annual Technical Conference and Exhibition. Anaheim, California, U.S.A.

Garmeh, G., R. T. Johns, et al. (2009). "Pore-Scale Simulation of Dispersion in Porous Media." SPE Journal **14**(4): 559-567.

Ghazanfari, M. H., D. Rashtchian, et al. (2007). "Capillary Pressure Estimation using Statistical Pore Size Functions." Chemical Engineering and Technology **30**(7): 862-869.

Graue, A., B. Kvamme, et al. (2008). "MRI Visualization of Spontaneous Methane Production from Hydrates in Sandstone Core Plugs when Exposed to CO_2." SPE Journal **13**(2): 146-152.

Greenman, K. (2009). "A Regulatory Framework for Carbon Sequestration: Risks, Safety, and Social Responsibility" Honors Thesis, St Louis Environmental Studies Department, Washington University.

Grogan, A. T., V. W. Pinczewski, et al. (1988). "Diffusion of CO_2 at Reservoir Conditions: Models and Measurements." SPE Reservoir Engineering **3**(1): 93-102.

Guo, T. and G. H. Neale (1996). "Effects of Buoyancy Forces on Miscible Liquid-Liquid Displacement Processes in a Porous Medium." Powder Technology **86**(3): 265-273.

Haghighi, M., B. Xu, et al. (1994). "Visualization and Simulation of Immiscible Displacement in Fractured Systems using Micromodels: I. Drainage." Journal of Colloid and Interface Science **166**(1): 168-179.

Hagoort, J. (1980). "Oil Recovery by Gravity Drainage." SPE Journal **20**(3): 139-150.

Haines, W. B. (1925). "Studies in the Physical Properties of Soils: II. A Note on the Cohesion Developed by Capillary Forces in an Ideal Soil." The Journal of Agricultural Science **15**(4): 529-535.

Heller, J. P. (1959). "Christiansen-Type Transparent Porous Media for Flow Studies." Review of Scientific Instruments **30**(11): 1056 - 1057

Hill, S. (1952). "Channeling in Packed Columns." Chemical Engineering Science **1**(6): 247-253.

Holm, L. W. (1986). "Miscibility and Miscible Displacement." Journal of Petroleum Technology **38**(8): 817-818.

Homsy, G. M. (1987). "Viscous Fingering in Porous Media." Annual Review of Fluid Mechanics **19**(1): 271-311.

IKONICS-Imaging. (2013). "AccuArt." Retrieved 28 July 2013, from www.ikonicsimaging.com.

Jadhawar, P. S. and H. K. Sarma (2010). "Improved Production Strategy for Enhancing the Immiscible and Miscible CO_2-Assisted Gravity Drainage Oil Recovery". International Oil and Gas Conference and Exhibition in China. Beijing, China.

Jha, R. K., A. John, et al. (2006). "Flow Reversal and Mixing". SPE Annual Technical Conference and Exhibition. San Antonio, Texas, USA.

Jiao, C. and T. Maxworthy (2008). "An Experimental Study of Miscible Displacement with Gravity-Override and Viscosity-Contrast in a Hele Shaw Cell." Experiments in Fluids **44**(5): 781-794.

Johnston, J. R. (1988). "Weeks Island Gravity Stable CO_2 Pilot". SPE Enhanced Oil Recovery Symposium. Tulsa, Oklahoma.

Karadimitriou, N. K., V. Joekar-Niasar, et al. (2012). "A Novel Deep Reactive Ion Etched (DRIE) Glass Micro-Model for Two-Phase Flow Experiments." Lab on a Chip **12**(18): 3413-3418.

Kasiri, N. and A. Bashiri (2009). "Gas-Assisted Gravity Drainage (GAGD) Process for Improved Oil Recovery". International Petroleum Technology Conference. Doha, Qatar.

Kong, X., M. Haghighi, et al. (1992). "Visualization of Steam Displacement of Heavy Oils in a Hele-Shaw Cell." Fuel **71**(12): 1465-1471.

Krummel, A., S. S. Datta, et al. (2013). "Visualizing Multiphase Flow and Trapped Fluid Configurations in a Model Three-Dimensional Porous Medium." American Institute of Chemical Engineers(AIChE) **59**(3): 1022-1029.

Kuo, C. W., J. C. Perrin, et al. (2010). "Effect of Gravity, Flow Rate, and Small Scale Heterogeneity on Multiphase Flow of CO_2 and Brine". SPE Western Regional Meeting. Anaheim, California, USA.

Kurowski, P., C. Misbah, et al. (1995). "Gravitational Instability of a Fictitious Front During Mixing of Miscible Fluids." Europhys. Letters **29** (4): 309

Labec. (2013). "Muffle Furnaces." Retrieved 28 July 2013, from http://www.johnmorris.com.au/files/files/PDFs/Labec/muffle%20furnace%2009.pdf.

Lenormand, R., E. Touboul, et al. (1988). "Numerical Models and Experiments on Immiscible Displacements in Porous Media." Journal of Fluid Mechanics **189**: 165-187.

Lenormand, R., C. Zarcone, et al. (1983). "Mechanisms of the Displacement of One Fluid by Another in a Network of Capillary Ducts." Journal of Fluid Mechanics **135**: 337-353.

Lewis, J. O. (1944). "Gravity Drainage in Oil Fields SPE-944133-G." Petroleum Transactions, AIME **155.**: 133-154.

Lusis, M. A. and G. A. Ratcliff (1971). "Diffusion of Inert and Hydrogen-Bonding Solutes in Aliphatic Alcohols." American Institute of Chemical Engineers (AIChE) Journal **17**(6): 1492-1496.

Mackay, E. J., G. D. Henderson, et al. (1998). "The Importance of Interfacial Tension on Fluid Distribution During Depressurization." SPE Reservoir Evaluation & Engineering **1**(5): 408-415.

Mahmoud, T. N. and D. N. Rao (2007). "Mechanisms and Performance Demonstration of the Gas-Assisted Gravity-Drainage Process using Visual Models." SPE Annual Technical Conference and Exhibition. California, USA.

Manickam, O. and G. M. Homsy (1995). "Fingering Instabilities in Vertical Miscible Displacement Flows in Porous Media." Journal of Fluid Mechanics **288**: 75-102.

Mattax, C. C. and J. R. Kyte (1961). "Ever See Water Flood?" Oil and Gas Journal **59**(42): 115-125.

Meurs, P. V. (1957). "The use of Transparent Three-Dimensional Models for Studying the Mechanism of Flow Processes in Oil Reservoirs." Petroleum Transactions, AIME **210**: 295-301

Meybodi, H. E., R. Kharrat, et al. (2008). "Effect of Heterogeneity of Layered Reservoirs on Polymer Flooding: An Experimental Approach using Five-Spot Glass Micromodel". Europec/EAGE Conference and Exhibition. Rome, Italy.

Meyer, H. I. and D. F. Searcy (1956). "Analog Study of Water Coning." Journal of Petroleum Technology **8**(4): 61-64.

Mohammadi, A. H., H. Ji, et al. (2006). "Gas Hydrates in Oil Systems". SPE Europec/EAGE Annual Conference and Exhibition. Vienna, Austria.

Mohammadzadeh, O. and I. Chatzis (2009). "Pore-Level Investigation of Heavy Oil Recovery using Steam Assisted Gravity Drainage (SAGD)". International Petroleum Technology Conference. Doha, Qatar.

Mohiuddin, Z. and M. Haghighi (2011). "Visualization of CO_2 Displacement Process under Gravity Domination". SPE Enhanced Oil Recovery Conference. Kuala Lumpur, Malaysia.

Mohiuddin, Z., Y. Stokes, et al. (2012). Pore Level Simulation of Miscible Injection with Gravity Domination. 11 International Conference on Greenhouse Gas Technologies. Kyoto, Japan

Mollaei, A. (2005). "Experimentally Investigation and Numerically Simulation of Free Fall Gravity Drainage in Conventional and Naturally Fractured Reservoirs". Master of Science Thesis, Petroleum University of Technology (PUT), Iran and University of Calgary, Canada.

Mollaei, A., M. Haghighi, et al. (2006). "Experimental Investigation and Network Modeling Simulation of Free Fall Gravity Drainage in Single-Matrix and Fractured-Blocks Models". Abu Dhabi International Petroleum Exhibition and Conference. Abu Dhabi, UAE.

Mollaei, A., M. Haghighi, et al. (2007). "Free-Fall Gravity Drainage in Fractured Matrix Blocks: Experimental and Network Modeling Simulation Findings and Observations". Latin American & Caribbean Petroleum Engineering Conference. Buenos Aires, Argentina.

Moore, J. S. (1986). "Design, Installation, and Early Operation of the Timbalier Bay S-2B(RA)SU Gravity-Stable, Miscible CO_2-Injection Project." SPE Production Engineering **1**(5): 369-378.

Nute, A. J. (1983). "Design and Evaluation of a Gravity-Stable, Miscible CO_2-Solvent Flood, Bay St. Elaine Field". Middle East Oil Technical Conference and Exhibition. Bahrain.

Page, C. A., H. J. Brooks, et al. (1993). "Visualization of the Effects of Buoyancy on Liquid-Liquid Displacements in Vertically Aligned Porous Medium Cells." Experiments in Fluids **14**(6): 472-474.

Palmer, F. S., A. J. Nute, et al. (1984). "Implementation of a Gravity-Stable Miscible CO_2 Flood in the 8000 Foot Sand, Bay St. Elaine Field." SPE Journal of Petroleum Technology **36**(1): 101-110.

Pathak, V. (2011). "Heavy Oil and Bitumen Recovery by Hot Solvent Injection: An Experimental and Computational Investigation". SPE Annual Technical Conference and Exhibition. Denver, Colorado, USA.

Perkins, E. (2011). "Webinar Presentation on CO_2 EOR and the Transition to Carbon Storage", Global CCS Institute, Alberta, Canada

Perkins, T. K. and O. C. Johnston (1963). "A Review of Diffusion and Dispersion in Porous Media." SPE Journal **3**(1): 70 - 84.

Pozzi, A. L. and R. J. Blackwell (1963). "Design of Laboratory Models for Study of Miscible Displacement." SPE Journal **3**(1): 28-40.

Rackett, H. G. (1970). "Equation of State for Saturated Liquids." Journal of Chemical & Engineering Data **15**(4): 514-517.

Rahman, C. V. (1949). "The Theory of the Christiansen Experiment." Indian Academy of Science **29**: 381-390.

Raible, C. (1992). Report: "Improvement in Oil Recovery using Cosolvents with CO_2 Gas Floods", IIT Research Institute, National Institute for Petroleum and Energy Research, US DOE , Fossil Energy.

Rao, D. N. (2006). Patent: "Gas-Assisted Gravity Drainage (GAGD) Process for Improved Oil Recovery". World Intellectual Property Organization, US.

Rao, D. N. (2006). Report : "Development and Optimization of Gas-Assisted Gravity Drainage (GAGD) Process for Improved Light Oil Recovery", Louisiana State University and Agricultural & Mechanical College.

Rogerson, A. and E. Meiburg (1993). "Numerical Simulation of Miscible Displacement Processes in Porous Media Flows Under Gravity." Physics of Fluids A: Fluid Dynamics **5**: 2644.

Rose, W. (1957). "Studies of Waterflood Performance III - Use of Network Models " Circular 237, Division of Illinois State Geological Survey, Urbana

Rose, W. and P. Witherspoon (1956). "Trapping Oil in Pore Doublet." Producers Monthly(December): 32-38.

Sahimi, M., M. Reza Rasaei, et al. (2006). Chapter 8: "Gas Injection and Fingering in Porous Media" of Book Gas Transport in Porous Media. (editor)Clifford K. Ho and S. W. Webb, Springer Netherlands. **20:** 133-168.

Sayegh, S. G. and D. B. Fisher (2009). "Enhanced Oil Recovery by CO_2 Flooding in Homogeneous and Heterogeneous 2D Micromodels." Journal of Canadian Petroleum Technology **48**(8): 30-36.

Schowalter, W. R. (1965). "Stability Criteria for Miscible Displacement of Fluids from a Porous Medium." American Institute of Chemical Engineers (AIChE) Journal **11**(1): 99-105.

Setiawan, A., H. Nomura, et al. (2012). "Microtomography of Imbibition Phenomena and Trapping Mechanism." Transport in Porous Media **92**(2): 243-257.

Shahabinejad, K., A. Danesh, et al. (2005). "Pore-Level Investigation of Heavy-Oil Depressurisation". SPE/PS-CIM/CHOA International Thermal Operations and Heavy Oil Symposium. Calgary, Alberta, Canada.

Shariatpanahi, S. F., A. Dastyari, et al. (2005). "Visualization Experiments on Immiscible Gas and Water Injection by using 2D-Fractured Glass Micromodels". SPE Middle East Oil and Gas Show and Conference. Kingdom of Bahrain.

Siddiqui, H. and M. Sahimi (1990). "Computer Simulations of Miscible Displacement Processes in Disordered Porous Media." Chemical Engineering Science **45**(1): 163-182.

Simon, R. and F. J. Kelsey (1971). "The use of Capillary Tube Networks in Reservoir Performance Studies: 1. Equal-Viscosity Miscible Displacements." SPE Journal **11**(2): 99-112.

Slobod, R. L. (1964). "The Effects of Gravity Segregation in Laboratory Studies of Miscible Displacement in Vertical Unconsolidated Porous Media." SPE Journal **4**(1): 1-8.

Smith Duane, H. (1988). Chapter 1: "Promise and Problems of Miscible-Flood Enhanced Oil Recovery" of Book. Surfactant-Based Mobility Control ,Progress in Miscible-Flood Enhanced Oil Recovery. (editor)Duane H. Smith, American Chemical Society. **373:** 2-37

Sohrabi, M., D. H. Tehrani, et al. (2004). "Visualization of Oil Recovery by Water-Alternating-Gas Injection Using High-Pressure Micromodels." SPE Journal **9**(3): 290-301.

Stalkup, F. I. J. (1983). "Miscibile Displacement", SPE Monograph volume 8, Society of Petroleum Engineers.

Stevenson, K. (2004). "Miscible Network Model 2-D Simulations of Two-Phase Flow Displacements in Porous Media with Gravitational and Distributional Effects". MSc Thesis, West Virginia University.

Stevenson, K., G. S. Bromhal, et al. (2004). "Miscible, Vertical Network Model 2-D Simulations of Two-Phase Flow Displacements in Porous Media." Physica A: Statistical Mechanics and its Applications **343**: pages 317-334.

Stevenson, K., M. Ferer, et al. (2006). "2-D Network Model Simulations of Miscible Two-Phase Flow Displacements in Porous Media: Effects of Heterogeneity and Viscosity." Physica A: Statistical Mechanics and its Applications **367**: 7-24.

Tchelepi, H. A. and F. M. Orr (1994). "Interaction of Viscous Fingering, Permeability Heterogeneity, and Gravity Segregation in Three Dimensions." SPE Reservoir Engineering **9**(4): 266-271.

Tiffin, D. L. and V. J. Kremesec-Jr. (1988). "Mechanistic Study of Gravity-Assisted CO_2 Flooding." SPE Reservoir Engineering **3** (2): 524-532.

Tyne, M. T. and W. F. Calus (1975). "Diffusion Coefficients in Dilute Binary Liquid Mixtures." Journal of Chemical and Engrineering Data **20(1):106**.

Vermeulen, T. N. (2011). Chapter 5 : "Chain Components" of Report CO_2 Liquid Logistics Shipping Concept (LLSC) - Overall Supply Chain Optimization.

Wang, G. C. (1980). "A Laboratory Study of the Effects of CO_2 Injection Sequence on Tertiary Oil Recovery." SPE Journal **20**(4): 278-280.

Wilke, C. R. and P. Chang (1955). "Correlation of Diffusion Coefficients in Dilute Solutions." American Institute of Chemical Engineers (AIChE) Journal **1**(2): 264-270.

Withjack, E. M. and I. Akervoll (1988). "Computed Tomography Studies of 3-D Miscible Displacement Behavior in a Laboratory Five-Spot Model". SPE Annual Technical Conference and Exhibition. Houston, Texas.

Wu, M., F. Xiao, et al. (2011). "Single and Two-Phase Flow in Microfluidic Porous Media Analogs Based on Voronoi Tessellation." Lab Chip **12**(2): 253-261.

Wyckoff, R. D., H. G. Botset, et al. (1932). "Flow of Fluids Through Porous Media under the Action of Gravity." Journal of Applied Physics **3**(2): 90-113.

Xu, B., J. Kamath, et al. (1999). "Use of Pore-Network Models to Simulate Laboratory Corefloods in a Heterogeneous Carbonate Sample." SPE Journal **4**(3): 178-186.

Xu, J. Q. (2008). "Modeling Unsteady-State Gravity-Driven Flow in Porous Media." Journal of Petroleum Science and Engineering **62**(3-4): 80-86.

Yoon, J. S., J. T. Germaine, et al. (2006). "Visualization of Particle Behavior within a Porous Medium: Mechanisms for Particle Filtration and Retardation during Downward Transport." Water Resources Research **42**(6).

APPENDIX A1: Source Code for Generating Grains

```
import com.comsol.model.*

import com.comsol.model.util.*

model = ModelUtil.create('Model');

model.modelPath('');

model.modelNode.create('mod1');

model.geom.create('geom1', 2);

model.mesh.create('mesh1', 'geom1');

indx=1;

%-%%%%% Basic Inputs %%%%%

%% Units in Centimetres

nx  = 13;                      % No of circles in x direction

ny  = 16;                      % No of circles in y direction

m   = 0.58;                    % Mean distance between circles

std = 0.0266;                  % Standard Deviation

v   = std*std;                 % Variance

ax= 0.25;                      % starting x co-ordinate i.e. x coordinate of first circle

r= 0.25; %radius of circle

ay=0.25;                       % starting y co-ordinate i.e. y coordinate of first circle


%%%%%%Creating x and y co-ordinates of n Circles%%%%%%%%%%%-

Yoff = m +std*randn(ny-1,nx);
```

```matlab
Xoff = m + std*randn(ny,nx-1);
```

% Move the Ycoord and Xcoord to here, and use the same starting points as in your other variables:

```matlab
Ycoord = cumsum( vertcat(ay*ones(1,nx), Yoff), 1);

Xcoord = cumsum( horzcat(ax*ones(ny,1), Xoff), 2);

%%%%%%For COMSOL Geometry%%%%%%%%%%%%%%%%

u=0:0.01:1; %degree

for y=1:nx

        for x=1:ny

                xpos = Xcoord(x,y);

                ypos = Ycoord(x,y);


                eval(['model.geom("geom1").feature.create("c',num2str(indx),'",
"Circle");'])

                eval(['model.geom("geom1").feature("c',num2str(indx),'").set("r",
'',num2str(r),'");'])


        eval(['model.geom("geom1").feature("c',num2str(indx),'").setIndex("pos",
'',num2str(xpos),'", 0);'])


        eval(['model.geom("geom1").feature("c',num2str(indx),'").setIndex("pos",
'',num2str(ypos),'", 1);'])

        indx=indx+1;

    end

end
```

```
model.geom('geom1').runAll;


model.save('c:\COMSOL41_copy1\new model designed.mph')

%%%%%%For Circles Plotting%%%%%%%%%%%%%%%%%%

u=0:0.001:1; %degree

for y=1:nx

for x=1:ny

whitebg('w')                                        % setting background to white

set(gca,'units','centimeters')                       % for units standardization

%set(gca,'xlimmode','manual','ylimmode','manual')  % for units standardization

axpos = get(gca,'position');                        % for units standardization

set(gca,'position',[axpos(1:2)   abs(diff(xlim))   abs(diff(ylim))])   %   for   units
standardization

axis equal % to make circles round

  fill(Xcoord(x,y)+r*cos(2*pi*u),Ycoord(x,y)+r*sin(2*pi*u),'k');  %  make  circles  of
white in colour

    hold on

    end

end
```
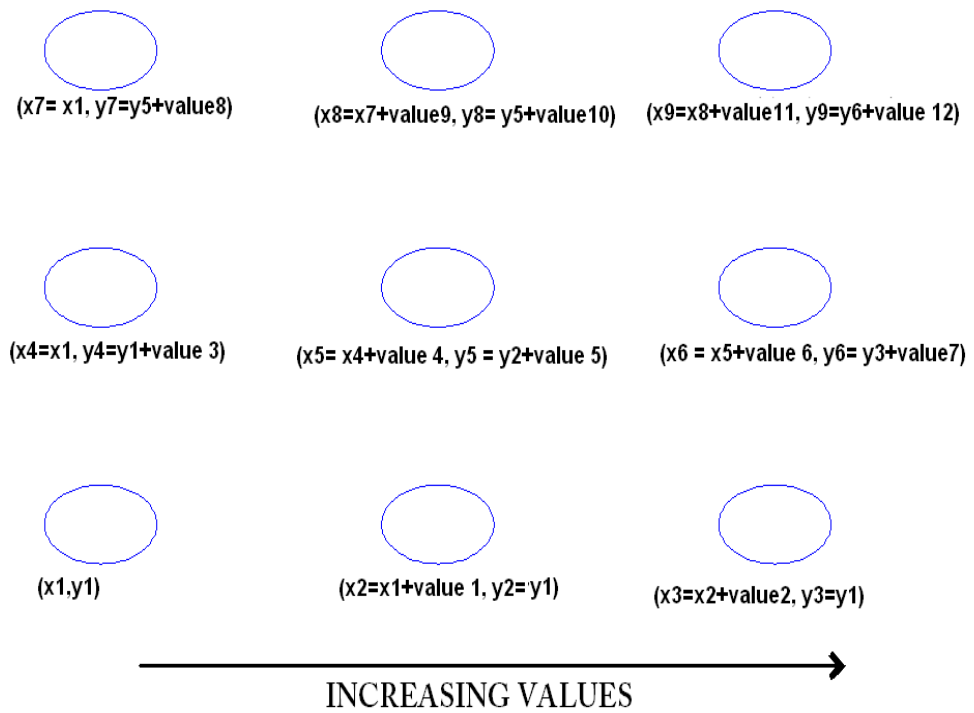
APPENDIX A2: Grain Arrangements

(x7= x1, y7=y5+value8)   (x8=x7+value9, y8= y5+value10)   (x9=x8+value11, y9=y6+value 12)

(x4=x1, y4=y1+value 3)   (x5= x4+value 4, y5 = y2+value 5)   (x6 = x5+value 6, y6= y3+value7)

(x1,y1)   (x2=x1+value 1, y2= y1)   (x3=x2+value2, y3=y1)

INCREASING VALUES

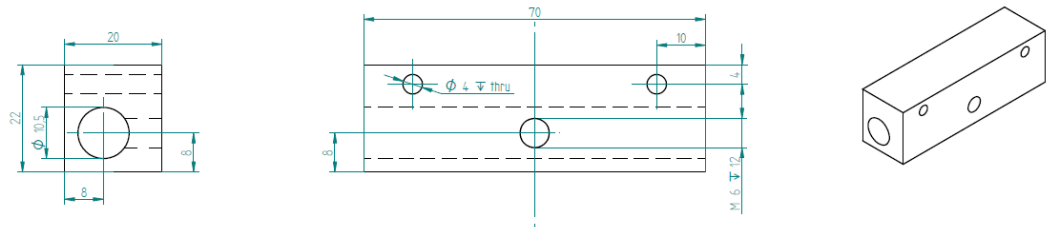Figure A2-7-1 Circular Arrangement of the Numerically Controlled Pattern

Distance Between the Circles (cm)

(A)

(B)
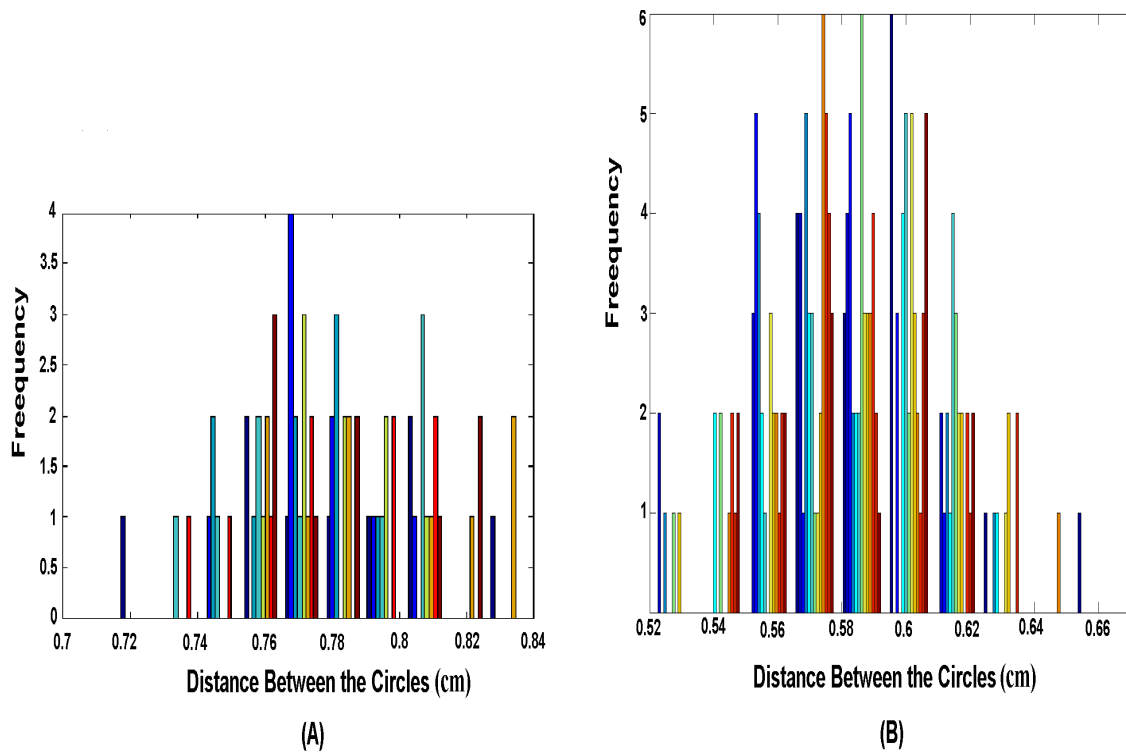
Figure A2-7-2 Distribution of Distances between the Centres of Circles for (a) Pattern 1 and (b) Pattern 2
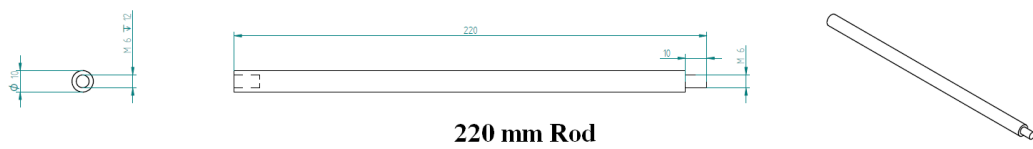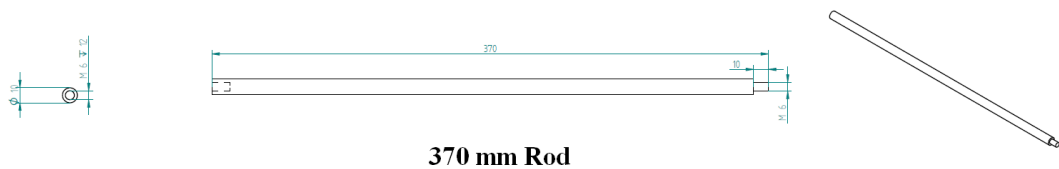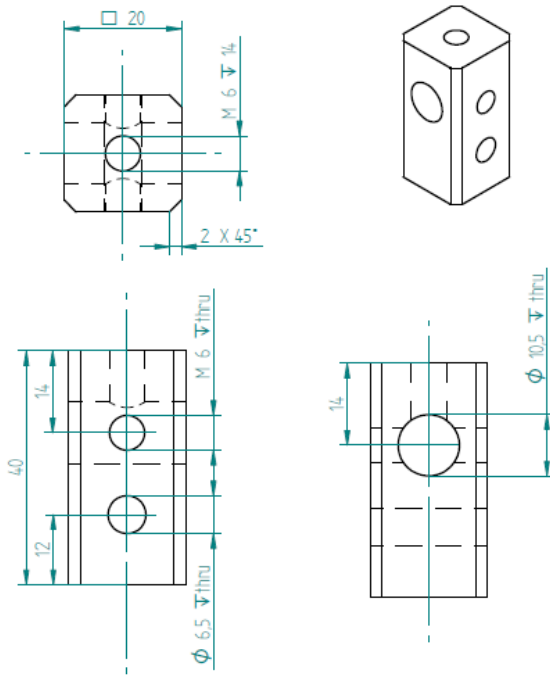
APPENDIX B: Detailed Designed of the Experimental Rig
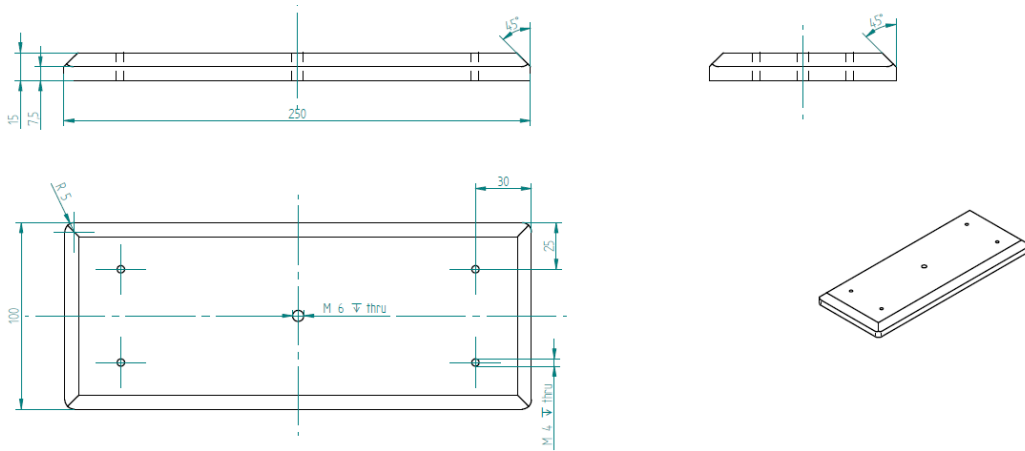
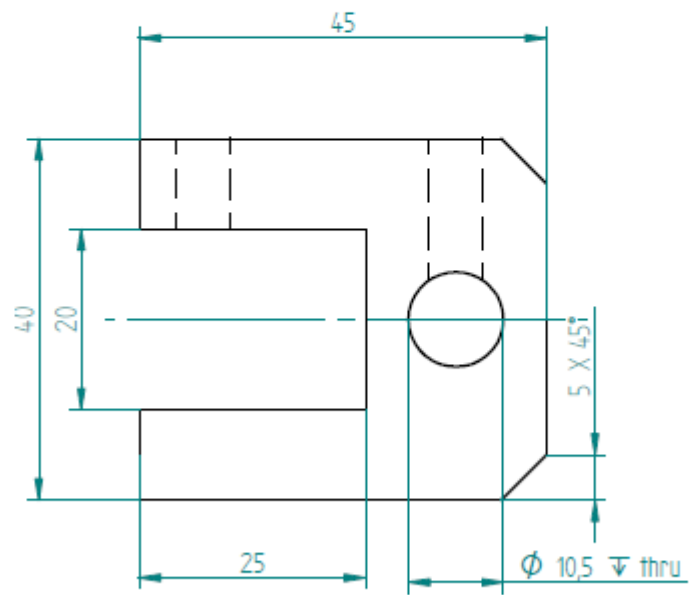
Base Plate

Base Alignment Slider

220 mm Rod
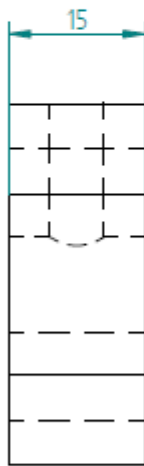

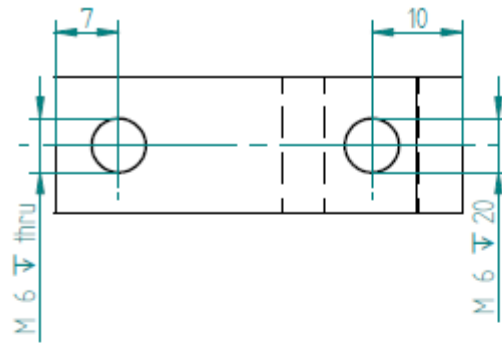**370 mm Rod**

Vertical Bar Connector

□ 20

M 6 ▼ 14

2 X 45°

M 6 ▼ thru

14

40

12

Φ 6.5 ▼ thru

Φ 10.5 ▼ thru

14

Frame Connector

80

8

8

M 6 ▼ 10

20

25

8

8

Φ 10.5 ▼ thru

Φ 6 ▼ 15

20

10

7
10
M 6 ▽ thru
M 6 ▽ 20

15

45
40
20
5 X 45°
25
Ø 10,5 ▽ thru
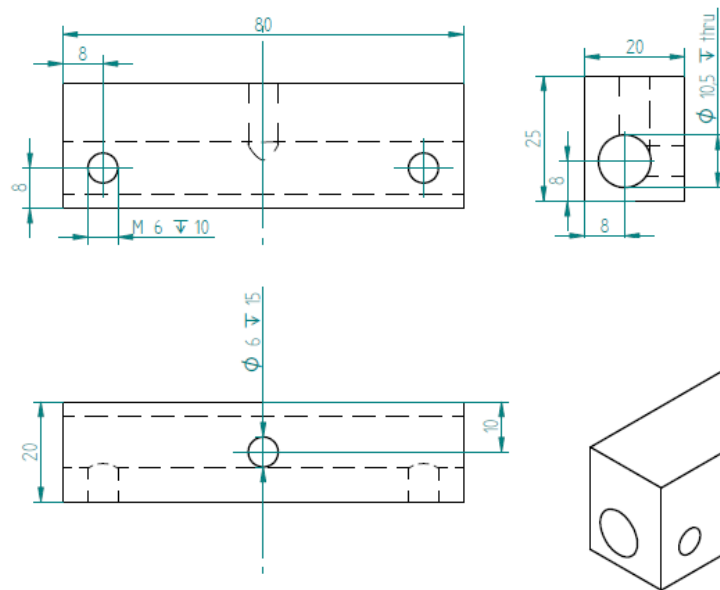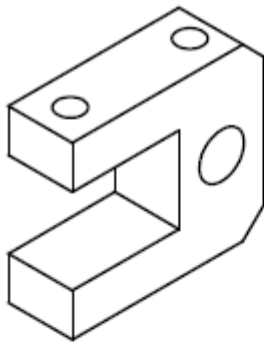
Glass Holder

APPENDIX C: Image Processing Source Code

```
figure

clear M

d=dir('*min.jpg');

min_sat_ref=0;

max_sat_ref=0;

% defines color range over which saturation is kept (ie. relates to the colour range of the
dye (in this case a pinkish red colour).

dye_hsv_min_limit = 0.2;

dye_hsv_max_limit  = 0.6;

% read "final" reference image and set max saturation accordingly

finalname = 'final 279.38min.jpg';

I=imread(finalname);

Ihsv = rgb2hsv(I);

S   =   Ihsv(:,:,2)    .*   (   (Ihsv(:,:,1)  <  dye_hsv_min_limit)  |  (Ihsv(:,:,1)  >
dye_hsv_max_limit) );

s=sort(S(:));

max_sat_ref = s( round(0.98*length(s)) );

% cycle thru each image in turn

for i=1:length(d)

  I= imread(d(i).name);

    Ihsv = rgb2hsv(I);
```

```matlab
  S   =   Ihsv(:,:,2)   .*   (   (Ihsv(:,:,1)   <   dye_hsv_min_limit)   |   (Ihsv(:,:,1)   >
dye_hsv_max_limit) );

    subplot(2,1,1)

  imagesc(I);axis equal tight;

  title(d(i).name);

  subplot(2,1,2);

  % scale image to 0..100 where the estimated max saturation goes to 100

  % and virtually no saturation goes to zero.

  imagesc( min( 100*S / max_sat_ref , 100 ) );

  caxis([0 100]);

  axis equal tight

  colorbar

  drawnow;

    M(i)=getframe(gcf);


end

% and just plot the reference to complete the process

I=imread(finalname);

Ihsv = rgb2hsv(I);

S   =   Ihsv(:,:,2)      .*   (   (Ihsv(:,:,1)   <   dye_hsv_min_limit)   |   (Ihsv(:,:,1)   >
dye_hsv_max_limit) );

subplot(2,1,1)

imagesc(I);axis equal tight;
```

```matlab
title(finalname);

subplot(2,1,2);

imagesc( min( 100*S / max_sat_ref , 100 ) );

caxis([0 100]);

axis equal tight

colorbar

drawnow;

M(end+1)=getframe(gcf);

% save movie file

disp('Saving movie...');

movie2avi(M,'movie.avi','compression','none');
```

APPENDIX D: Source Code for Creating Multiple Layers of Grains

```
import com.comsol.model.*

import com.comsol.model.util.*

model = ModelUtil.create('Model');

model.modelPath('');

model.modelNode.create('mod1');

model.geom.create('geom1', 2);

model.mesh.create('mesh1', 'geom1');

indx=1;

indxx=1;

%%%%%%%%%For First Series of Circles %%%%%%%%%%%%%%%%%%%%

nx  = 11; % No of circles in x direction

ny  = 22; % No of circles in y direction

m   = 0.305; % Mean distance between circles

std = 0.00125; % Standard Deviation

ax= 0.15; % starting x co-ordinate i.e x cordinate of first circle

r= 0.15; %radius of circle

ay=0.15; % starting y co-ordinate i.e y c

%%%%%%%% Determining the Co-ordinates for First Series of Circles %%%%%%%%%%%%

Yoff = m+std*randn(ny-1,nx);

Xoff = m+ std*randn(ny,nx-1);

Ycoord = cumsum( vertcat(ay*ones(1,nx), Yoff), 1);

Xcoord = cumsum( horzcat(ax*ones(ny,1), Xoff), 2);

%%%%%For Second Series of Circles %%%%%%%%%%%%%%%%%%%

nx2  = 9; % No of circles in x direction

ny2  = 14; % No of circles in y direction
```

```matlab
m2  = 0.37; % Mean distance between circles

std2 = 0.0233; % Standard Deviation

r2= 0.15; %radius of circle

lastx= Xcoord(ny,nx);

ax2= ax;

maximum_of_lastrow =max( Ycoord(ny,nx)); % starting y co-ordinate i.e y c

ay2= maximum_of_lastrow+r+r2;

%%%%%%%% Determining The Co-ordinates for Second Series of Circles %%%%%%%

Yoff2 = m2 +std2*randn(ny2-1,nx2);

Xoff2 = m2 + std2*randn(ny2,nx2-1);

Ycoord2 = cumsum( vertcat(ay2*ones(1,nx2), Yoff2), 1); %%%%%%

Xcoord2 = cumsum( horzcat(ax2*ones(ny2,1), Xoff2), 2);

%%%%%%-%%%%%%Comsol Geometry%%%%%%%%%%%%%%%%%%%%%

u=0:0.01:1; %degree

for y=1:nx

        for x=1:ny

                xpos = Xcoord(x,y);

                ypos = Ycoord(x,y);

                eval(['model.geom(''geom1'').feature.create(''c',num2str(indx),''', ''Circle'');'])

                eval(['model.geom(''geom1'').feature(''c',num2str(indx),''').set(''r'',
''',num2str(r),''');'])

                eval(['model.geom(''geom1'').feature(''c',num2str(indx),''').setIndex(''pos'',
''',num2str(xpos),''', 0);'])

                eval(['model.geom(''geom1'').feature(''c',num2str(indx),''').setIndex(''pos'',
''',num2str(ypos),''', 1);'])

    indx=indx+1;

  end

end
```

```
for yy=1:nx2

        for xx=1:ny2

                xpos2 = Xcoord2(xx,yy);

                ypos2 = Ycoord2(xx,yy);

                eval(['model.geom(''geom1'').feature.create(''y'',num2str(indxx),''', ''Circle'');'])

                eval(['model.geom(''geom1'').feature(''y'',num2str(indxx),''').set(''r'',
'',num2str(r2),''');'])

                eval(['model.geom(''geom1'').feature(''y'',num2str(indxx),''').setIndex(''pos'',
'',num2str(xpos2),''', 0);'])

                eval(['model.geom(''geom1'').feature(''y'',num2str(indxx),''').setIndex(''pos'',
'',num2str(ypos2),''', 1);'])

    indxx=indxx+1;

  end

end

model.geom('geom1').runAll;

model.save('c:\Newfolder1\new model designed2layers.mph')

%%%%%%%%%%%%%%For Circles Plotting%%%%%%%%%%%%%%%%%%%%-%

u=0:0.001:1; %degree

for y=1:nx

        for x=1:ny

whitebg('w') % setting background to white


set(gca,'units','centimeters')    % for units standardization

%set(gca,'xlimmode','manual','ylimmode','manual')% for units standardization

axpos = get(gca,'position');               % for units standardization

set(gca,'position',[axpos(1:2) abs(diff(xlim)) abs(diff(ylim))]) % for units standardization

axis equal % to make circles round

 fill(Xcoord(x,y)+r*cos(2*pi*u),Ycoord(x,y)+r*sin(2*pi*u),'k'); % make circles of white in colour
```

```
    hold on

    end

end

u=0:0.001:1; %degree

for y=1:nx2

        for x=1:ny2

whitebg('w') % setting background to white

set(gca,'units','centimeters')    % for units standardization

%set(gca,'xlimmode','manual','ylimmode','manual')% for units standardization

axpos = get(gca,'position');              % for units standardization

set(gca,'position',[axpos(1:2) abs(diff(xlim)) abs(diff(ylim))]) % for units standardization

axis equal % to make circles round

  fill(Xcoord2(x,y)+r2*cos(2*pi*u),Ycoord2(x,y)+r2*sin(2*pi*u),'k'); % make circles of white in
colour

    hold on

    end

end
```